ISSN en trámite

Geofísica Internacional

Revista Trimestral Publicada por el Instituto de Geofísica de la Universidad Nacional Autónoma de México

México
Volume 56 Number 2
April - June
2017

— Geofísica Internacional —

GEOFÍSICA INTERNACIONAL, Año 56, Vol. 56, Núm. 2, abril - junio de 2017 es una publicación trimestral, editada por la Universidad Nacional Autónoma de México, Ciudad Universitaria, Alcaldía Coyoacán, C.P. 04150, Ciudad de México, a través del Instituto de Geofísica, Circuito de la Investigación Científica s/n, Ciudad Universitaria, Alcaldía Coyoacán, C.P. 04150, Ciudad de México, Tel. (55)56 22 41 15. URL: http://revistagi.geofisica.unam.mx, correo electrónico: revistagi@igeofisica.unam.mx. Editora responsable: Andrea Rostan Robledo. Certificado de Reserva de Derechos al uso Exclusivo del Título: 04-2022-081610251200-102, ISSN: en trámite, otorgados por el Instituto Nacional del Derecho de Autor (INDAUTOR). Responsable de la última actualización Saúl Armendáriz Sánchez, Editor Técnico. Fecha de la última modificación: 31 de marzo 2017, Circuito de la Investigación Científica s/n, Ciudad Universitaria, Alcaldía Coyoacán, C.P. 04150, Ciudad de México.

Geofísica Internacional

Vol. 56, Núm. 2, abril-junio de 2017

Contents

Geofísica Internacional (2017) 56-2: 137-145

Original paper

Attenuation of Coda Waves in the Central Region of the Gulf of California, México

Héctor E. Rodríguez-Lozoya, Tonatiuh Domínguez R., Luis Quintanar Robles, Armando Aguilar Meléndez, Héctor E. Rodríguez-Leyva, Wenseslao Plata Rocha and Fernando García Páez

Received: January 06, 2016; accepted: October 25, 2016; published on line: April 01, 2017

Resumen

Se analizan las ondas de coda de eventos registrados por la red sísmica de NARS que cuenta con instrumentos instalados a lo largo de ambas márgenes del Golfo de California, México, para estimar atenuación Q_c. Se utilizó modelo de dispersión simple de Sato (1977) para ventanas tiempo de 20 a 25 segundos comenzando en dos veces el tiempo de viaje de la onda S. Se analizaron eventos registrados entre 2003 y 2007 ocurridos en la región central del Golfo de California. Las distancias fuente-receptor analizadas son entre 40 y 500 km. Suponiendo una relación de dependencia de Q_c de la frecuencia de la forma $Q_C(f) = Q_o f^a$, los valores promedio encontrados fueron de Q_o = 83±3 y una dependencia de la frecuencia a de 1.06±0.03 en el rango de frecuencias de 1 a 7 Hz. El valor Q_o y la alta dependencia de la frecuencia están de acuerdo con los valores reportados para otras regiones caracterizadas por una alta actividad tectónica. Con base en la distribución de estaciones respecto a las fuentes, se definieron dos subregiones (norte y sur). Se calcularon los valores de Q_C y se correlacionaron con la tectónica y morfología de cada zona. Se observa una mayor atenuación en la región sur que puede ser atribuida a que esa zona esté más fracturada dado que los eventos sísmicos mayores ocurren de la zona centro del Golfo de California hacia el sur. Por otro lado, la corteza de la zona sur es de menor espesor que la zona norte.

Palabras clave: Atenuación de coda, atenuación-frecuencia, Golfo de California, Mexico.

H. E. Rodríguez-Lozoya*
H. E. Rodríguez-Leyva
F. García Páez
Facultad de Ingeniería
Universidad Autónoma de Sinaloa, México
*Corresponding author: rolohe1@yahoo.com.mx

T. Domínguez R.
Centro Universitario de Estudios
e Investigación en Vulcanología
Universidad de Colima, México

L. Quintanar Robles
Instituto de Geofísica
Universidad Nacional Autónoma de México
Ciudad Universitaria
Delegación Coyoacán 04510
Mexico CDMX, México

A. Aguilar Meléndez
Universidad Veracruzana
Campus Poza Rica, México

W. Plata Rocha
Facultad de Ciencias de la Tierra y el Espacio
Universidad Autónoma de Sinaloa, México

Abstract

Coda waves were analyzed from events recorded by NARS seismic network deployed along both margins of the Gulf of California, Mexico, to estimate coda attenuation Qc. Sato's (1977) single scattering model was used for a coda window of 20 to 25 s beginning at twice the S-wave travel time. Events recorded from 2003 to 2007 located in the central region of the Gulf of California were analyzed.
Source-to-receiver distances are between 40 and 500 km. Assuming a power law of the form $Q_C(f) = Q_o f^a$, Q_C values were averaged and a value of Q_o = 83±3 and a frequency-dependence α value of 1.06±0.03 in the frequency range from 1 to 7 Hz was obtained. Q_o value and the high frequency dependency agree with the values of other regions characterized by a high tectonic activity.
Based on source-station distribution two subregions (north and south) were defined. Q_C values were calculated and correlated with tectonics and morphology of each area. The observed higher attenuation in the south region can be attributed to the fact that south region is more fractured since the greater earthquakes occur in central to south Gulf of California and the oceanic crust is reported to be thinner in the southern region.

Key words: Coda attenuation, attenuation-frequency, Gulf of California, Mexico.

Introduction

The Gulf of California, Mexico, is a complex tectonic zone where the peninsula of Baja California is separating from the continent. This active zone has generated moderate earthquakes which have affected cities on both sides of the gulf. In 2012, an M6.0 earthquake affected the city of Los Mochis, where damages in the regional hospital were reported. Last earthquake occurred on September, 2015 (M_W6.7).

Social and economic effects resulting from earthquakes can be reduced through seismic risk analysis. The elaboration of good quality hazard maps is required. To do this, studies of source characteristics and wave propagation are essential. Attenuation is an important factor to such studies.

Attenuation of seismic waves has been widely studied in different regions around the world since Aki and Chouet (1975) and Sato (1977) introduced their theories on coda waves attenuation (Q). Different tectonic regions around the world (e.g., volcanic, active, stable) have been characterized by their Q^{-1} values (Pulli, 1984; Jin *et al*., 1985; Wiggins-Grandison and Havskov, 2004, among others). In Mexico there are attenuation studies mostly for the south and southeastern for the subduction zones of the Rivera and Cocos plates (Castro and Munguía, 1993; Ordaz and Singh 1992; Domínguez *et al*., 2003, among others) and for the northwestern zone of Mexico for the Gulf of California region (Domínguez *et al*., 1997; Castro *et al*., 2008).

In the present study, Sato's formulation (Sato, 1977) was used to estimate Q_C at the central zone of the Gulf of California.

Data from 6 stations of the NARS-Baja network (Network of Autonomously Recording Seismographs of Baja California) installed by Utrecht University, CALTECH and CICESE (Centro de Investigación Científica y Educación Superior de Ensenada Baja California, México) during 2002 were used. This region was chosen due to its implication in terms of civil protection for the cities on both sides of the Gulf. The correlation of the results with the morphology and tectonics of the region is also presented.

Tectonic Setting and Seismicity

The Gulf of California forms an oblique-divergent boundary between the Pacific and North America plates. Relative motion between the peninsula of Baja California and North America plate in the southern gulf is about 46 mm/yr (Plattner *et al*., 2007). It consists of a system of linked transform faults and short spreading centers forming basins (Lonsdale, 1989). Deformation accommodates in oblique faults to the north and transform faults to the south (Fenby and Gastil, 1991; Nagy and Stock, 2000). Northern basins are shallower than those to the center and southern basins (Curray *et al*., 1982; Lonsdale, 1989; Persaud *et al*., 2003).

In the north zone of the Gulf, an incipient spreading center begins in the Wagner basin (Persaud *et al*., 2003) developed from Cerro Prieto and Wagner transform faults, and ending in the south with the East Pacific Rise which corresponds to the northern limit of the Rivera plate.

Lonsdale (1989) suggested the presence of a transitional crust at the Guaymas basin in the middle sector of the Gulf of California. In this location, there is a high rate of sedimentation,

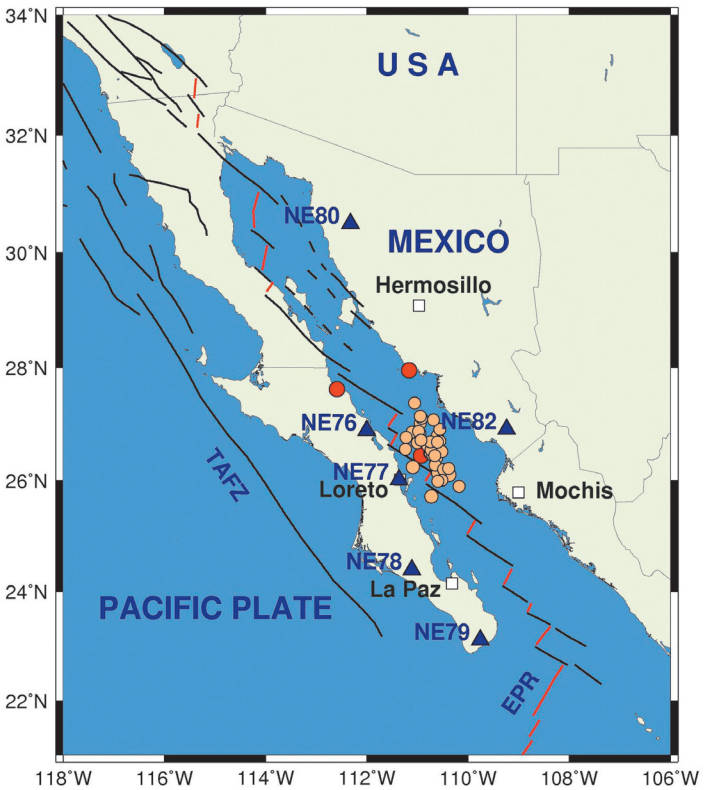

Figure 1. Tectonic setting and location of used seismic stations (triangles) and analyzed earthquakes (circles). White squares indicate main cities in the area. Red circles indicate events with Mw >5. TAFZ (Tosco-Abreajos fault zone), EPR (East Pacific Rise).

which promoted the development of a basin containing sills and altered sediments.

Most of the seismicity is distributed in the NW–SE direction along the axis of the Gulf of California, following a linear trend that, from north to south, steps southward near the main basins (Wagner, Delfin, Guaymas, Carmen, Farallon, Pescadero, and Alarcon) and spreading centers. Seismicity in the northern zone has low magnitude (Castro *et al*., 2007) but increases to the south reaching magnitudes of M>6 such as the 2010 and 2015 earthquakes that occurred near (south) parallel 25° N, or the 1992 earthquake (M7.0), which is the greater earthquake ever recorded in this zone (Pacheco and Sykes, 1992).

Only good quality data (high signal/noise ratio) was used from five years recording which included 4 moderate events (M>5) and their aftershocks (Figure 1).

Method

Sato's (1977) formulation was used to estimate Q_c through measurements of the amplitude decay of coda waves with time. The model assumes a source embedded in an infinite medium populated by a random distribution of scatterers in an infinite volume and cross-sectional area σ. The density of energy in terms of root mean square (*rms*) amplitude, scattered by the inhomogeneities on the surface of an ellipsoid whose foci are the source, and the receiver can be expressed as

$$A(r,t \setminus \omega) = \frac{1}{\omega}\left[\frac{\Omega(\omega)\Delta f}{2\pi\sigma L}\right]^{1/2} \frac{\left[K(\alpha)\right]^{1/2}}{r} e^{-\omega t/2Q}, \quad (1)$$

where A is the *rms* amplitude of the coda wave, $\Omega(\omega)$ is the total energy radiated by the source within a frequency band, r is the distance between the source and the receiver, $K(\alpha) = \frac{1}{\alpha} ln[(\alpha+1)/(\alpha-1)]$ and $\alpha = t/t_s$, t is the elapsed time of the coda wave, t_s is the elapsed time of the S wave, both measured from the earthquake origin time. $L = 1/N\sigma$ is the mean free path.

Usually (1) is expressed as the linear function

$$\frac{\ln\left[A(r,t \setminus \omega)\right]}{\left[K(\alpha)\right]} = \ln C - (\pi f / Q)t \quad (2)$$

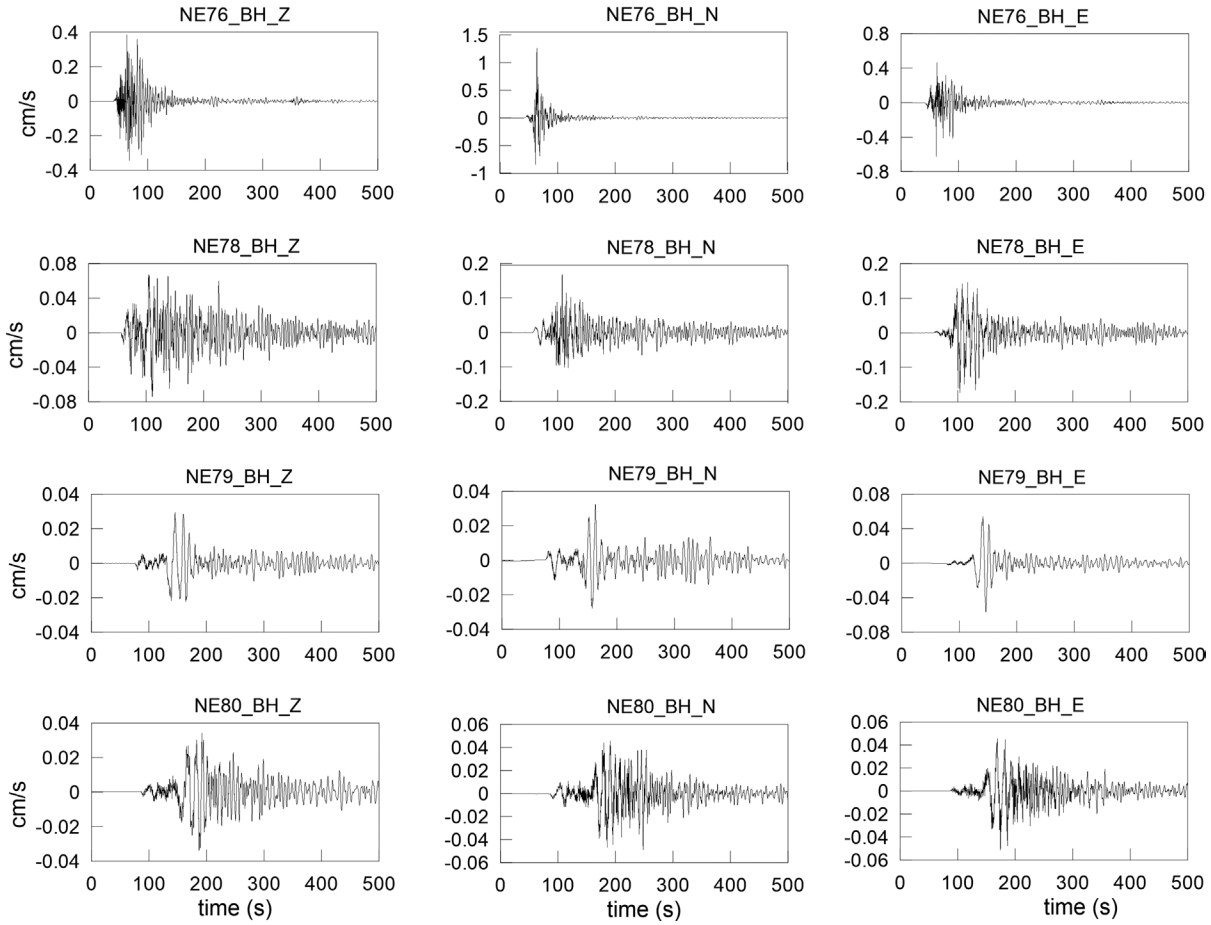

Figure 2. Example of an event used for Q_c calculation. Records correspond to the 2003/03/12 earthquake (M_w6.3).

Table 1: Velocity model.

Vp (km/s)	Vs (km/s)	Density (kg/m^3)	Thickness (km)
4.0	2.6	1800	4.0
5.7	3.3	2500	4.0
6.7	3.8	3000	16.0
7.8	4.0	3400	400.0

where the quality factor Q can be obtained from the slope of the linear fit of the logarithm of the observed amplitude (root mean square amplitude) of the coda wave vs t for the frequency f.

Data

Records from the three components of six stations of NARS were used (Trampert *et al*., 2003). Each station consists of a 3-channel, broad band STS-2 sensor (velocity) connected to a 24 bit resolution recorder. 20 samples per second are recorded. For this reason the analysis was restricted to frequencies below 10 Hz.

Records from 2003 to 2007 were available. From this database only events recorded by at least four stations, presenting no saturation, showing high signal/noise ratio (>5) and no overlapping with other events (case of aftershocks) were selected to ensure good quality data. An example of a record is shown in Figure 2.

Processing began with locating events. Hypocenter (Lienert *et al*., 1986; Lienert and Havskov, 1995) which is included in SEISAN code (Ottemöller *et al.,* 2013) was used. The one-dimensional velocity model used by Rebollar *et al*. (2001) shown in table 1, was also used. From all the located events, we selected only those which were in the area of interest, between parallels and N. 50 events filled these criteria and those mentioned above, and were

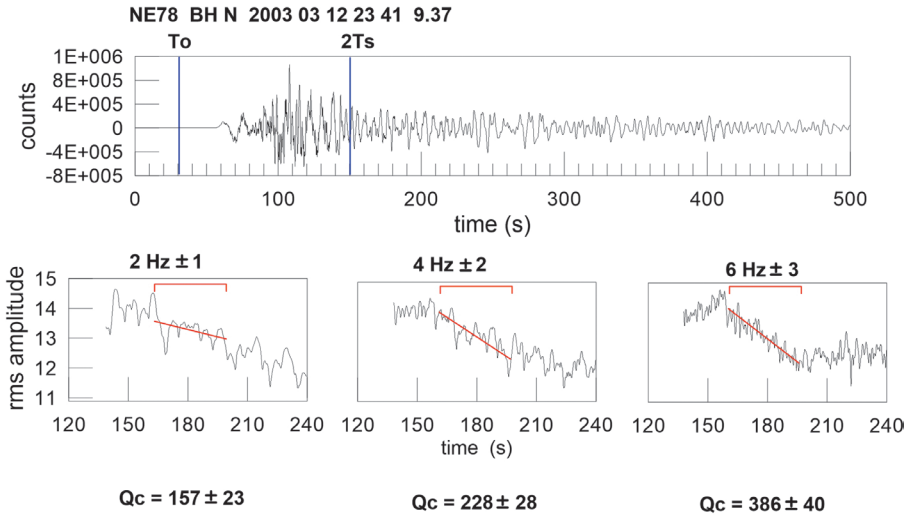

Figure 3. Coda Q_C estimation procedure. The unfiltered seismogram is shown at the top. *rms* amplitudes *vs* lapse time for the time window indicated at the different frequency bands are shown below.

used for Q_C estimation. These events included four events with M>5 and their aftershocks.

Each record was bandpass-filtered for seven frequencies between 1 and 7 Hz with an eight-pole Butterworth filter and bandwidths of two-thirds of the center frequency

rms amplitudes were determined for sliding windows of 2 seconds width and 1 second advance. Assuming that noise is not correlated with signal, the seismogram can be considered as a linear superposition of noise and signal. Corrected amplitudes (A_C) were calculated using

$$A_c = (A_T^2 - A_N^2) \qquad (3)$$

where A_N is the maximum amplitude (*rms*) of the noise and A_T is the actual amplitude (*rms*) of the seismic record. For each band, *rms* amplitudes of a representative window of noise before the P arrival and corrected *rms* amplitudes were calculated according to (3).

A_C versus t was plotted and fitted a straight line by a least squares method to calculate the slope from which was obtained. The lower bound of the time window started always after twice the S-wave travel time. The upper bound was usually given by the change of the trend of $A(t)$. The time windows selected in this way were between 20 and 65 s in all cases. Figure 3 shows an example of this procedure. The unfiltered seismogram is shown at the top, below it, the *rms* amplitudes from the bandpass filtered windows, and the fitted line for the selected time window. Q_C estimated values for each frequency are also shown.

Results

Q_C average was obtained at each station for central frequencies 1 to 7 Hz. Figure 4(up) shows the values for the six stations and a comparison of the Q_C values estimated for the different stations, from December, 1997, to May, 1998, (down). Vertical bars indicate standard deviation in Q_C estimation (±1s).

Some observations can be drawn from this figure. Within the bounds of the variation, it can be seen that Q_C values at each frequency are similar between stations and the general trend is the same for all of them. Assuming a power law of the form $Q_C(f) = Q_0 f^a$, we averaged Q_C values and obtained a value of Q_0 = 82±3 and a frequency-dependence α value of 1.05±0.03 in the frequency range from 1 to 7 Hz.

Lapse time used to evaluate Q_C and epicentral distance are related to the size of the sampled region. For a source in a homogeneous half-space with random scatters, scattered energy arriving at time t in the coda comes from scatterers lying on an ellipsoidal shell, which surface projection is defined by

$$\frac{x^2}{(vt/2)^2} + \frac{y^2}{(vt/2)^2 - (r/2)^2} = 1 \qquad (4)$$

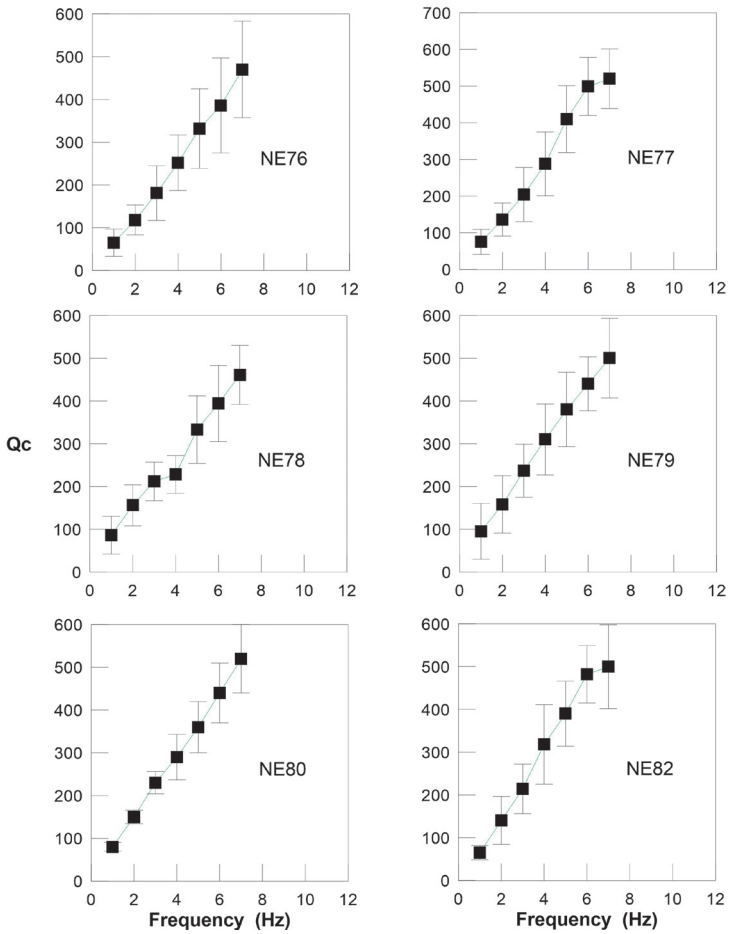

Figure 4. Coda Q_C values obtained for different stations. Vertical bars indicate standard deviation in Q_C estimation.

Figure 5. North and South subregions of Gulf of California for attenuation analysis.

where r is the source-station distance, v is the wave velocity (averaged S-wave velocity of the model of Table 2), and x and y are the surface coordinates (Pulli, 1984).

Ellipses for each source-station pair were plotted and an envelope was drawn. Two subregions could be defined; the first one with stations to the south of the epicenters (NE78 and NE79) and the second one with the other stations including the most northern station (NE80, Figure 5) since the region between NE80 and the cloud of epicenters to have similar characteristics were considered. Attenuation-frequency dependency function for the north subregion was of $(85\pm3)f^{1.03\pm0.03}$ and of (75 ± 3) $f^{1.07\pm0.03}$ for the south subregion. Q for the closest stations to the epicenters cloud (NE76, NE77 and NE82, distances between 40 a 200 km) were also estimated in order to see if there was a significant difference for this smaller region,obtaining $(83\pm3)f^{1.16\pm0.03}$. A higher value of the frequency-dependence α which could be expected as this zone correspond to events occurrence, and can be considered as the most heterogeneous zone.

Discussion and Conclusions

In this study an estimation of averaged value of parameter coda attenuation($Q_c\ (f\ )$) was obtained for the center and south of the Gulf of California, Mexico.

The obtained relation, shows that attenuation is highly dependent on frequency which is in agreement with the high tectonic activity of the Gulf.

A slightly higher attenuation in the south subregion was observed. Oceanic crust is reported to be thinner in this region (López-Pineda, 2007). Lonsdale (1989) suggested the presence of a transitional crust at the Guaymas basin in the middle sector of the Gulf of California. In this location, there is a high rate of sedimentation, which promoted the development of a basin containing sills and altered sediments. The greater earthquakes occur in central to south Gulf of California (M>6). We can thus infer that the southern region is more fractured than the northern one, explaining the observed difference in attenuation.

For a small zone of 1.5x1.5 degrees located inland (northeastern Sonora state) within the north subregion (region of the 1887, Mw 7.5 earthquake rupture zone which included the Otates, Teras and Pitáycachi faults), Castro *et al*. (2008) found an S-wave attenuation-frequency dependent function Q_S = 83.8 $f^{0.9}$. Very similar values to those obtained in the present study. They suggested scattering to be an important mechanism controlling the decay of spectral amplitudes. The higher frequency dependence in the present case could be

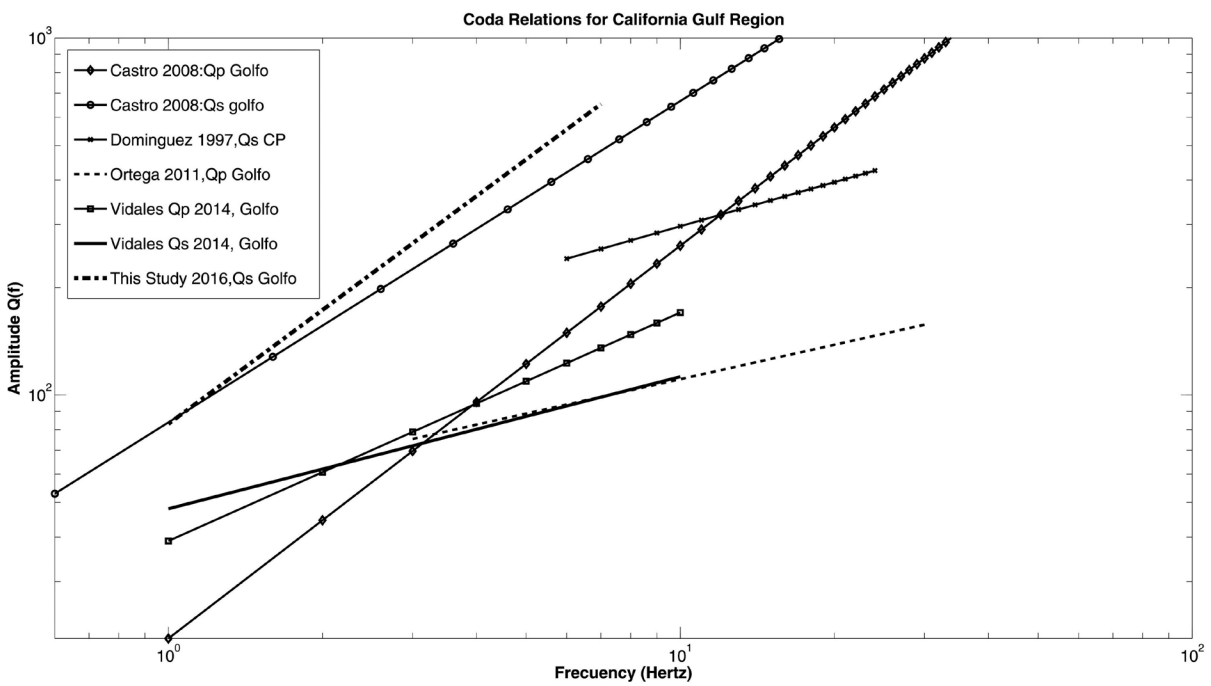

Figure 6. Comparison of Q values found in the California and the Gulf of California regions

reflecting the paths that approach the boundary between the North America and Pacific plates where higher heterogeneity is to be expected, the thickness of the crust is thinner, and new ocean floor is being created.

To the north from the Gulf of California, some attenuation studies have been performed: Reyes *et al*. (1982) obtained Q_C = 250, independent of frequency between 5 and 12 Hz using aftershocks of the 1980 Victoria earthquake, using spectral ratios. Another study of attenuation was made at Imperial fault region by Singh *et al*. (1982); they used a spectral approach to estimate attenuation of SH waves and obtained a linear functional relation of Q_S = 20 $f^{1.0}$ in the frequency range from 3 to 25 Hz. Dominguez *et al*. (1997), found Q_C = 111.5 $f^{0.41}$ between 6 and 24 Hz for a small area (less than 10 km) around the Cerro Prieto Geothermal field. More recently, Vidales *et al*. (2014) studied attenuation of the same region of this study but restricting their source-station paths up to 220 km. They found Q_S = 176 $f^{0.6}$ for distances up to 120 km and Q_S = 48 $f^{0.37}$ for 120-220 km. Similar values to those obtained by Ortega and Quintanar (2011) for the southern zone of the Gulf of California (Q_p = 56 $f^{0.3}$) which are very different from that obtained by Castro *et al*. (2008) of Q_p = 20.8$f^{1.1}$ for the Sonora Region. Although they are different regions (Sonora is part of the basin and range province), no such differences were to be expected, specially the differences in frequency dependence (Figure 6).

References

Aki K., Chouet B., 1975, Origin of coda waves: source, attenuation, and scattering effects. *J. Geophys. Res*. 80, 3322-3342.

Castro R., Munguia M. 1993, Attenuation of P and S waves in the Oaxaca, Mexico Subduction zone. *Phys. Earth Planet. Interiors.,* 76, 179-187.

Castro R., Munguia M., Rebollar C., Acosta J. 1994, A comparative analysis of the quality factor Q for the regions of Guerrero and Oaxaca, Mexico. *Geofisica Internacional*. 33, 3, 373-383.

Castro R.R., Méndez I., Pérez-Vertti A., Mendoza A., Inzunza L., 2007, Seismicity in the Gulf of California region recorded by the NARS-Baja array: Preliminary results, Eos Trans. AGU 88, 23, Jt. Assem. Suppl., Abstract S31A-08.

Castro R., Condori C., Romero O., Jacques C., Suter M., 2008, Seismic Attenuation in Northeastern Sonora, Mexico. *Bull. Seism. Soc. Am*. 98, 2, 722-732.

Curray J.R., Moore D.G., Keitz K., Einsele G., 1982, Tectonics and geological history of the passive continental margin at the tip of Baja California: Initial Reports of the Deep Sea Drilling Project, Leg. 64, Part 2, XLIV, 1089-116.

Domínguez T., Rebollar C., Fabriol H., 1997, Attenuation of coda waves at the Cerro Prieto geothermal field, Baja California, México. *Bull. Seism. Soc. Am*., 87, 1368-1374.

Domínguez T., Flores C.F., Reyes D.G., 2003, Temporal change in coda wave attenuation observed at Volcán de Colima, México before the 1998 eruption. *Journal of Volcanology and Geothermal Research*, 125, 215-223.

Fenby S.S., Gastil R.G., 1991, A seismo-tectonic map of the Gulf of California and surrounding areas, in Dauphin, J.P., and Simoneit,B.R., eds., The Gulf and Peninsular Province of the Californias: American Association of Petroleum Geologists Memoir 47, p. 79–83.

Jin A., Cao T., Aki K., 1985, Regional change of coda Q in the oceanic lithosphere. *J. Geophys. Res*. 90. 8651-8659.

Lienert B., Berg E., Frazer L., 1986, HYPOCENTER: An earthquake location method using centered, scaled, and adaptively damped least squares, *Bull. Seis. Soc. Am*., 76, 771-783.

Lienert B.R., Havskov J., 1995, A computer program for location earthquakes both locally and globally, *Seism. Res. Lett*., 66, 26-36.

Lonsdale P., 1989, Geology and tectonic history of the Gulf of California, in Winterer, E.L., *et al*., eds., The Eastern Pacific Ocean and Hawaii:Boulder, Colorado, Geological Society of America, Geology of North America, v. N, p.499–521.

López-Pineda L., Rebollar C.J., Quintanar L., 2007, Crustal thickness estimates for Baja California, Sonora and Sinaloa, Mexico, using disperse surface waves. *J. Geophys. Res.,* 112, B04308. doi:10.1029/2005JB003899

Nagy E.A., Stock J.M., 2000, Structural controls on the continent-ocean transition in the northern Gulf of California, *Journal of Geophysical Research*, 105 (B7), p. 16.251-16,269.

Ordaz M., Singh S., 1992, Source spectra and spectral attenuation of seismic waves from Mexican earthquakes and evidence of amplification in the hill zone of Mexico City. *Bull. Seism. Soc. Am*., 82, 24-43.

Ortega Ruiz R., Quintanar Robles L., 2011, A comparison between P- wave and S-wave propagation characteristics in the southern part of the Gulf of California, Mexico. *Bull. Seism. Soc. Am.,* 101, 3, 1270-1280.

Ottemöller Voss, Havskov, 2013, Seisan Earthquake Analysis Software for Windows, Solaris, Linux and MacOSX.

Pacheco J.F., Sykes L.R., 1992, Seismic moment catalog of large,shallow earthquakes, 1900–1989, *Bull. Seism. Soc. Am*., 82, 1306–1349.

Persaud P., Stock J.M., Steckler M., Martin-Barajas A., Diebold J.B., Gonzalez-Fernandez A., Mountain G., 2003, Active deformation and shallow structure of the Wagner, Consag and Delfin Basins, Northern Gul f of California, Mexico. *Journal of Gephysical Research*, 108, 7.

Plattner C., Malservisi R., Dixon T.H., LaFemina P., Sella G.F., Fletcher J., Suarez-Vidal F., 2007, New constraints on relative motion between the Pacifi c plate and Baja California microplate (Mexico) from GPS measurements: *Geophysical Journal International*, 170, p. 1373–1380, doi:10.1111/j.1365-246X.2007.03494.x.

Pulli J.J., 1984, Attenuation of coda waves in New England, *Bull. Seism. Soc. Am.,* 74, 1149-1166.

Rebollar C.J., Quintanar L., Castro R., Day S.M., Madrid J., Brune J.N., Astiz L., Vernon F., 2001, Source characteristics of a 5.5 magnitude earthquake that occurred in the transform fault system of the Delfin basin in the Gulf of California, *Bull. Seismol. Soc. Am.*, 91, 781–791.

Reyes A., Chang A., Albores A., 1982, Atenuación y origen de las ondas de coda en la región del campo geotérmico de Cerro Prieto, *Proceedings Cuarto simposio sobre el campo geotérmico de Cerro Prieto, Baja California, México,* 1, 77-105.

Sato H., 1977, Energy propagation including scattering effects: single isotropic scattering aproximation. *Phys. Earth Planet. Inter*., 25, 27-41.

Singh S.K., Aspel R.J., Fried J., Brune J.N., 1982, Spectral attenuation of SH waves along the imperial fault. *Bull. Seismol. Soc. Am*., 72, 2003-2016.

Trampert J., Paulssen H., A. van Wettum, Ritsema J., Clayton R., Castro R., Rebollar C., Perez-Vertti A., 2003, NARSBaja:monitoring the Gulf of California, Mexico, EOS.

Vidales-Basurto C.A., Castro R.R., Huerta C.I., Sumy D.F., Gaherty J.B., Collins J.A., 2014, An attenuation Study Body Waves in the South-Central Region of the Gulf of California, México. *Bull. Seismol. Soc. Am.*, 104, 4, doi: 10.1785/0120140015.

Wiggins-Grandison M., Havskov J., 2004, Crustal attenuation for Jamaica, West Indies. *Journal of Seismology*, 8, 193–209.

Geofísica Internacional (2017) 56-2: 147-155

Original paper

Radiometric and seismic study of Chidvinskaya kimberlite pipe (Arkhangelsk diamondiferous province, North of the East European Craton, Russia)

Kiselev Georgij*, Danilov Konstantin, Yakovlev Evgenij and Druzhinin Sergej

Received: February 25, 2016; accepted: October 11, 2016; published on line: April 01, 2017

Resumen

Se realizaron cálculos geofísicos superficiales en el pasaje de diamante Chidvinskaya de la provincia productora de diamantes de Arkhangelsk (Norte del Craton de Europa Oriental, Rusia). Dichos cálculos incluyeron un estudio gamma-espectrométrico de alta precisión, una estudio de emanación de radón en el aire del suelo y un método de sondeo microsísmico. Se utilizáron cálculos radiométricos para encontrar anomalías de radiactividad de la capa superficial sobre el tubo de Chidvinskaya, el cual podría ser un resultado del impacto del cuerpo kimberlita en un medio huésped. Con la estructura profunda de la pasaje de kimberlita y el medio huésped se formó una imagen mediante el método de sondeo microsísmico. Los resultados indican que el tubo aparece como un cuerpo de alta velocidad. El medio huésped es de baja velocidad que es típico de las rocas con fisuras excesivas. Los valores aumentados de la radiación de rayos gamma total de la capa superficial cercana se observan dentro del contorno de la tubería y superan los valores de fondo de 2 a 4 veces. Se encontró emanación anómala de radón en el aire del suelo en los límites de las tuberías. De acuerdo con los datos de sondeo microsísmico, la zona de contacto cercano es una estructura permeable al gas con excesiva fisuración. Los resultados de los métodos utilizados concuerdan entre sí. El complejo de métodos propuesto ha permitido identificar la característica distintiva de la tubería.

Palabras clave: estudio gamma-espectrométrico, emanación del radón, microseísmo, tubería de Chidvinskaya, provincia diamantífera de Arkhangelsk.

Abstract

Surface geophysical measurements were carried out on Chidvinskaya diamond pipe of the Arkhangelsk diamondiferous province (North of the East European Craton, Russia). Geophysical measurements included a high-precision gamma-spectrometric survey, radon emanation survey in soil air, and microseismic sounding method. Radiometric measurements were used to found radioactivity anomalies of the surface layer over the Chidvinskaya pipe which could be a result of impact of the kimberlite body on a host medium. Deep structure of the kimberlite pipe and host medium was imaged by means of microseismic sounding method. Results indicate that the pipe appears as a high-velocity body. The host medium is low-velocity that is typical for rocks with excessive fissuring. Increased values of total gamma-ray radiation of near surface layer are observed within the pipe contour and exceeded the background values by 2-4 times. Anomalous radon emanation in the soil air was found at the pipe boundaries. According to the microseismic sounding data near-contact zone is a gas-penetrable structure with excessive fissuring. The results of the used methods are in good agreement with each other. The proposed complex of methods has allowed to identify the pipe distinctive feature.

Key words: gamma-spectrometric survey, radon emanation, microseisms, Chidvinskaya pipe, Arkhangelsk diamondiferous province.

K. Georgij*
D. Konstantin
Y. Evgenij
D. Sergej
Institute of Ecological Problems of the North
Ural Branch of Russian Academy of Sciences
Northern Dvina Embankment 109, 163000
Arkhangelsk, Russia
*Corresponding author: kiselevgp@yandex.ru

Introduction

Since the discovery of the first kimberlite pipe in the Arkhangelsk diamondiferous province (ADP) (North of the East European Craton, Russia) many traditional geophysical methods have been tested with the purpose to search new kimberlite bodies (Bezborodov *et al.,* 2003; Kontarovich & Babayants 2011). Aeromagnetic methods have shown the most effective (Mwenifumbo & Kjarsgaard 1999; Reed & Witherly 2007). However, at the present time crisis of the efficiency aeromagnetic survey to searching kimberlite bodies influences on the searches results increasingly. Thus, in the early eighties of the last century the efficiency verification magnetic anomalies was about 20 %; at the end of the eighties, 12.5 %; in the nineties it was already below 1 % (Stognij & Korotkov 2010). Today, this figure is less than 0.5% for the whole territory of the Arkhangelsk diamondiferous province. It is connected with a decrease of contrast magnetic anomalies which are tending to geological noise. Therefore, development of new approaches for exploration and prediction of kimberlite pipes are an important task.

One such approach is a complex use of surface geophysical methods such as a high-precision gamma-spectrometric survey, radon emanation survey in soil air and microseismic sounding. According to the microseismic sounding (MSM) method, kimberlite pipes appear as vertical zones with values of relative microseismic intensity lower than 5 dB. Kimberlite pipes are accompanied by faults with higher values of the relative intensity of MS (*Popov et al. 2014*). Gamma-spectrometric studies are used widely to search for uranium ore with high efficiency (IAEA, 2003; Babayants *et al.,* 2015; Killeen *et al.,* 2015). Also, radiometric studies have shown that total gamma-ray radiation and concentration of radioactive elements are increased in near surface layer. The boundaries of kimberlite pipes are accompanied by anomalous radon emanations.

Furthermore, as an example at Arkhangelskaya kimberlite pipe it was found that secular radioactive equilibrium of the even uranium isotopes is disturbed in enclosing rocks of the near-contact zone. Similarly, the radioactive elements concentrate inside that zone (Yakovlev *et al., 2016*).

The objective of the present work is to study Chidvinskaya pipe of the Chidvinsko-Izhmozerskoe kimberlite field of ADP. This pipe was selected because of its relatively large size and low overburden thickness that is important for radiometric measurements. The pipe's dimensions exceeded the resolving power of the microseismic sounding method (MSM) and allowed to expect a more reliable determination of the deep structure.

General characteristics of the research object

Chidvinskaya pipe is part of the Chidvinsko-Izhmozerskoe kimberlite field, located 30 kilometers north-east from Arkhangelsk, and belonging to a membership of six pipes, constituting a chain with about 20 kilometers length to the North-North-East (Figure 1).

Chidvinskaya pipe is 1810x580 m. The pipe has low-grade ores without commercial value. However, a small amount of tests casts doubt on the accuracy of these estimates.

The complex overburden rock presented quaternary loose sediments, made mainly of sands, loams, peat and sand-pebble formations. Overburden thickness change from 1.5 to 35.3 m northern and southern part of the pipe. The average thickness of quaternary sediments is about 9.4 m.

The vertical section of Chidvinskaya pipe is two-root diatreme with a common trumpet in the surface portion. The upper part of the pipe is formed by rocks of crateral facies which are divided into two bench, the top and bottom bench with total capacity of about 123.5 m.

Top bench is composed of tuffaceous sedimentary rocks represented by coarse sandstones with an admixture of magmatic material, tuff-sandstones, tuffites and tuffs. Bottom bench is distributed in the northern part of the pipe and is made by tuffites with rare interlayers of tuffs and tuff-sandstones.

Diatreme facies is composed by autolit breccias, tuff breccias that form two ore pillars. The boundary between them is held in the middle bottleneck zone. Contacts between the diatreme rocks and the surrounding sedimentary deposits are quite clear.

Experimental

Surface geophysical measurements including high-precision gamma-spectrometric survey, radon emanation survey in soil air and microseismic sounding were used.

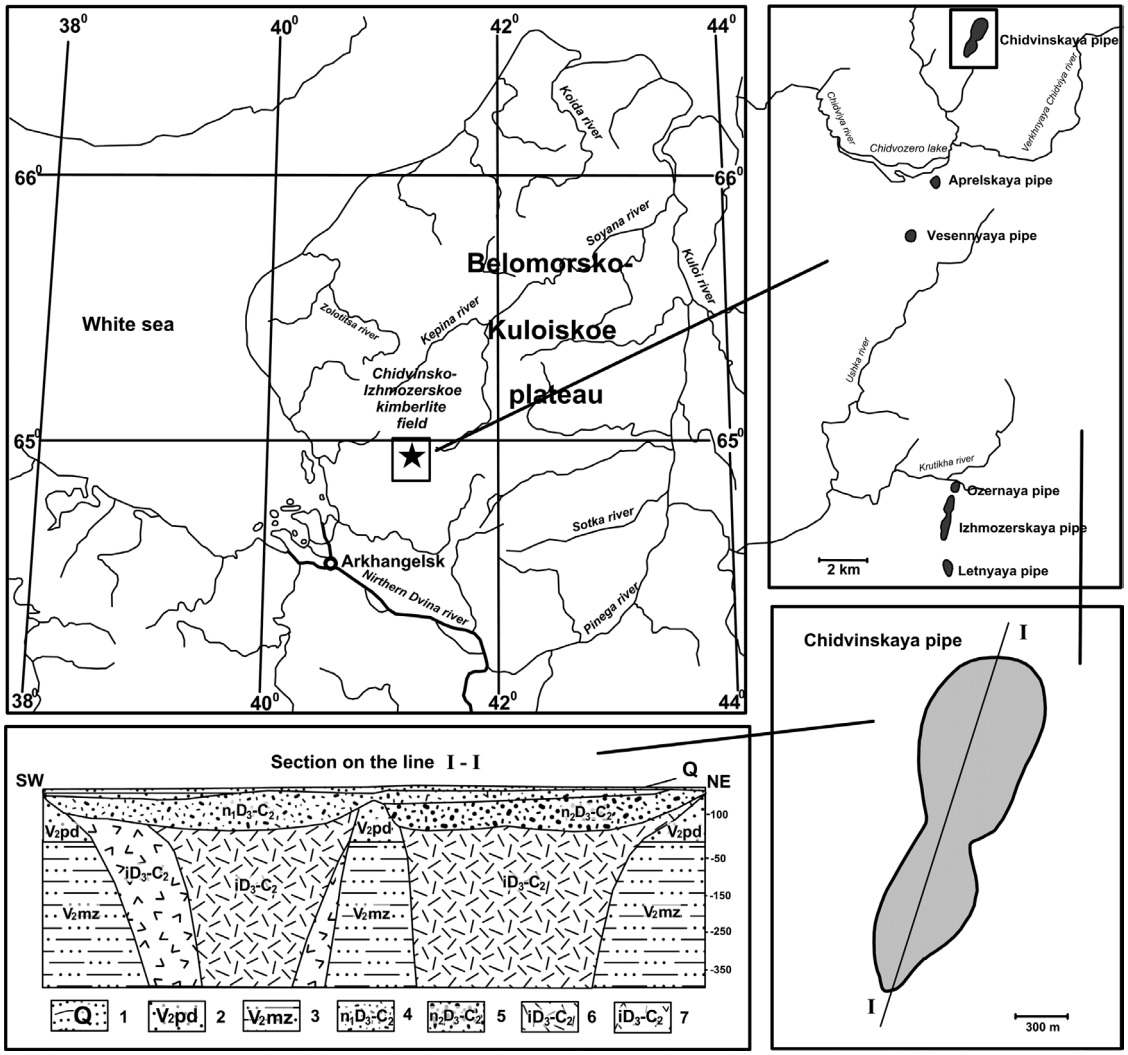

Figure 1. Location of the pipes of Chidvinsko-Izhmozerskoe kimberlite field and structure of the Chidvinskaya pipe (section by Eremenko (2004).

1.- quaternary deposits (sandy loams, loams, sands, clays); 2.– padun suite of vendian system (sandstones, argillites, siltstones); 3.– mezen suite of vendian system (siltstones, argillites, sandstones); 4.– top bench of crateral facies (tuffaceous sandstones with interlayers tuffs and tuffites); 5.– bottom bench of crateral facies (tuffites with interlayers tuffs); 6.– autolith breccias of diatreme facies; 7.– tuff breccias of diatreme facies.

Gamma-spectrometric survey

During the opening of the first diamond-bearing pipes of ADP gamma-spectrometric survey was used in combination with traditional geophysical methods, but it didn't receive further development, although it has been shown that kimberlite bodies were accompanied by radiation field anomalies in well landscape and geological setting (Babayants *et al.,* 2015). Kimberlite pipes of Yakut diamondiferous province were characterized by increased concentrations of thorium according to the airborne gamma-spectrometric measurements (Tsyganov *et al.,* 2004). Diamond deposits of tuffizit type were characterized by high-radioactivity in areas with low thickness of covering deposits (Rybalchenko *et al.,* 2011).

Surface gamma-spectrometric studies in the area of Chidvinskaya pipe were performed in pedestrian options using high-precision mobile scintillation gamma spectrometric complex RS-700 (Canada). Complex RS-700 is an advanced high resolution (1024 channels) digital spectrometer (ADS) allowing real-time to perform measurements of total radioactivity (Bq m^{-3}), as well as a separate measurement of the concentration of total uranium (μg/g), thorium (μg/g) and potassium in percentages

(%). The complex is equipped with an integrated GPS-receiver, enabling precise measurement of each binding. Complex RAD Assist software is used, that may directly conduct processing of the data in the field.

The traverse survey was carried out at a relatively uniform network with increments of 50 - 100 m. The measurements were made at 1.2 m above the ground. In total more than 16800 measurements, were performed using the gamma-spectrometric complex RS-700.

Radon emanation survey

^{222}Rn is a member of the ^{238}U radioactive series (Abumurad & Al-Tamimi 2001). Radon in the earth's surface depends on the characteristics of geological structure of the territory: development of plutonic rocks, permeable zones (faults), groundwater dynamics, presence of hydrocarbon accumulations, etc. (Bossew 2003). Heightened concentrations of radon are associated with tectonic faults, where it enters on the system of joints and tiny fractures and with fracturing persilicic intrusive mass (King, 1980). Zone crushing rocks surrounding these faults are feeders for radon (Kikaja *et al.,* 2016). Fractured rocks can increase the *in situ* local radon concentration, hence increasing the radon signal.

Measurements of radon emanation in soil air above Chidvinskaya pipe were conducted on the profile that crosses the north pole of the pipe in north-west – south-east direction using an automatic radium emanation radiometer RRA-01M-03 (Figure 2).

For the measurement of radon in soil air, drilling of pits to 0.5 m depth and 0.2 m diameter using soil portable drilling rig were conducted. The gas collector was placed to pit, then gas was pumped out from soil into the ionization chamber of the radiometer. After that radon measurement was conducted. The values of radon emanation were obtained for the 16 observation points.

Microseismic sounding method

The microseismic sounding method (MSM) was implemented on the assumption that the vertical component microseisms are determined mainly by the contribution of the fundamental mode of Rayleigh waves (Bath 1979). According to the results, two regularities were noted (Gorbatikov & Tsukhanov 2011; Gorbatikov *et al.,* 2013):

1) power spectrum amplitudes of Rayleigh waves increases when passing through low-velocity heterogeneities and decreases when passing through high-velocity heterogeneities;

2) the greatest change in intensity is observed for wavelengths twice the size of the cover thickness of the heterogeneity. This can be explained by the fact that a shear stress zone of Rayleigh wave is located at a depth equal to half of the length of a wave. As this takes place, the shift zone is located closer to surface.

The first statement on a qualitative level was predicted theoretically by Savarenskii and Kirnos, (1955). The close conclusions were reached at independent research of Rayleigh waves amplifications (Lin*, et al.,* 2012; Eddy and Ekström, 2014)

In the MSM it is necessary to define an indicative spectrum of microseisms for each point of measuring. For this purpose microseisms are accumulated during the period of stationarity equal to 1.5 hours duration (Gorbatikov & Stepanova, 2008).

Processing of the data starts with the construction of power spectra. Next, each frequency is studied individually. The relative intensity (I_i) of microseisms between the reference and mobile stations is calculated as

$$I_i = 20 \cdot log_{10} \frac{A_{ip}}{A_{ip}} \qquad (1)$$

where A_{ip} and A_{io} are the spectral amplitudes for recordings at the i^{th} point of the mobile and reference stations at the considered frequency.

The next step is the determination of the depth to be sounded which is equal to a half of the wavelength. The wavelength is determined based on the most probable velocity model of the investigated object.

The result of this processing is a distribution diagram of relative intensity of microseisms along the profile by depth. Zones with a higher relative microseism intensity represent an area with relatively reduced velocity properties, and vice versa.

Due to the fact that the microseismic sounding method is aimed at the vertical and near-vertical boundaries, it can be used for the allocation of various geological objects, including faults and kimberlite pipe.

The microseismic sounding method was successfully tested on a number of tubes of the kimberlite pipes (Gorbatikov *et al.,* 2009; Popov *et al.,* 2014)

Microseisms were measured along the profile that crosses the northern block of the pipe Chervinskaya. The central part of the profile of (MSM) coincided with the route of radon emanation survey (Figure 2). Microseisms were measured by the seismic equipment of production Guralp (Great Britain).

Records of microseisms were processed in a complex DAK program (*Popov et al. 2014*).

Results and discussion

Gamma-spectrometric studies

Figure 2 shows the map of total gamma-ray distribution of near surface layer above Chidvinskaya pipe. The total radioactivity of rocks varies widely from 172 to 1585 Bq m^{-3}. The distribution of high gamma-field has a slightly wide configuration than the pipe contour. The most contrast and the biggest area of increased gamma-ray values is confined to the northern part of the pipe and localized within the north pole, where thickness overburden of quaternary sediments is minimal and is about 1.5 m. Value of total radioactivity reached 1500 Bq m^{-3}.

Spatial distribution of high values of total gamma-ray radiation of near surface layer above Chidvinskaya pipe forms a linear anomaly of northeast trending which goes beyond contour of the pipe. Average values of radioactivity are about 800-900 Bq m^{-3} outside this area.

Concentration of thorium in Chidvinskaya pipe area varies within 0.5 - 14.0 μg/g. The maximum values of thorium are localized at small areas and are arranged substantially within the contour of the pipe. The potassium content ranges from 0.3 to less than 3.8%. The spatial distribution picture of potassium content in general is identical to the index of total gamma-ray radiation and forms an area of high values within pipe contour, especially in the northern part of the pipe where thickness overburden of quaternary sediments is minimal. Uranium concentration ranges from less than 0.4 to 4.6 μg/g. Distribution picture of uranium isn't unambiguous. Explicit spatial confinement to the contour of the pipe wasn't observed.

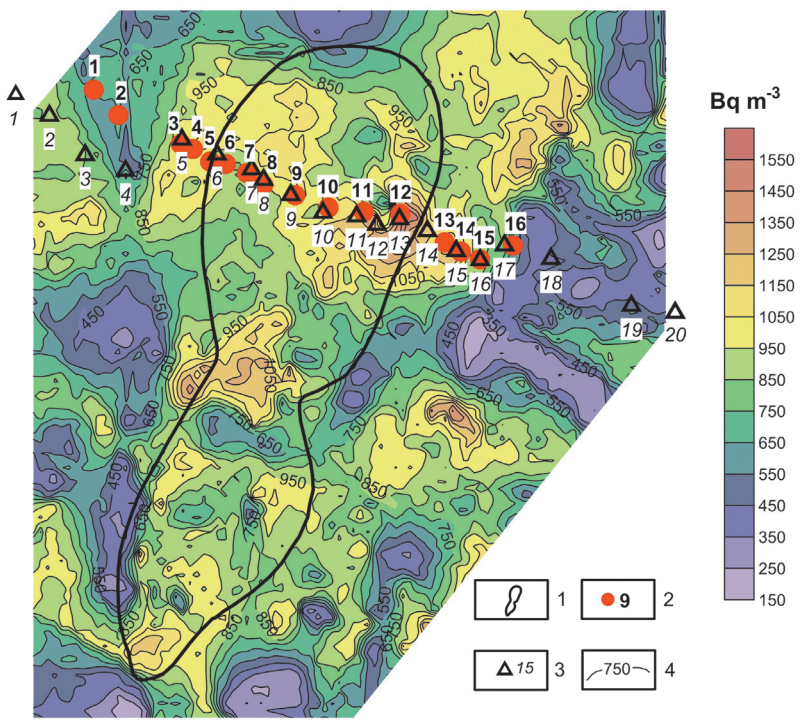

Figure 2. Distribution of total gamma-ray radiation above Chidvinskaya pipe.
1.- Chidvinskaya pipe contour; 2.- point measurement of radon emanation in the soil air; 3.– MSM measuring points; 4.- contour lines of gamma-ray radiation intensity.

In general, it can be noted that Chidvinskaya pipe have increased values of gamma radiation, as well as potassium. Distribution of thorium and uranium concentration doesn't have areal disposition that apparently is a consequence of erosional feature of top bench craterial facies Chidvinskaya pipe.

Radon emanation results

Traverse of radon method included 16 observation points. Points of observation are shown in Fig. 2. The results are shown in Table 1.

Radon radioactivity in the soil air ranges from 114 to 1312 Bq/m^3 on the profile that crosses the north pole of Chidvinskaya pipe. Variation of values radon emanation are insignificant within the contour of the pipe from 185 to 312 Bq/m^3. Anomalous increase of radon concentrations was observed at the boundaries of Chidvinskaya pipe.

Maxima of radon radioactivity in soil air were obsewrved at the north-western and south-eastern borders of the profile, 1156 Bq/m^3 and 1312 Bq/m^3, respectively. ^{222}Rn radioactivity falls sharply and decreases to a minimum beyond the boundaries of the pipe.

Revealed regularities of radon changes on the profile can be elucidated by the fact that the contacts of kimberlite pipe with the enclosing rocks are fractured faults zones with high permeability.

Microseismic sounding results

The results of MSM are shown in Figure 3 were the high-velocity tube body is allocated at observation points 6 - 15. The border dividing the western and eastern blocks of a pipe has an inclination of about 45 degrees at depths up to 400 m. Deeper than 400 m all borders remain almost vertical. Eastern block is traced up to the depths more than 1000 m despite the small sizes in deep part of a section. The pipe differ from environment in 2-7 dB by relative microseism intensity. The western and east blocks of pipe differ from each over about 2-5 dB by relative microseism intensity. According to (Gorbatikov & Tsukhanov 2011) these relative microseism intensity changes correspond to velocity properties changes in 1.5-2 times and 1.2-1.5 times.

The allocated pipe is limited by contrast linear, vertical low-velocity zones from the West and the East. These zones are likely caused by faults in endocontact rock. These faults are traced at the depths of 200-1000 m under points 5 from the West and 15-16 from the East. Also, the vertical low-velocity zones can be traced for 300-400 m off pipe to the west and east.

Table 1. Radioactivity ^{222}Rn in soil air above Chidvinskaya pipe.

Number of measuring points	Coordinates of measuring points N	E	Radioactivity ^{222}Rn, Bq/m^3 (± absolute error)
1	64.95030	41.11813	114±20
2	64.94983	41.11915	682±115
3	64.94927	41.12177	1156±184
4	64.94917	41.12228	545±98
5	64.94893	41.12300	238±49
6	64.94888	41.12367	195±42
7	64.94870	41.12455	185±42
8	64.94848	41.12522	248±52
9	64.94827	41.12657	300±57
10	64.94803	41.12798	312±58
11	64.94793	41.12948	201±42
12	64.94787	41.13103	254±53
13	64.94733	41.13288	254±53
14	64.94715	41.13357	857±145
15	64.94700	41.13437	1312±209
16	64.94723	41.13580	212±44

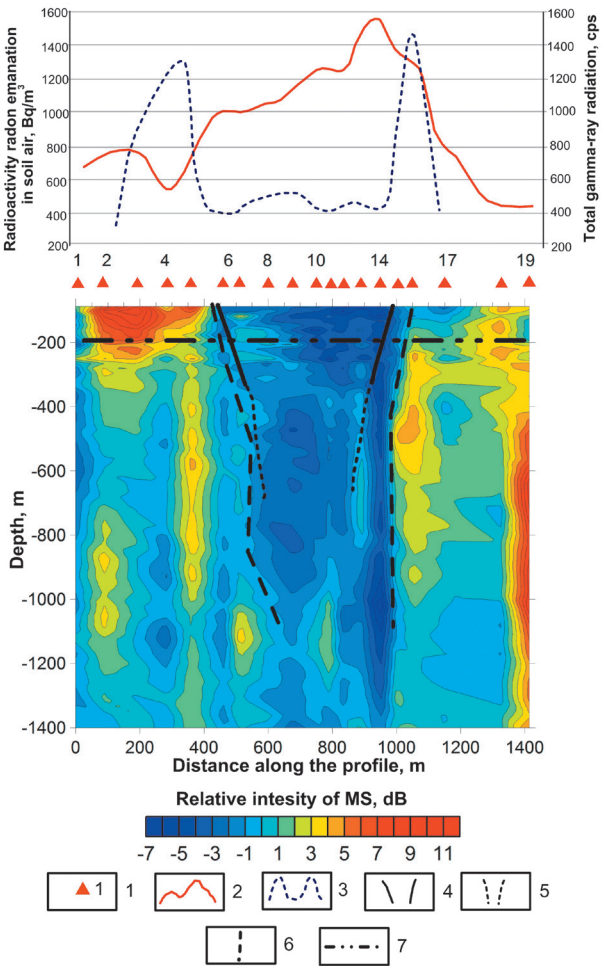

Figure 3. The depth section of relative intensity distributions of microseisms and radiometric parameters along the profile crossing Chidvinskaya pipe. 1.- point measurements of MS; 2.- curve of change the total intensity of the gamma-ray radiation, Bq m^{-3}; 3.- curve of change of radon emanation in soil air, Bq/m^3; 4.- Chidvinskaya pipe border for geological exploration data; 5.- proposed structure of diatreme facies; 6.- side pipe body according to MSM; 7.- border Padun and Mezen suites of Vendian.

In near-surface area the most contrast low-velocity body is observed under points 2-5 at depths from 40 to 200 m and has a cone-shaped structure. According to (Gorbatikov & Tsukhanov 2011). this contrast approximately correspond to velocity decreasing of 2-3 times. Also vertical low-speed zones are traced on removal from a pipe body on 300-400 m to the West and the East.

The changes in the configuration consistent with the changes in the intensity of the allocated zones allow to place the layer in the crust at about 200 m depth, and corresponds to boundary of Padun and Mezen suites of the top of Vend.

When comparing the results we observe an increase of the total gamma gamma-ray radiation consistent with MSM, that corresponds to a high-velocity anomaly. Intensity of gamma radiation on the high-speed anomaly is greater than 2-4 times for background values of enclosing rocks. At the same time, there is a decrease of total gamma radiation from western to eastern blocks of the pipe body. Such a significant change of the gamma radiation level and high-speed characteristics may indicate different material composition of the Western and Eastern pipe blocs. This difference can indicate either different implementation phases, or that data block was subjected to various (physical, metamorphic, erosive) processes after the formation of the tube.

Anomalous radon concentrations at the boundaries of Chidvinskaya pipe are appropriate contrasting linear low-velocity zones. As a dedicated fault structures, there is a possible influx of radon and other gases. High-velocity nature of the pipe body indicates a consolidated structure and a minimum influx of ^{222}Rn. High velocity nature of the pipe body can be explained by the sharply different composition of the pipe and enclosing medium.

The proposed set of methods can be used in further studies, since the methods showed a good convergence of results.

Conclusions

The results of the radiometric and seismic studies including high-precision gamma-spectrometric survey, radon emanation survey in soil air and microseismic sounding method in the area of Chidvinskaya pipe of the Chidvinsko-Izhmozerskoe kimberlite field ADP are as follows:

1. The method of surface gamma-ray spectrometric survey showed that Chidvinskaya pipe against the backdrop of the deposits are allocated increased values of gamma-field, as well as potassium, especially in the northern part with minimum thickness overburden quaternary sediments.

2. Anomalous radon has fixed on lips of the pipe. Probably, it is linked with excessive fissuring of host sediments which appear in the form of contrasting high-velocity zones on MSM data.

3. The method of MSM was conducted clarifying the deep structure of the pipe and enclosing environment. Chidvinskaya pipe manifests as a high- velocity body.

4. The consistency of the results with each other and with the known geological and geophysical information indicates the validity of the data.

References

Abumurad K., Al-Tamimi M., 2001, Emanation power of radon and its concentration in soil and rocks. *Radiat. Meas.*, 34, 423–426.

Babayants P.S., Kertsman V.M., Levin F.D., Trusov A.A., 2015, Special features of the state-of-the-art airborne gamma-spectrometry. *Prospect of mineral resources*, 12, 10-15.

Bath M., 1979, Spectral Analysis in Geophysics, *Elsevier Scientific Publ. Co., Amsterdam, Oxford, New York*, 539.

Bezborodov S.M., Verzhak V.V., Gerasimchuck A.V., 2003, Diamond exploration and mining in north-west of Russia: 4th Fennoscandian exploration and mining. Final Program and Event Document. - Rovaniemi, 279-304.

Bossew P., 2003, The radon emanation power of building materials, soils and rocks. *Appl. Radiat. Isot.*, 59, 389–392.

Eremenko A.V., 2004, Osobennosti sostava khromshpinelidov trubok vzryva Izhmozjorskogo polya Arhangel'skoj almazonosnoj provintsyi kak otrazhenie geodinamiki ikh formirovaniya // *Vestnik Voronezhskogo universiteta, Geologiya*, 1, 84-92.

Gorbatikov A.V., Stepanova M.J., 2008, Statistical characteristics and stationarity properties of low-frequency seismic signals. Izvestiya, *Physics of the Solid Earth,* 1, 50-59. DOI: 10.1007/s11486-008-1007-0.

Gorbatikov A.V., Tsukanov A.A., 2011, Simulation of the Rayleigh waves in the proximity of the scattering velocity inhomogeneities. Exploring the capabilities of the microseismic sounding method. *Izvestiya, Physics of the Earth,* 4, 354-369. DOI: 10.1134/S1069351311030013

Gorbatikov A.V., Larin N.V., Moiseev E.I., Belyashov A.V., 2009, The microseismic sounding method: Application for the study of the buried diatreme structure. *Doklady Earth Sciences,* 1, 1222-1226. DOI: 10.1134/S1028334X0907040X.

Gorbatikov A.V., Montesinos F.G., Arnoso J., Stepanova M.Yu, Benavent M., Tsukanov A.A., 2013, New Features in the Subsurface Structure Model of El Hierro Island (Canaries) from Low-Frequency Microseismic Sounding: An Insight into the 2011 Seismo-Volcanic Crisis. *Surveys in Geophysics,* 34, 463–489. DOI: 10.1007/s10712-013-9240-4.

IAEA-TECDOC-1363. Guidelines for Radioelement Mapping Using Gamma Ray Spectrometry Data, Vienna: 2003.

Kikaja D., Jeranb Z., Bahtijaric M., Stegnara P., 2016, Radon in soil gas in Kosovo. *Journal of Environmental Radioactivity*, 164, 245–252.

Killeen P.G., Mwenifumbo C.J., Ford K.L., 2015, Tools and Techniques: Radiometric Methods. *Treatise on Geophysics (Second Edition)*, 11, 447–524.

King Chi-Yu, 1980, Episodic radon changes in subsurface soil gas along active faults and possible relation to earthquakes*. J. of Geophys. Res.*, 6, 3065–3078.

Kontarovich R.S., Babayants, P.S., 2011, Problems of modern advanced geophysical support for prediction and exploration operations. *Prospect of mineral resources.* 7, 18-22.

Lin F.C., Tsai V.C., Ritzwoller M.H., 2012, The local amplification of surface waves: A new observable to constrain elastic velocities, density, and anelastic attenuation, *J. Geophys. Res*., 117, B06302, doi:10.1029/2012JB009208.

Mwenifumbo C.J., Kjarsgaard B.A., 1999, Gamma-ray logging and radioelement distribution in the Fort à la Corne kimberlite pipe 169. *Exploration and Mining Geology*, 8, 12, 137–147.

Popov D.V., Danilov K.D., Zhostkov R.A., Dudarov Z.I., Ivanova E.V., 2014, Processing the digital microseism recordings using the Data Analysis Kit (DAK) software package. Seismic Instruments, 50, 75-83. DOI: 10.3103/S074792391401006X.

Reed L.E., Witherly K.E., 2007, 50 Years of Kimberlite Geophysics, A Review.

Proceedings of Exploration 07: Fifth Decennial International Conference on Mineral Exploration" edited by B. Milkereit. 679-689.

Rybalchenko A.Ya., Rybalchenko T.M., Silaev V.I., 2011, Theoretical basis for forecasting and exploration of primary diamonds deposits of tuffizit type. *Proceedings of the Komi Science Centre,* 1, 5*,* 54-66.

Stogniy V.V., Korotkov Yu.V., 2010, The Search of the Kimberlite Bodies by Transients. *Malotirazhnaya tipografiya 2D, Novosibirsk*, 121.

Tsyganov V.A., Kontarovich R.S., Mogilevskij V.E., Golubkov V.V., Kercman V.M., 2004, Sovremennye aérogeofizicheskie tehnologii – kak osnova geologicheskikh i prognozno-mineragenicheskikh kart novogo pokoleniya. In *Sbornik nauchnyh trudov «Kongress vypusknikov geologicheskogo fakul'teta MGU 26 maya 2004».* pp. 151-158. MGU, Moskva.

Yakovlev E.Y., Kiselev G.P., Druzhinin S.V., 2016, Non-equilibrium uranium in kimberlites and host rocks Pionerskaya pipe of the M.V. Lomonosov deposit. *Vestnik of Northern (Arctic) Federal University*, 1, 19-28.

Geofísica Internacional (2017) 56-2: 157-172

Original paper

Groundwater vulnerability based on GIS approach: Case study of Zeuss-Koutine aquifer, South-Eastern Tunisia

Hanen Jarray*, Mounira Zammouri, Mohamed Ouessar, Fadoua Hamzaoui-Azaza, Manuela Barbieri, Ammar Zerrim, Albert Soler and Houcine Yahyaoui

Received: April 04, 2016; accepted: January 16, 2017; published on line: April 01, 2017

Resumen

La cartografía de la vulnerabilidad del agua subterránea se utiliza como herramienta de modelado de contaminación y para proteger los recursos hídricos. El acuifero Zeuss-Koutin, que constituye una fuente primordial de agua potable en el sur este de Tunez, esta sometido a una explotación intensiva y amenazado de contaminación debido esencialmente a la zona industrial de Koutine. El agua subterránea circula a través de piedra calcarea fisurada y karstificada. La vulnerabilidad del acuifero se ha evaluado en los acuiferos Zeuss-Koutine utilizando el método SINTACS. Los distintos parámetros del modelo se obtuvieron de distintes fuentes y se hicieron mapas temáticos utilizand ArcGis. A cada parámetro SINTACS se le assigno un peso y una clasificación basados en una amplia gama de información del parámetro. El peso de cada parámetro depende del impacto de la contaminación potencial. El análisis del mapa de vulnerabilidad a la contaminación muestra que la parte sud-este del acuifero y los lechos Wadis son mas susceptibles a la contaminación. Las concentraciones de nitratos medidas en dos campañas de muestreo realizadas en temporades altas y secas en agua son coherentes con los resultados del modelo SINTACS.

Palabras clave: vulnerabilidad de agua subterranea, método SINTACS, SIG, contaminación, acuifero Zeuss-Koutine, sud este de Tunez.

H. Jarray*
Ecole Nationale des Ingénieurs Sfax (ENIS)
Université de Sfax, Route Soukra Km 3.5
1173-3038, Tunisia
*Corresponding author: jarray_hanen@yahoo.fr

M. Zammouri
Faculté des Sciences de Tunis
Université de Tunis El Manar
Campus Universitaire Farhat Hached, 2092
Tunis, Tunisia

H. Jarray
M. Ouessar
A. Zerrim
Laboratoire d'Eremologie et Lutte contre la Désertification
Institut des Régions Arides Médenine (IRA)
4119-Médenine, Tunisia

F. Hamzaoui-Azaza
Unité de recherche Géochimie et Géologie de l'Environnement
Faculté des Sciences de Tunis
Université de Tunis El Manar
Campus Universitaire Farhat Hached, 2092
Tunis, Tunisia

M. Barbieri
A. Soler i Gil
Grup de Mineralogia Aplicada i Geoquímica de Fluids
Departament de Mineralogia, Petrologia i Geologia Aplicada
Facultat de Ciencies de la Terra, Universitat de Barcelona (UB)
C/Martí i Franquès s/n, 08028
Barcelona, Spain

H. Yahyaoui
Commissariat Régional au Développement Agricole (CRDA) de Médenine
4100 Médenine, Tunisia

Abstract

Groundwater vulnerability mapping is largely used as a modeling tool to delineate areas susceptible to pollution and to protect groundwater resources from this threat. The Zeuss-Koutine aquifer, which constitutes an important source of drinking water in the Southeastern Tunisia, is subjected to an intensive exploitation and threatened by pollution due mainly to the industrial zone of Koutine. The groundwater circulates in fissured and karstified limestone. Aquifer vulnerability has been assessed using the SINTACS method. The different parameters of the SINTACS model were collected from several sources and converted into thematic maps using ArcGis. Each SINTACS parameter was assigned a weight and rating based on a range of information within the parameter. The weight of each parameter depends on the impact of potential pollution. The analysis of vulnerability map to pollution shows that the Southeastern part of the aquifer and the Wadis beds are more susceptible to pollution. The measured nitrate concentrations of two sampling campaigns carried out in high and dry water seasons are coherent with the SINTACS model results.

Key words: Groundwater vulnerability; SINTACS method; GIS; pollution; Zeuss-Koutine aquifer, South-East of Tunisia.

Introduction

Groundwater pollution can be avoided by delineating and monitoring vulnerable areas. Determining the spatial extension of areas susceptible to pollution is difficult given the many variables affecting groundwater pollution (Dixon, 2005). In fact, groundwater vulnerability cannot be directly measured in situ. It is a complex function of large number of parameters related to the soil, the unsaturated zone and the aquifer (Aller *et al*., 1987; Civita, 1990).

Margat (1968) introduced the concept of groundwater vulnerability to pollution in the 1960s in France. It can be defined as the possibility of percolation and diffusion of pollutants from surface into the groundwater (Aller *et al*., 1987; Civita, 1990).

Several approaches were developed in the world for aquifer vulnerability assessment. They include statistical approaches, based on variable related to pollutant concentration or to pollution probability (Zwahlen, 2004), indices methods, based on weighting between various criteria affecting the vulnerability (Gogu & Dassargues, 2000) and models taking into account the physical, chemical and biological processes in the unsaturated zone (Schnebelen *et al*., 2002). The indexes methods such as DRASTIC (Aller *et al*., 1987), GOD (Foster 1987), AVI (Van Stempvoort *et al*., 1993), SINTACS (Civita, 1994), DRISTPI (Jiménez-Madrid, 2013), EPIK (Doerfliger & Zwahlen, 1997), PI (Goldscheider *et al*., 2000) and COP were based on the European approach (COST, 2003). They are well-known worldwide of low cost and the most relevant with regard to field realities because of the consideration of the relative importance of every criterion involved in groundwater vulnerability (Ashokraj *et al*., 2015; Al-Abadi *et al*., 2014; Neshat *et al*., 2014; Kumar *et al*., 2013; Sener & Davraz, 2013; Saidi *et al*., 2010, Leyland & Witthüser, 2010). The characterization of groundwater vulnerability is regularly a qualitative process; specified intrinsic vulnerability assessment methods present a subjective component that may affect the results (Jiménez-Madrid, 2011). Dissimilarities between the different results of vulnerability methods are a result of the weight and rating attributed to each parameter (Hiscock *et al*., 1995).

Sustainable management of groundwater resources, the prediction of the pollution risk and the prevention against groundwater pollution are important issues, especially in semiarid and arid regions where precipitation are scarce and irregular (Ouessar *et al*., 2006; Khemmoudj *et al*., 2014). In these regions, groundwater resources are the main source for water supply and their prevention from degradation and pollution is vital. Various pollution types such as heavy metals, fertilizers, pesticides and other organic chemicals threaten groundwater (Babiker *et al*., 2005). The karstified and fissured carbonated aquifers are highly vulnerable to pollution due to human activities (Corniello & Ducci, 2000; Corniello *et al*., 2004; Ducci, 2010).

The aim of this paper is to evaluate Zeuss-Koutine aquifer vulnerability using SINTACS method based on GIS. The hydrogeological parameters were mapped and processed to delineate areas susceptible to pollution producing a vulnerability assessment map. The SINTACS model results are compared to measured nitrate concentration of two sampling campaigns carried out in February and June 2015 and representative of high and low water seasons, respectively.

Description of the study area

The Zeuss-Koutine aquifer is located in the coastal Jeffara plain in South-East of Tunisia. The aquifer covers an area of about 820 km^2 (Figure 1). The geographical location of the study area lies in longitudes 10°16´-10°61´E and latitudes of 33°39´-33°75´N. The climate is arid Mediterranean with an average annual rainfall of 180 mm. The southeastern Tunisia is characterized by the presence of alternating marine and continental formations consequences of marine transgressions and regressions throughout the geological history of the northern Sahara (Gabtni *et al*., 2009). The stratigraphic sequence outcropping in the study area ranges from Triassic to Quaternary (figure 1). The groundwater circulates in the carbonate formations of the Jurassic, the Albo-Aptian, the Turonian and the lower Senonian. However, the Jurassic limestones is the main layer with a thickness reaching 120 m (Hamzaoui-Azaza *et al*., 2011). The Zeuss-Koutine aquifer constitutes a multilayered hydrogeologic entity where the relays are available through faults or by vertical drainance (Gaubi, 1988). The hydraulic communication between different layers of the Zeuss-Koutine aquifer is realized through faults of which the Medenine fault is the most important. Currently, this aquifer is subjected to an intensive exploitation and exploited by several wells. The main recharge of Zeuss-Koutine is infiltration of runoff water flowing from Matmata Mountains and local infiltration from several wadis (streams) (Oum Zessar, Zeuss…). The Zeuss-Koutine aquifer provides a source of water for drinking and agriculture use. Since 1962, Zeuss Koutine aquifer has been contributing significantly to drinking water supply of Jerba Island and major cities of Tataouine and Medenine governorates. The pumping of the aquifer started since the 60s and has kept a gradual increase up to present. For example, exploitation flow rates have increased from 206 l/s in 1977 to 277 l/s in 1987, 298 l/s in 1995, 339 l/s in 2004, 589 l/s in 2010 to 623 l/s in 2014. The withdrawals reached 641 l/s in 2014 while the renewable resources are estimated to 352 l/s (DGRE, 2014). The exploitation increase produced a continuous piezometric decline of 0.5 to 1 m/year on average and a possible groundwater pollution by the salty waters of Sebkha in the northeast of the Zeuss-Koutine basin (Gaubi, 1988). The transmissivity of the aquifer varies between 0.055 and 0.2 m^{2}s^{-1} (OSS, 2005).

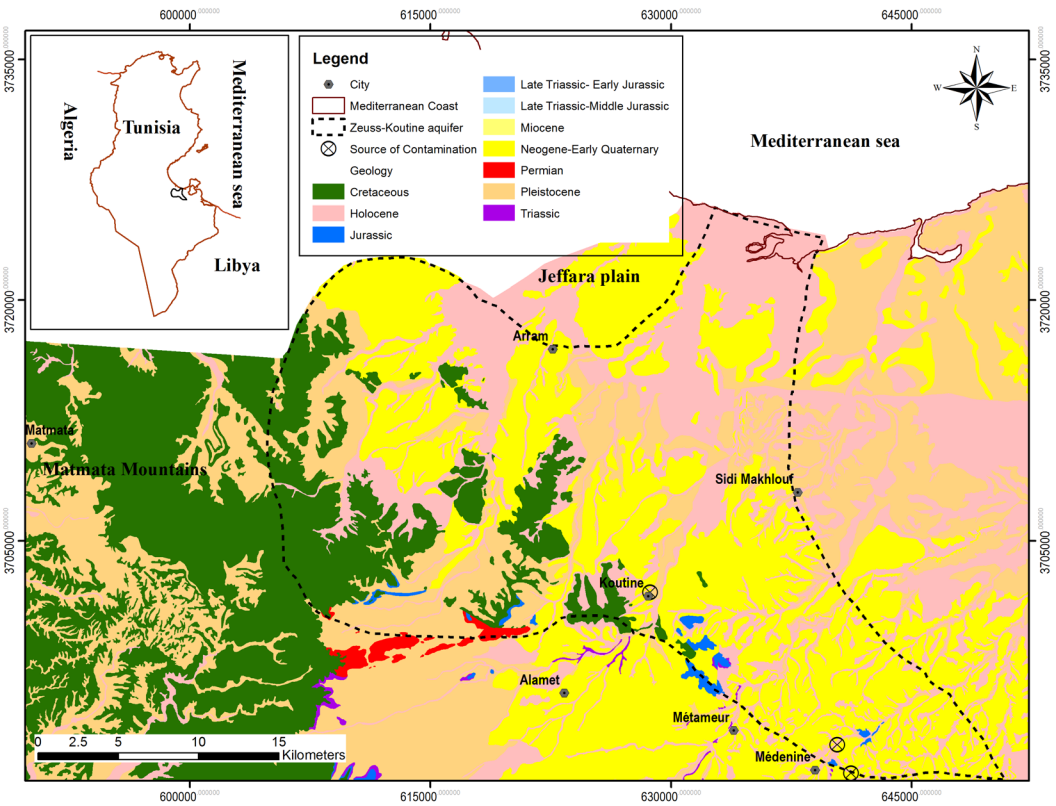

Figure 1. Geologic map of Zeuss-Koutine aquifer (based on Geologic maps: Medenine, Ajim, Mareth, Kirchaou, Matmata and Ghomrassen).

Groundwater flow in the study area is towards the Sebkha Oum Zessar and the Mediterranean Sea (Hamzaoui-Azaza, 2011) (Figure 2). Moreover, groundwater is threatened by pollution. The main source of pollution is the industrial zone of Koutine (milk, soft drinks and juice industries) in the south part of the Zeuss-Koutine aquifer and wastewater effluents in Medenine urban area in the southeastern part of the aquifer. The vulnerability assessment of the Zeuss-Koutine aquifer is a crucial issue in order to prevent groundwater from pollution. We focus on the SINTACS model (Civita, 1990; Civita *et al*., 1999) that has been widely used for any kind of aquifer and especially for karstic and fissured aquifers (Civita *et al*., 1999).

Materials and Methods

The vulnerability assessment approach

SINTACS method is an updated model of US DRASTIC method. It was developed in Italy in the early 1990s in order to adapt the mapping to a larger scale in view of the great diversity of the hydrogeology of Italy (Civita, 1990; Civita, & De Maio, 2004). SINTACS model shows vulnerability index of the study area using seven hydrological parameters, which are the Depth to water *S* (*Soggiacenza* in Italian), Impact of effective infiltration *I* (*Infiltrazione* in Italian), Hydrogeologic properties of the aquifer *N* (*Not Azione del Satoru* in Italian), Attenuation capacity of the soil/sediment cover *T* (*Tipologia della Copertura* in Italian), Attenuation capacity in the unsaturated zone *A* (*Carratteri Idrogeologici dell Acquifero* in Italian), Hydraulic conductivity range of the aquifer *C* (*Conductivity Idraulica* in Italian), and Hydrological role of the terrain slope *S* (*Acclività della Topographica area* in Italian). To avoid confusion with the depth to water table, we will change the terrain slope designation to *SA*. Unlike DRASTIC, SINTACS method allows to use, at the same time and in different cells, weighting factors variable according to certain situations. It is more flexible in terms of the indexation and weighting system. The steps followed in the Zeuss-Koutine aquifer vulnerability assessment were data gathering, processing and mapping data using ArcGis, and operating results for the identification of vulnerable areas.

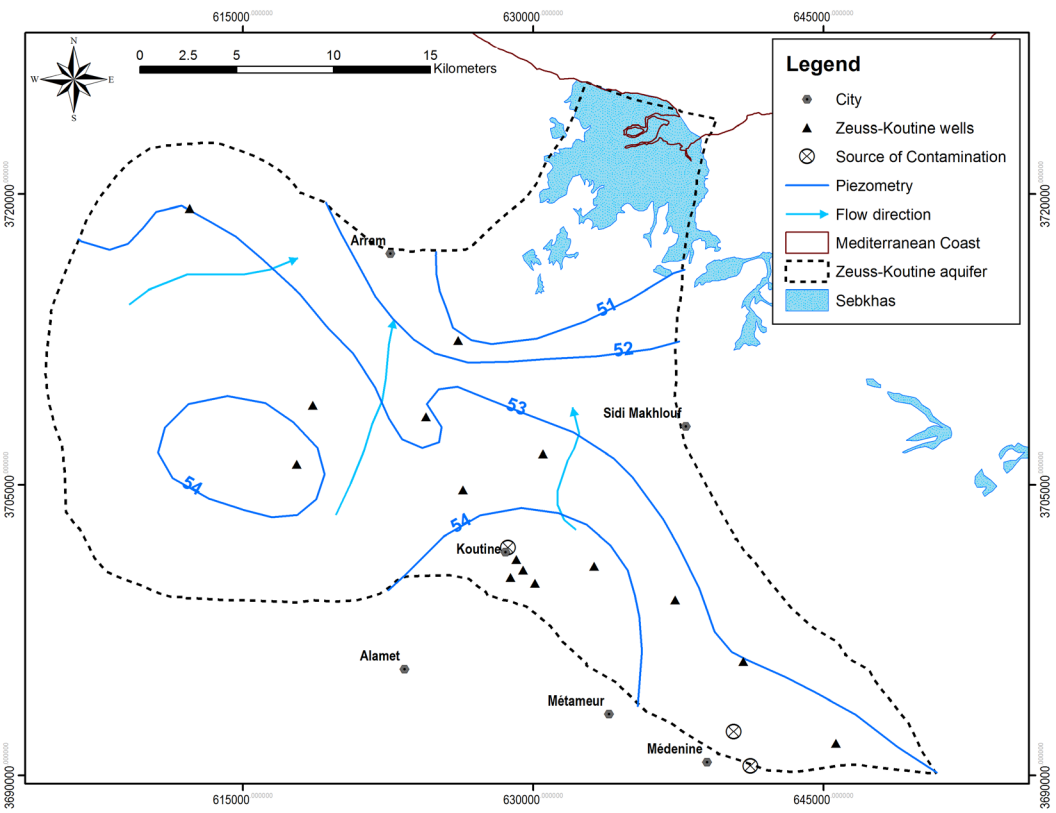

Figure 2. Piezometric map of Zeuss-Koutine aquifer (Hamzaoui-Azaza et al. 2011)

SINTACS vulnerability index (*SI)* is computed using the equation (1) (Civita & De Maio, 1997):

$$SI = S_r \times S_w + I_r \times I_w + N_r \times N_w + T_r \times T_w + A_r \times A_w + C_r \times C_w + SA_r \times SA_w \quad (1)$$

Where the weighted parameters are: S_w, I_w, N_w, T_w, A_w, C_w and SA_w (Table 1). S_r, I_r, N_r, T_r, A_r, C_r and SA_r are ratings for each of the parameters. The weight of each parameter depends on the impact of potential pollution (Table 1). The SINTACS parameters ratings vary from 1 to 10, where higher values are directly proportional to the degree of vulnerability.

Table 1. The SINTACS model parameter weight's (Civita & De Maio, 2004).

Factor	Weight
Depth to water (S)	3
Impact of effective infiltration (I)	3
Attenuation capacity in the unsaturated zone (N)	3
Attenuation capacity of the soil/sediment cover (T)	4
Hydrogeologic properties of the aquifer (A)	4
Hydraulic conductivity range of the aquifer (C)	5
Hydrological role of the terrain slope (SA)	4

Table 2. Vulnerability classes of SINTACS method

Vulnerability index (SI)	Degree of intrinsic vulnerability
26–80	Very low
81–105	Low
106–140	Medium
141–186	High
187–210	Very high
211–260	Extremely high

The intrinsic vulnerability values indicate the potential pollution in the aquifer. A higher vulnerability index indicates a higher probability of pollution (Civita & De Maio, 1997). The output values vary from 26 to 226. The vulnerability classes are defined using Table 2 (Corniello *et al*., 2004):

To establish thematic layers of the seven parameters, several types of data were used. Table 3 shows data types, sources and usages.

The depth to water (*S*) is the vertical distance from the ground surface to the water table. Generally, potential aquifer protection increases with the higher depth of the water. The water table depths were measured from observation wells. The Inverse Distance Weight (IDW) interpolation method implemented in the ArcGIS Geostatistical Analyst extension was applied to interpolate the points and to develop the raster map with a pixel size of 100 m. The IDW technique provided better fitting data for use in this study since it produced only the value ranges found within the data attributes.

Table 3. Sources of data used for creation of hydrogeological parameter for SINTACS method

Data type	Source	Format	Scale	Used to produce
Borehole, Piezometer data, water table level	CRDA[1], DRE[2]	Table, Location map	1:100 000	*S*, *A*
Inter annual rainfall (mean)	CRDA, DRE	Table	1:100 000	*I*
Geology map	Geologic maps	Digital	1:100 000	*A*
Soil map	Agriculture map, 2003	Digital	1:100 000	*T*
Topographic map	DEM3 30 Tunisie		1:100 000	*SA*
Hydraulic conductivity, piezometer geological profiles	CRDA, DRE			*N*, *A*, *C*

[1]CRDA: Commissariat Régional au Développement Agricole
[2] DRE: Direction de ressources en eau (Tunisie)
[3] DEM: Digital elevation model

The main source of groundwater recharge is rainfall infiltration. Net recharge (*I*) is the quantity of water per unit of land that reaches the aquifer (Aller *et al*., 1987). Rainfall data were collected from CRDA-DRE Medenine rain gauges and interpolated using IDW method; to produce the isohyet map. Since, the Zeuss-Koutine aquifer is unconfined; rating of net recharge is derived from the amount of precipitation.

An aquifer is a geological formation containing water, which can be exploited through wells or sources for domestic, industrial and agricultural usage. Circulation and spread of any pollutant into the saturated zone depends on the texture and lithology of the aquifer layers. This is always controlled by the particle size, porosity, permeability and lithology of geological formations. The parameter *A* was obtained by IDW interpolation of horizontal equivalent permeability of the saturated zone. Horizontal equivalent permeability was calculated using the equation (2):

$$A_{eq} = \frac{\Sigma_{i=1}^{3} H_i \times A_i}{\Sigma_{i=1}^{3} = 1\ H_i} \qquad (2)$$

Where: A_{eq} is horizontal equivalent permeability (m/s), H_i is thickness of the layer *i* (m), A_i is permeability of the layer *i* (m/s), *i* (*i*=1 to 3) is an index related to the lithological classes forming the Zeuss-koutine aquifer.

The soil parameter (*T*) represents the influence of soil material on the infiltration. The soil layer types indicate the recharge rate infiltrated into the aquifer. In general, the less clay and the smaller the grain size of the soil, the less permeable the soil will be and the less pollutant will reach the aquifer (Aller *et al*., 1987). Taamallah (2003) provided the soil map of the study area. Table 4 shows the classification of soil types and their rating.

Table 4. The type of the soil media and their ratings.

Soil class	Rating
Regosols	9
Lithosols, Fluvisols	5
Rendzinas (Gypsum)	3
Xerosols	8
Solonchak	2
Gleysols	3
Rendzinas (Calcareous)	4
Urban areas	1

Topography (*SA*) refers to the slope of the land surface. The topography indicates whether a pollutant will move or will stay on the ground surface to penetrate into the aquifer (Lynchez *et al*., 1994). The slope (%) of the study area was obtained from the Digital Elevation Model (DEM).

The vadose zone (*N*) is defined as the fraction between groundwater and the surface of soil where the pores are partially saturated with water. The permeability of the vadose zone controls the movement of pollutants and their arrival to the aquifer. Most of the physicochemical processes taking place in this zone are influenced by its thickness. The infiltration and dispersion of pollutants are guided by the lithological characteristics of the layers that control their paths and trajectory in the subsurface.

Hydraulic conductivity (*C*) refers to the ability of the aquifer to transmit water. It controls the migration and dispersion of pollutants. Hydraulic conductivity was obtained by identifying the permeability coefficient for each lithological class (Castany, 1982) and assigning a rating to each interval (Aller *et al*., 1987). The conductivity and the aquifer vulnerability are proportional. This factor was obtained by IDW interpolation of point data.

The final SINTACS map was created by calculating a weighted sum of the individual aquifer attribute raster's within Conceptual model ArcGis.

The nitrate sampling campaigns

Groundwater was sampled from 17 wells of Zeuss-Koutine aquifer for nitrate analysis during February (Humid period) and June (Dry period) 2015. The samples were well spatially distributed. A volume of 5 ml of each sample was filtered at 0.2 µm and was conserved in 10 ml plastic tubes. All samples were stored in ice chests at 4°C and transported to the laboratory where they were analyzed within two weeks. The analyses were performed in the Laboratory of the Department of Crystallography, Mineralogy and Mineral Deposits of the University of Barcelona, Spain. Nitrates concentrations were determined using High Performance Liquid Chromatography (HPLC).

Results and discussion

SINTACS parameters

Figure 3 shows the different thematic maps of SINTACS model realized using ArcGis. The ratings corresponding to each class for the parameters are presented in Table 5.

Figure 3a shows that the Zeuss-Koutine aquifer is divided into two water depth intervals (from 23 to 31 m and >31 m). The lowest water table values have the highest index ($S_r \times S_w = 6$) and located near the discharge area of Sebkhat Oum Zessar.

Impact of effective infiltration (I) map (Figure 3b) indicates that the amount of rainfall received by the aquifer is divided into two intervals from 0.1 to 0.17 m/year and from 0.17 to 0.25 m/year, respectively. The major area of the aquifer belongs to the second interval with an index ($I_r \times I_w = 32$).

The parameter A map (Figure 3c), corresponding to hydrogeological properties of the aquifer, shows the distribution of the horizontal equivalent permeability of the saturated zone. The highest permeability is represented by dark red and reaches 8.7×10^{-4} m/s with $Ar \times Aw = 32$. In fact, the aquifer layers consisting of limestone that has been affected by dissolution producing ridges, fissures, karsts and sinkholes show high permeability values. The lower permeability is about 10^{-5} m/s, this permeability decrease is explained by the existence of marl and clay layers (Gaubi 1988; Yahyaoui 1998).

Figure 3d shows the soil type distribution. Each soil type has a rating. Regosols have the highest index ($Tr \times Tw = 36$) while the urban areas have the lowest index ($Tr \times Tw = 4$).

Topography of the aquifer (SA) map (Figure 3*e*) shows that the majority of the Zeuss-Koutine aquifer area has a slope between 0 and 18 %.

The vadose zone (N) map indicates that the wadi beds have the highest permeability value, about 10^{-3} m/s. In fact, wadi beds are formed by gravels, pebbles and sands resulting in high permeability (Figure 3*f*).

The hydraulic conductivity (C) map shows that the highest values are located in Matmata mountains and in the southeastern part of the aquifer (Figure 3*g*). This is explained by the existence of fissured and karstified limestones. The hydraulic conductivity of the aquifer reachs 4.45×10^{-3} m/s.

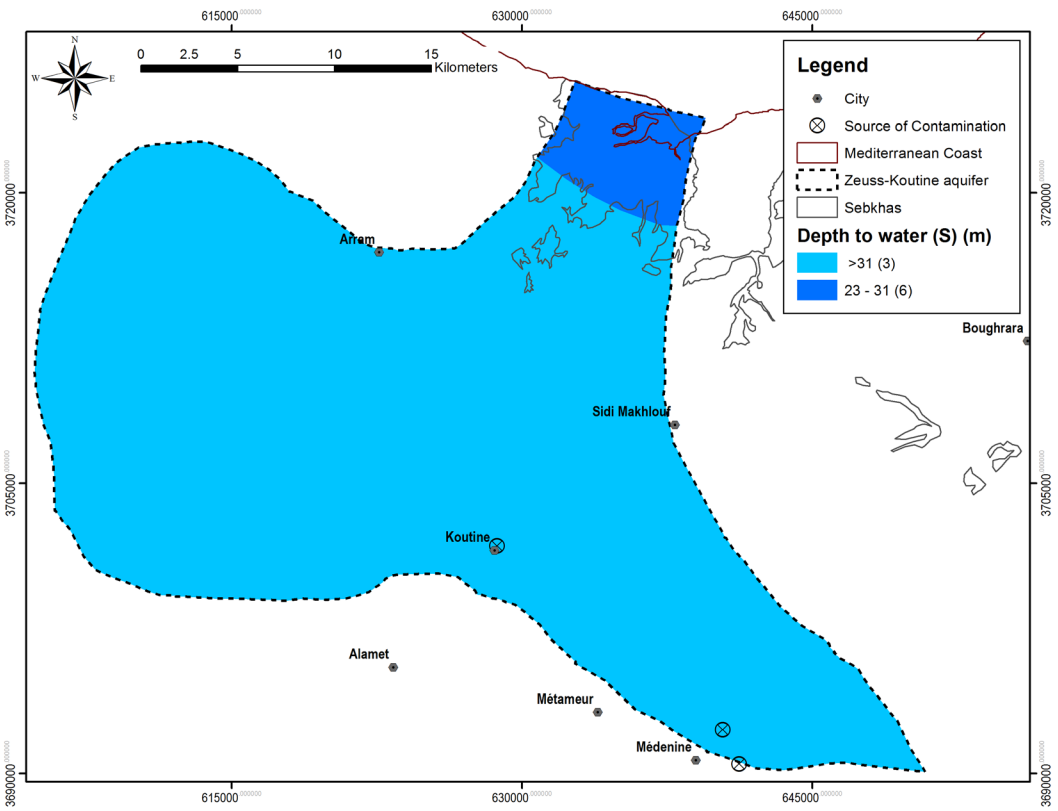

Figure 3. The calculated layers of SINTACS model showing the calculated weight of the different parameters. *(a)* Depth to water (S), *(b)* Impact of effective infiltration (I), *(c)* Hydrogeologic properties of the aquifer (A), *(d)* Attenuation capacity of the soil/sediment cover (T), *(e)* Hydrological role of the terrain slope (SA), *(f)* Attenuation capacity in the unsaturated zone (N), *(g)* Hydraulic conductivity range of the aquifer (C).

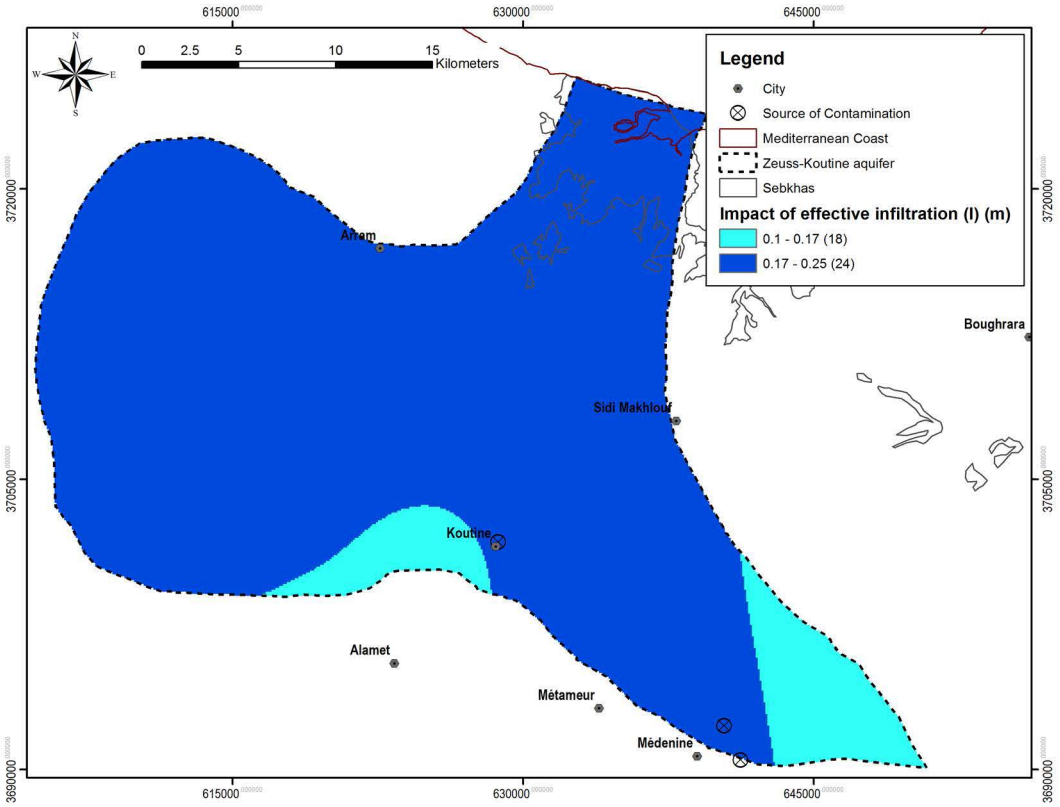

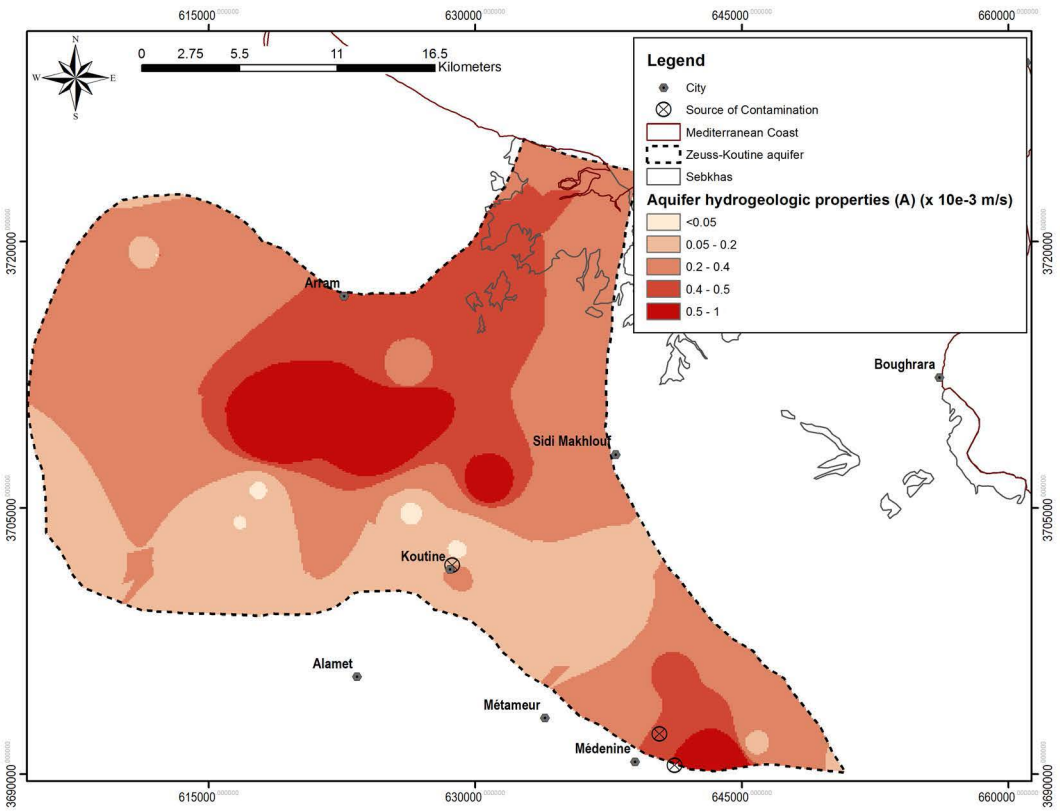

Figure 3b and 3c.

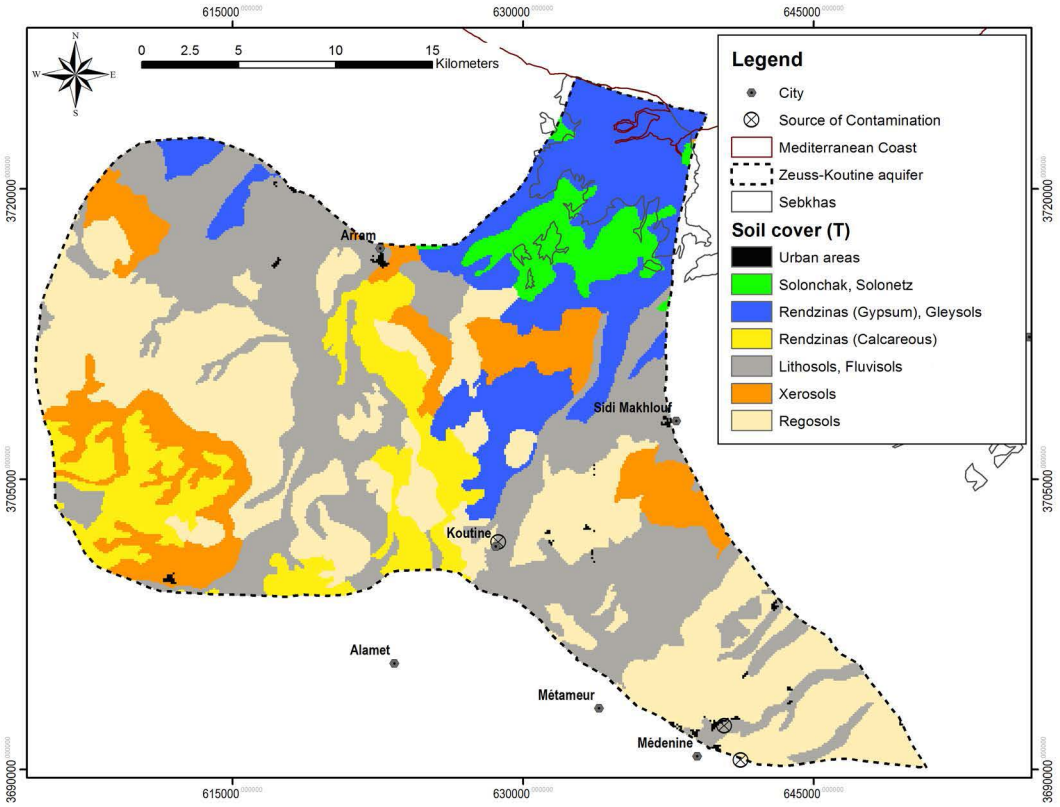

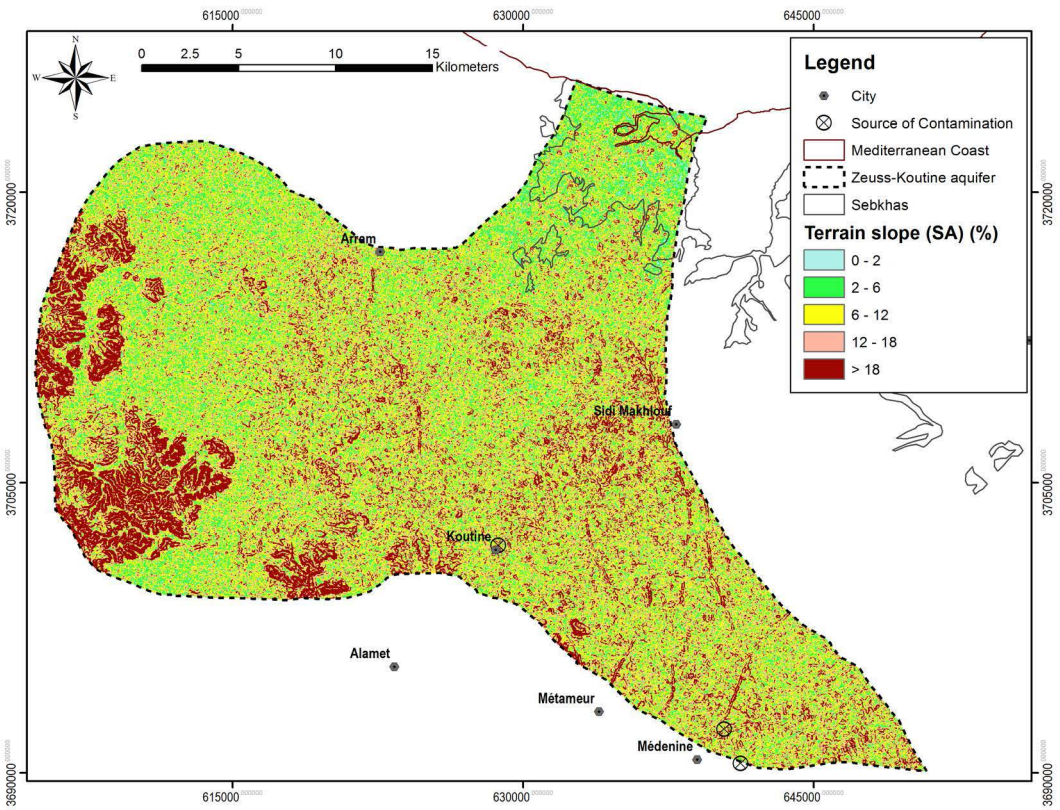

Figure 3d and 3e.

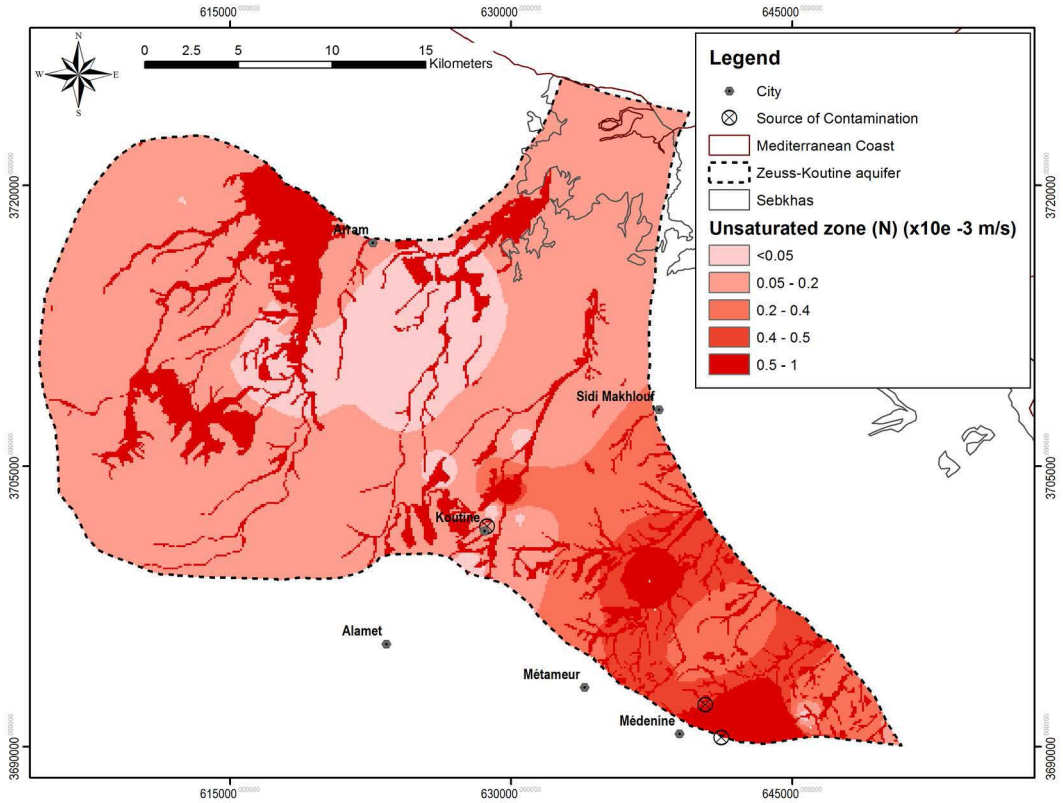

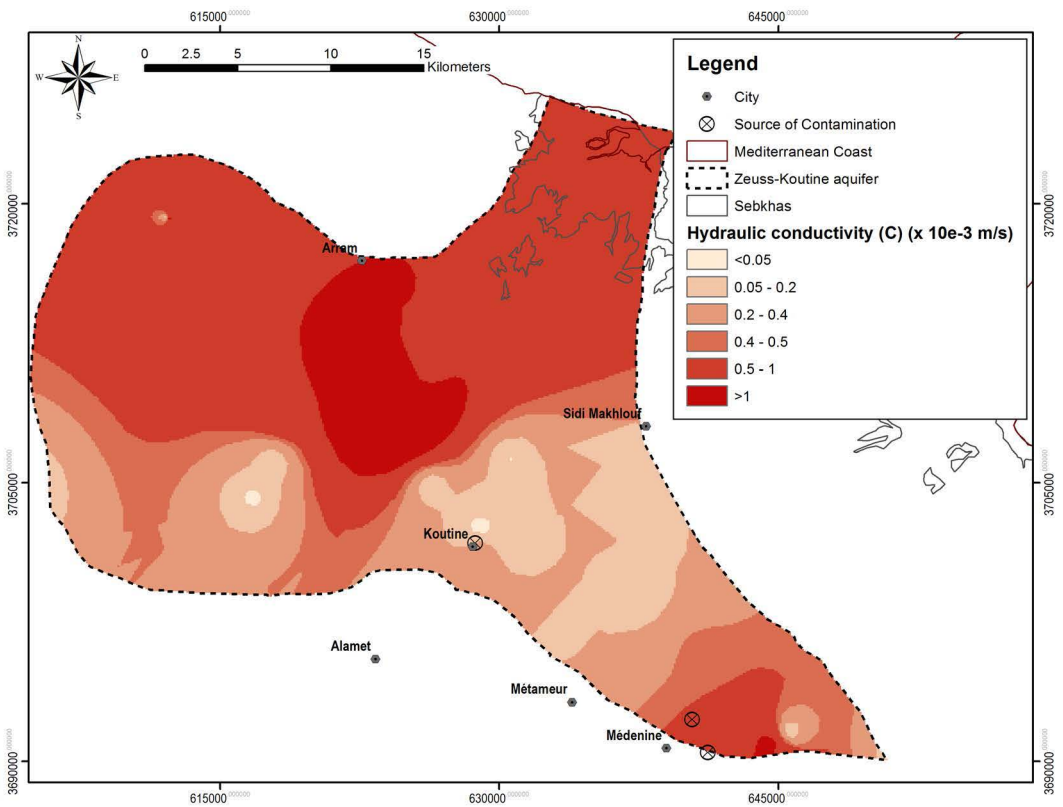

Figure 3f and 3g.

Table 5. Rating values of the vulnerability parameters for the SINTACS method.

S (Depth to water)								
Range (m)	0 - 1.5	1.5 - 4.5	4.5 - 9	9 - 15	15 - 23	23 - 31	> 31	
Rating	10	9	7	5	3	2	1	
I (Impact of effective infiltration)								
Range (m)	0 - 0.05	0.05 - 0.1	0.1 - 0.17	0.17 - 0.25	> 0.25			
Rating	1	3	6	8	9			
N (Attenuation capacity in the unsaturated zone)								
Range (10^{-3}m/s)	<0.05	0.05 - 0.2	0.2 - 0.4	0.4 - 0.5	0.5 - 1	>1		
Rating	1	2	4	6	8	10		
T (Soil parameter)								
Range	Regosols	Lithosols, Fluvisols	Rendzinas (Gypsum)	Xerosols	Solonchak, Solonetz	Gleysols	Rendzinas (Calcareous)	Urban areas
Rating	9	5	3	8	2	3	4	1
A (Hydrogeologic properties of the aquifer)								
Range (10^{-3}m/s)	<0.05	0.05 - 0.2	0.2 - 0.4	0.4 - 0.5	0.5 - 1	>1		
Rating	1	2	4	6	8	10		
C (Hydraulic conductivity)								
Range (10^{-3}m/s)	<0.05	0.05 - 0.2	0.2 - 0.4	0.4 - 0.5	0.5 - 1	>1		
Rating	1	2	4	6	8	10		
SA (Hydrological role of the terrain slope)								
Range (%)	0 - 2	2 - 6	6 - 12	12 - 18	> 18			
Rating	10	9	5	3	1			

SINTACS vulnerability map

Figure 4 shows the spatial distribution of vulnerability classes of the Zeuss-Koutine aquifer. SINTACS map shows that 0.1 % of the total area of the study area has an extremely high vulnerability index, 8.4 % a very high vulnerability, 46.1 % a high vulnerability, 34.8 % a moderate vulnerability, 10.5 % a low vulnerability and 0.1 % a very low vulnerability. The highest vulnerability is located mainly in wadis beds, the southeastern part of the aquifer and the area of Matmata Mountains. In the wadis and Matamta Mountains, the high values are explained by the low depth of the water table and the high permeability of lithological formations consisted in current alluvial wadis deposits (gravels, pebbles…) corresponding to Mio-Plio-Quaternary filling. It is important to note that the recharge area of the Zeuss-Koutine aquifer comprising wadi beds and Matmata Mountains has the highest index of vulnerability (46 % of the total area). In addition, the southeastern part of the aquifer has a high vulnerability index (8.6 % of the total area). This is can be explained by the low depth of water table and the high permeability of the saturated and vadose zone in wadi beds that let water to infiltrate easily. In addition, the low slope allows runoff to stagnate and to infiltrate immediately.

Vulnerability map validation

Nitrate concentration ranges from 0.01 to 34.2 mg/l for the high water season campaign (February, 2015) while it varies between 1 and 61.02 mg/l for the low water season campaign (June, 2015) (Table 6). Results of the two campaigns show an increase of nitrate concentrations from the high water season to the low water season. Nitrate spatial distribution map for the Zeuss-Koutine aquifer (Figures 5a and 5b) indicates that the highest values are located in the southeast of the aquifer near Medenine urban area, in the close vicinity of the Koutine region where industrial factories are implemented and in the extreme West of the aquifer. The nitrate distribution map confirms the vulnerability map results. In fact, urban area and Matmata Mountains region have the highest nitrate values (>20 mg/l).

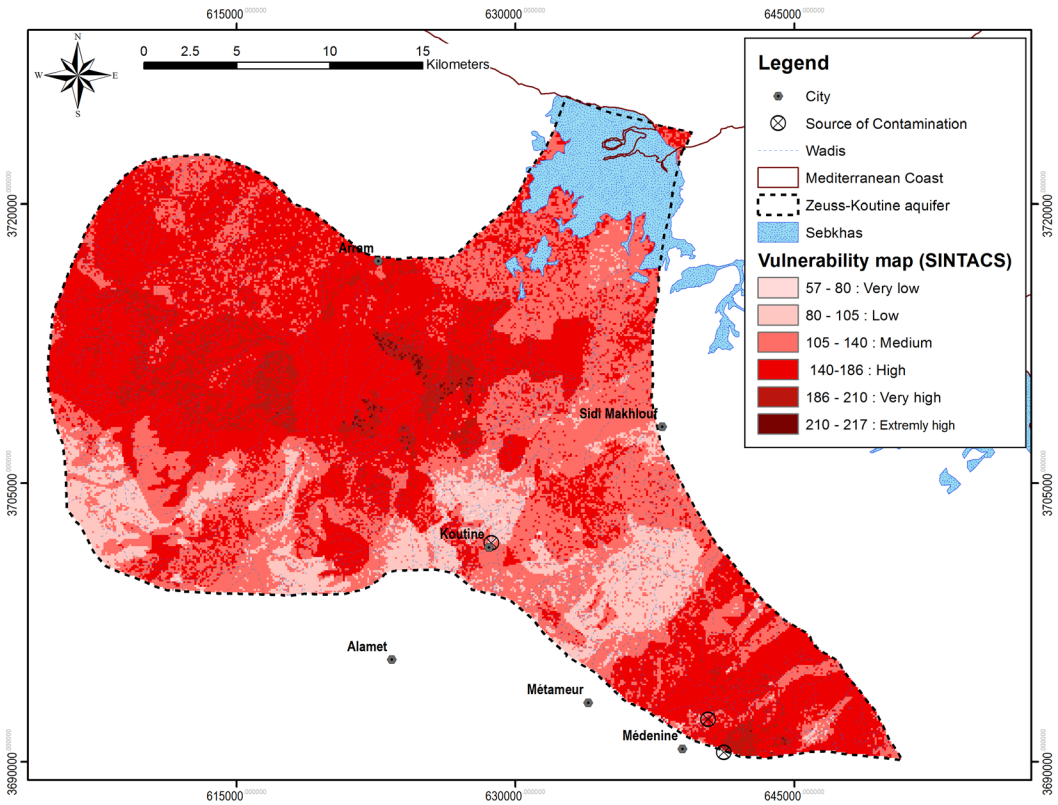

Figure 4. Vulnerability map of Zeuss-Koutine aquifer (SINTACS).

Table 6. Nitrate concentration results of sampled water points.

Sampled points	X (UTM)	Y (UTM)	February 2015 campaign Nitrate (mg/l)	June 2015 campaign
ZK-1	640865	3695888	25.28	24.36
ZK-2	645647	3691676	20.67	18.11
ZK-3	612259	3719252	23.73	23.52
ZK-4	617362	3704685	13.31	**
ZK-5	618628	3709107	15.27	15.02
ZK-6	629480	3700610	34.20	45.52
ZK-7	633148	3700799	28.11	25.31
ZK-8	630095	3699929	0.01	1.00
ZK-9	626379	3704741	3.11	2.67
ZK-10	630513	3706604	6.65	7.60
ZK-11	629139	3701159	33.88	42.63
ZK-12	628102	3702038	26.77	**
ZK-13	626131	3712454	6.65	7.07
ZK-14	624465	3708517	7.21	7.96
ZK-15	637347	3699068	24.24	25.55
ZK-16	628834	3700218	16.50	17.92
ZK-17	617787	3706070	9.33	61.02

** Not analyzed

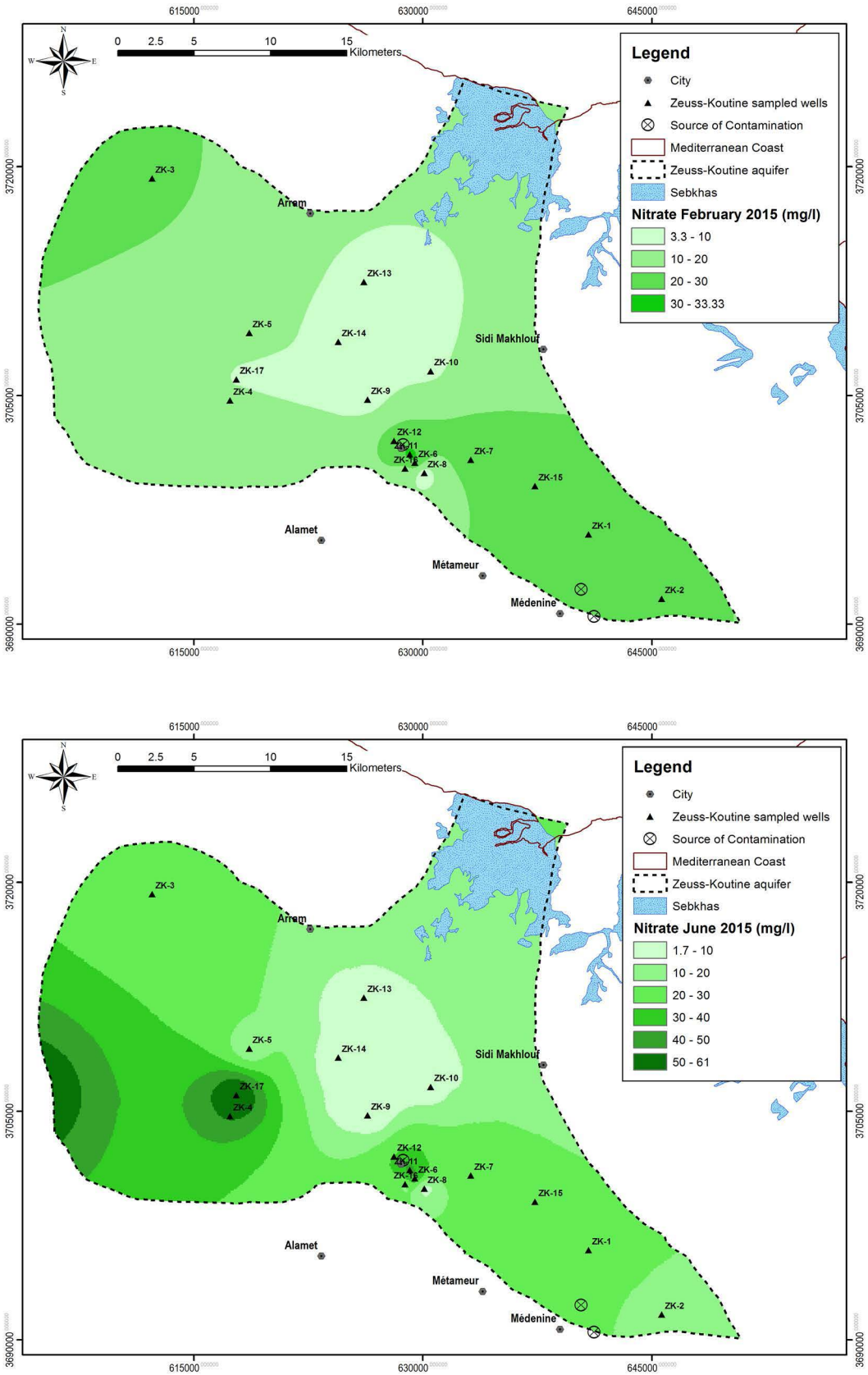

Figure 5. Nitrate concentration distribution in Zeuss-Koutine aquifer in *(a)* February 2015 and *(b)* June 2015.

Summary and conclusion

This study aims to assess groundwater vulnerability in an arid region using the empirical indexes SINTACS models. Seven environmental parameters, prepared in a GIS environment, were used to represent the natural hydrogeological setting of Zeuss-Koutine aquifer. The vulnerability map indicated that wadi beds, urban area and the region of Matmata are more susceptible to pollution where nitrate concentrations are higher than 20 mg/l.

Nowadays, sources of contamination are limited to the southeastern part. They may multiply and spread with the population growth and the economic development of the region, threatening the Zeuss-Koutine waters. In order to relieve the Zeuss-Koutine waters pollution, recommendations may be taken into account. Various sources of waste that can affect groundwater such as solid waste discharges, wastewater treatment plant, industrial areas, etc. should be reduced. A channel discharging plastic pipes with sizes and diameters suitable for the delivery of wastewater treatment plant and industry wastewaters to the sea should be planned.

In order to better exploit the vulnerability map, more detailed information on local conditions and additional hydrologic studies about the studied area are necessary for planners and decision makers to understand the mechanisms of pollution and recharge of the aquifer. Furthermore, in the indexes methods, the concept of groundwater vulnerability deals only with hydrogeological setting and does not include pollutant concentration. This work will be completed by the development of transport model that would enable us to follow the pollutant propagation. This model could be used to investigate some remediation solution like pumping the polluted water by wells located close the pollution source.

Acknowledgements

This work was supported by the Institut des Régions Arides (IRA) through the following programs: Eremology and Combating Desertification Laboratory funded by the Tunisian Ministry of Higher Education and Scientific Research, the EU-funded projects WADIS-MAR (n° ENPI/2011/280-008) and WAHARA (FP7/2007-2013, n° 265570).

References

Al-Abadi A.M, Al-Shamma'a A.M., Aljabbari M.H., 2014, A GIS-based DRASTIC model for assessing intrinsic groundwater vulnerability in northeastern Missan governorate, southern Iraq. *Appl Water Sci*., DOI 10.1007/s13201-014-0221-7.

Aller L., Bennet T., Leher J.H., 1987, DRASTIC: A Standardized System For Evaluating Ground Water Pollution Potential Using Hydrogeological Settings. EPA 600/2-87-035.

Ashokraj C., Kirubakaran M., Colins Johnny J., 2015, Estimation of Groundwater Vulnerability using Remote Sensing and GIS Techniques. IJIRST. 1, 9: 2349-6010.

Babiker I.S., Mohamed A.A., Hiyama T., 2005, A GIS based DRASTIC model for assessing aquifer vulnerability in Kakamigahara Heights, Gifu Prefecture, central Japan. *Sci of the Total Environ*. 345: 127– 140.

Castany G., 1982, Principe et méthodes de l'hydrogéologie.]. Paris: University of Pierre Marie Crue (ParisVI).

Civita M., De Maio M., 1997, SINTACS: un sistema parametrico pernla valutazione e la cartografia della vulnerabilita ´degli acquiferi all'inquinamento. Metodologia et Automatizzazione. Pitagora Ed., Bologna: Itlaia, 191 pp.

Civita M., De Maio M., 2004, Assessing and mapping groundwater vulnerability to contamination - The Italian "combined" approach. *Geofisica international*, 43, 4-19.

Civita M., 1990, Legenda unificata per le carte della vulnerabilita dei corpi idrici soutterranei. In: Studi sulla vulnerabilita degli Acquiferi. Pitagora: Bologna.

Civita M., 1994, Contamination Vulnerability Mapping of the Aquifer: Theory and Practice. Quaderni di Tecniche di Protezione Ambientale, Pitagora.

Corniello A., Ducci D., Monti G.M., 2004, Aquifer pollution vulnerability in the Sorrento peninsula,southern Italy, evaluated by SINTACS method. *Geofísica Internacional*, 43, 4, pp. 575-581.

Corniello A., Ducci D., 2000, "Pollution Vulnerability Assessment in Karstic Aquifers: A Case Study of the Matese Mountains," In: O. Sililo *et al*., Ed., 30th International Association of r:Past Achievements and Future Challenges Cape Town, Balkema, Rotterdam, 26 November-1 December 2000, pp. 725-730.

COST (European cooperation in science and technology), 2003, Action 620 – Vulnerability and risk mapping for the protection of carbonate (karst) aquifers. European Commission, Directorate-General for Research, Report EUR 20912, Luxemburg.

DGRE (Direction Générale des Ressources en Eau, Ministère de l'Agriculture), 2014, Rapport annuel d'exploitation des nappes profondes. DGRE, Tunis, 363 pp.

Dixon B., 2005, Applicability of neurofuzzy techniques in predicting groundwater vulnerability: a GIS-based sensitivity analysis. *J of Hydrol*., 309: 17-38.

Doerfliger N., Jeannin P.Y., Zwahlen F., 1999, Water vulnerability assessment in karst environments: a new method of defining protection areas using a multi-attribute approach and GIS tools (EPIK method). *Environ Geol*., 39, 2: 165–176.

Doerfliger N., Zwahlen F., 1997, EPIK: a new method for outlining of protection areas in karstic environment, in: International symposium and field seminar on "karst waters and environmental impacts", edited by: Gunay, G. and Jonshon, A. I., Antalya, Turkey, Balkema, Rotterdam. 117–123.

Ducci D., 2010, Aquifer Vulnerability Assessment Methods: The Non-Independence of Parameters Problem. J. Water Resource and Protection, 2, 298-308 doi:10.4236/jwarp.2010.24034.

Foster S., 1987, Fundamental Concept in Aquifer Vulnerability, Pollution Risk and Protection Strategy. In: W. Van Dui- jvenbooden and H. G. Van Waegeningh, Eds., Vulnerability of Soil and Groundwater to Pollutions. Committee on Hydrogeological Research, Hague, 69-86.

Gabtni H., Jallouli K., Mickuse L., 2009, Deep structure and crustal configration of the Jeffara basin (Southern Tunisia) based on regional gravity, seismic reflection and borehole data: How to explain a gravity maximum within a large sedimentary basin? *J of Geodynamics*. 4: 142-152.

Gaubi E., 1988, Evolution de la piézométrie et de la géochimie de la nappe de Zeuss-Koutine. Tunis: Faculty of Science of Tunis, 63 pp.

Gogu R.C., Dassargues A., 2000, Current trends and future challenges in groundwater vulnerability assessment using overlay and index methods. *Environ Geol*., 39: 549–559.

Goldscheider N., Klute M., Sturm S., 2000, The PI method – a GIS-based approach to mapping groundwater vulnerability with special consideration of karst aquifers. Zeitschrift für Angewandte Geologie. 46, 3: 157–166.

Hamzaoui-Azaza F., Ketata M., Bouhlila, R., 2011, Hydrogeochemical characteristics and evaluation of drinking water quality in Zeuss-Koutine aquifer, south-eastern Tunisia: *Environ Monit and Assess*. 174: 283–298.

Hamzaoui-Azaza F., 2011, Géochimie et Modélisation des Nappes de Zeuss-Koutine, des Grès du Trias et du Miocène de Jorf Jerba-Zarzis. Department of Geology, University of Tunis El-Manar, Faculty of Science of Tunis, 262 pp.

Hiscock K.M., Lovett A.A., Brainard J.S., Parfitt J.P., 1995, Groundwater vulnerability assessment: two case studies using GIS methodology. *Q J of Eng Geol*., 28: 179–194.

Jiménez-Madrid A., Carrasco F., Martínez C., Gogu R.C., 2013, DRISTPI, a new groundwater vulnerability mapping method for use in karstic and non-karstic aquifers. *Q J of Eng Geol and Hydrogeol*., 46:245-255.

Jiménez-Madrid A., Carrasco F., Martínez C., Vernoux J.F., 2011, Comparative analysis of intrinsic groundwater vulnerability assessment methods for carbonate aquifers. Q J of Eng Geol and Hydrogeol. 44:361-371.

Khemmoudj K., Bendadouche H., Merabet S., 2014, Assessment of the vulnerability of an aquifer by DRASTIC and SINTACS methods: Aquifer of Bazer – Geult Zerga area (northeast Algeria). E3 Journal of Environmental Research and Management 5: 9. pp. 0169-0179.

Kumar S., Thirumalaivasan D., Radhakrishnan N., Mathew S., 2013, Groundwater vulnerability assessment using SINTACS model, Geomat, *Nat Hazards and Risk*, 4, 4: 339-354.

Leyland R.C., Witthuser K.T., 2010, VUKA: a modified COP vulnerability mapping method

for karst terrains in South Africa. *Q J of Eng Geol and Hydrogeol*., 43: 107–116.

Lynchez S.D., Reynders A.G., Schulze R.E., 1994, Preparing input data for a national-scale groundwater vulnerability map of southern Africa. Document ESRI94. Strasbourg: ESRI.

Margat J., 1968. "Groundwater Vulnerability to Contamination," Bases de la Cartographie. Doc. 68 SGC 198 HYD, BRGM, Orleans.

Neshat A., Pradhan B., Dadras M., 2014, Groundwater vulnerability assessment using an improved DRASTIC method in GIS. Resour, *Conserv and Recycl*., 86: 74–86.

OSS (Observatoire du Sahara et du Sahel), 2005, Etude hydrogéologique du système aquifère de la Djeffara tuniso-libyenne. Observatoire du Sahara et du Sahel, Tunisia, 209 pp.

Ouessar M., Taamallah H., Ouled Belgacem A., 2006, Un environnement soumis à des fortes contraintes climatiques. In: Genin D., Guillaume H., Ouessar M., Ouled Belgacem A., Romagny B., Sghaier M., Taamallah H. (eds). Entre la désertification et le développement: la Jeffara tunisienne. CERES, 2006, Tunis, pp: 23-32.

Saidi S., Bouri S., Ben Dhia H., 2010, Groundwater vulnerability and risk mapping of the Hajeb-jelma aquifer (Central Tunisia) using a GIS-based DRASTIC model. *Environ Earth Sci*. 59: 1579–1588.

Schnebelen N., Platel J.P., Le Nindre Y., 2002, Gestion des eaux souterraines en Aquitaine Année 5. Opération sectorielle. Protection de nappe de l'Oligocène en région bordelaise. (ERIC Document Reproduction Service No ED 98-01) 51178).

Sener E., Davraz A., 2013, Assessment of groundwater vulnerability based on a modified DRASTIC model, GIS and an analytic hierarchy process (AHP) method: the case of Egirdir Lake basin (Isparta, Turkey). *Hydrogeol J*., 21: 701–714.

Taamallah H., 2003, Carte pédologique de la Jeffara. Rapport interne. [Soil Map of the Jeffara. Internal report]. Jeffara project, IRA/IRD, Tunis.

Van Stempvoort D., Ewert Wassenaar L.L., 1993, "Aquifer Vulnerability Index (AVI): A GIS Compatible Method for Groundwater Vulnerability Mapping". *Canadian Water Resour J*., 18, 1: 25-37.

Yahyaoui H., 1998, Fluctuations piézométriques des principales nappes dans le gouvernorat de Medénine. DGRE-Tunis, 30pp.

Zwahlen F., 2004, (ed.): Vulnerability and risk mapping for the protection of carbonate (karst) aquifers. European Commission, Directorate – General for Research, European research area: structural aspects – COST 620, 279 pp.

Geofísica Internacional (2017) 56-2: 173-186

Original paper

Guadalajara, Mexico, Earthquake Sequence of December 2015 and May 2016: Source, *Q*, and Ground Motions

Shri Krishna Singh*, Danny Arroyo, Xyoli Pérez-Campos, Arturo Iglesias, Víctor Hugo Espíndola and Leonardo Ramírez with contributions by Citlalli Pérez and Héctor Sandoval

Received: August 12, 2016; accepted: February 28, 2017; published on line: April 01, 2017

Resumen

Se analizó una secuencia de sismos que se produjo a 24 km NNW de la catedral de Guadalajara. La actividad inició el 15 de diciembre de 2015, con un sismo de M_w4.1 y se reanudó el 11 de mayo de 2016, cuando ocurrió el sismo más grande de la secuencia, M_w4.8. Los sismos fueron registrados por dos acelerógrafos en la ciudad y por estaciones de banda ancha a distancias mayores. La región de la fuente de la secuencia se encuentra en el norte de la amplia unión formada por los *rifts* Tepic-Zacoalco, con una orientación NW-SE, el de Colima, con una tendencia N-S, y el de Chapala, con tendencia E-W. El mecanismo focal del evento más grande se caracteriza por: rumbo φ = 21º, echado δ = 49º, y deslizamiento λ = -86º, con el eje de tensión horizontal en una dirección 110º. Este mecanismo no es consistente con la dirección NE-SW de movimiento medido en un echado de falla por Barrier *et al*. (1990) ~ 35 km al WNW de Guadalajara. También se diferencia del mecanismo reportado en un estudio previo para una secuencia sísmica en el *rift* de Zacoalco unos 60 km al sur de Guadalajara. La similitud de las formas de onda en las estaciones acelerográficas sugiere que el mecanismo de otros eventos en la secuencia fueron similares y los eventos se localizan en un volumen pequeño, probablemente en un radio de 1 a 2 km. A partir del análisis de registros del sismo del 11 de mayo a lo largo de la Faja Volcánica Trans Mexicana, desde el volcán Ceboruco, hacia el oeste, y hasta el volcán Popocatépetl, al este, se estimó el parámetro de atenuación Q como $141f^{0.63}$. El sismo del 11 de mayo se sintió fuertemente en la ciudad y produjo una aceleración máxima del terreno (*PGA*) que alcanzó 80 cm/s^2. En la región se han reportado sismos relativamente grandes; e.g., 11 de febrero de 1875 en San Cristóbal de la Barranca, por lo cual resulta de interés emplear los registros de las estaciones acelerográficas para estimar los parámetros pico del movimiento del terreno debidos a escenarios sísmicos con $M_w \leq 6.0$ utilizando la teoría de vibraciones aleatorias (RVT) y las técnicas de la función de Green empírica (EGF). A partir de simulaciones empleando RVT, los valores de *PGA* esperada, velocidad pico (*PGV*) y desplazamiento pico (*PGD*) del movimiento del terreno en las estaciones acelerográficas para un sismo M_w6.0 en la región de la fuente de la secuencia son 195 cm/s^2, 10 cm/s y 3 cm, respectivamente. Las estimaciones obtenidas a partir de la técnica de EGF son más altas que las calculadas con RVT en un factor de no mayor de dos.

Palabras clave: secuencia de sismos de Guadalajara, valores pico de movimiento del terreno, peligro sísmico en Guadalajara.

S.K. Singh*
X. Pérez-Campos
A. Iglesias
V. H. Espíndola
Instituto de Geofísica
Universidad Nacional Autónoma de México
Ciudad Universitaria
Delegación Coyoacán, 04510
Mexico CDMX, México
*Corresponding author: krishna@geofisica.unam.mx

D. Arroyo
Departamento de Materiales
Universidad Autónoma Metropolitana
Mexico CDMX, México

L. Ramírez
C. Pérez
H. Sandoval
Instituto de Ingeniería
Universidad Nacional Autónoma de México
Ciudad Universitaria
Delegación Coyoacán, 04510
Mexico CDMX, México

Abstract

We analyze an earthquake sequence which occurred 24 km NNW from Guadalajara Cathedral. The activity began on 15 December, 2015 with an M_w4.1 earthquake and resumed, again, on 11 May, 2016 when the largest earthquake of the sequence, M_w4.8, occurred. The earthquakes were recorded in the city by two accelerographs and at larger distances by broadband seismographs. The source region of the sequence is located in the north of the broad junction formed by NW-SE trending Tepic-Zacoalco rift, N-S trending Colima rift, and E-W trending Chapala rift. The focal mechanism of the largest event is characterized by: strike φ = 21º, dip δ= 49º, and rake λ= -86º, with horizontal tensional axis trending 110º. This mechanism is not consistent with NE-SW direction of motion measured on fault strike by Barrier *et al*. (1990) ~ 35 km WNW of Guadalajara. It also differs from the mechanism reported in a previous study for a seismic sequence in the Zacoalco rift about 60 km south of Guadalajara. Similarities among recorded waveforms at the accelerographic stations suggest that the mechanism of other events in the sequence were similar and the events were located in a small volume, probably 1 to 2 km in radius. From the analysis of the recordings of the 11 May shock along the Trans-Mexican Volcanic Belt, from Ceboruco volcano to the west and Popocatepetl volcano to the east, the attenuation parameter Q as $141f^{0.63}$ was estimated. The earthquake on 11 May was felt very strongly in the city and produced peak ground acceleration (*PGA*) reaching 80 cm/s^2. Relatively large earthquakes have been reported in the region; e.g., on 11 February, 1875 near the town of San Cristobal de la Barranca, about 40 km NNW of Guadalajara, therefore, the interest on using recordings from accelerographic stations to estimate peak ground motion parameters for scenario earthquakes of $M_w \leq 6.0$ using random vibration theory (RVT) and empirical Green's function (EGF) techniques. From RVT simulations, the expected *PGA*, peak ground velocity (*PGV*), and peak ground displacement (*PGD*) at the accelerographic stations from an M_w6.0 earthquake in the source region of the sequence are 195 cm/s^2, 10 cm/s, and 3 cm, respectively. The predictions from the EGF technique are somewhat higher but still within a factor of two of the RVT predictions..

Key words: Guadalajara earthquake sequence, peak ground motion, Seismic hazard in Guadalajara.

Introduction

The Trans-Mexican Volcanic Belt (TMVB) is an east-west trending calc-alkaline volcanic arc related to the subduction of oceanic Rivera and Cocos plates below Mexico along the Middle America trench. The belt is traversed by networks of faults that are nearly parallel and orthogonal to its axis (e.g., Pasquaré *et al*., 1987; Johnson and Harrison, 1990; Suter *et al*., 2001). Seismicity in the TMVB is relatively low, and the seismic networks in the region are sparse. As a consequence, source parameters of earthquakes that occur in the TMVB, including their depths and focal mechanisms, are known for only a handful of earthquakes. The occurrence of large earthquakes in the TMVB is well documented. Acambay earthquake of 1912 (M_S7.0), which occurred in the central part of TMVB (Urbina and Camacho, 1913), about 100 km WNW of Mexico City, is one example. Jalapa earthquake of 1920 (M_w6.4), near the eastern end of the TMVB, caused many deaths related to a triggered landslide and was damaging to the city (Camacho and Flores, 1922). Suárez *et al*. (1994) report a large earthquake in 1568 (M~7) in/near Guadalajara in the western part of the TMVB which caused severe damage to the city. A relatively large earthquake occurred on 11 February, 1875 destroying the town of San Cristóbal de la Barranca located about 40 km NNW of Guadalajara (García Acosta and Suárez Reynoso, 1996). Clearly, cities and towns in the Mexican Altiplano are exposed to seismic hazard from earthquakes in the TMVB. A reliable estimation of this hazard, however, will only be possible by performing detailed studies of all well-recorded TMVB earthquakes; fortunately, the reported number of such events is increasing due to improvement in the seismic instrumentation of the region and quick deployment of digital portable seismographs in the field. As examples, recent well-studied earthquake sequences in the TMVB are cited, which occurred in Zacoalco, Jalisco (Pacheco *et al*., 1999), Sanfandila, Querétaro (Zúñiga *et al*., 2003), and Morelia, Michoacán (Singh *et al*., 2012).

In December 2015 and May 2016 an earthquake sequence occurred NNW of Guadalajara. The source region of the sequence is located to the north of the broad triple rift junction formed by NW-SE trending Tepic-Zacoalco, N-S trending Colima, and E-W trending Chapala rifts (Figure 1). The rifts of Tepic-Zacoalco and Colima are forming the northern and eastern boundaries of the Jalisco block which is separating from the North America plate. Active rifting is occurring

along these boundaries (e.g., Barrier *et al*., 1990; Allan *et al*., 1991; Michaud *et al*.,1994; Moore *et al*., 1994). The seismic sequence was recorded in the city by two accelerographs at an epicentral distance of about 20 km. The largest earthquake in the sequence (M_w4.8) occurred on 11 May, 2016, and was strongly felt in the city but caused no damage (R. Meli, personal communication, 2016). This event was also extensively recorded by the broadband seismographic network of the National Seismological Service (SSN). In this paper the source characteristics of some of the larger events of the sequence are studied and the attenuation parameter, Q, along central-west TMVB is estimated. Taking advantage of the recordings at the two accelerographic stations, an estimation of ground motions from scenario earthquakes of M_w5.5 and 6.0 in the source region of the sequence are performed. The results should be useful in seismic hazard estimation of Guadalajara from normal-faulting crustal earthquakes in the region.

Location, focal mechanism, and magnitude

As mentioned before, the sequence began on 15 December, 2015 with an earthquake of magnitude M_w4.1 located ~ 20 km NW of Guadalajara. SSN reported three more events in the next 40 hours. The activity resumed on 11 May, 2016 with a M_w4.8 earthquake, the largest event of the sequence. SSN reported 29 other events in the next 18 days. The closest SSN station which recorded these events was more than 100 km away and the *P* waves at the SSN stations were highly emergent. The sequence was also recorded by two accelerographs located on the campus of Universidad Panamericana (station GDLP) and Colegio Cervantes (station GDLC) (Figures 1 and 2). These stations are operated by Instituto de Ingeniería, UNAM. Recordings at these stations are made in continuous mode at 100 samples/s. Due to the noise level at these stations (especially at GDLC), very high during traffic hours at frequencies above about 8 Hz,

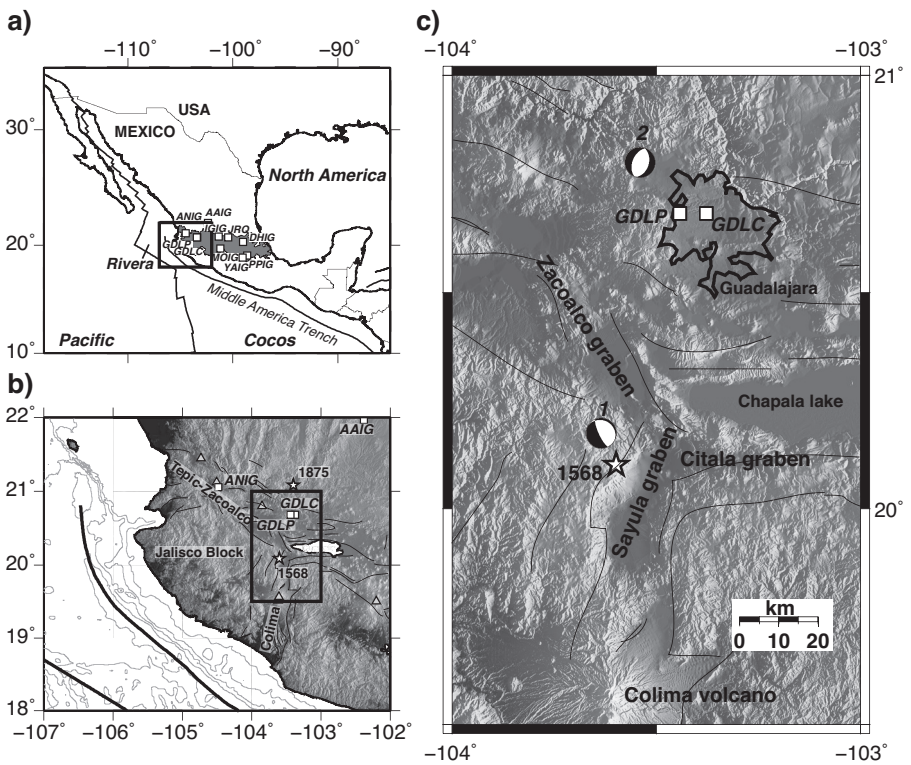

Figure1. a) Tectonic setting of the region. Gray area: Trans-Mexican Volcanic Belt. Rectangles: broadband stations in the belt which recorded 11 May, 2016 (M_w4.8) earthquake. Enlarged map of the area in the black rectangle is shown in b). b) Tectonic setting of west-central Mexico showing the Jalisco block and the rift-rift-rift triple point junction. Triangles: active volcanoes. Squares: accelerographic (GDLC and GDLP) and broadband (AAIG and ANIG) stations in the region. Stars correspond with the approximate epicenters for large historical earthquakes reported in the region. An enlarged view of the rectangular area, the region of interest, is shown on the right. c) Shaded relief map of the area around Guadalajara; its metropolitan area is enclosed within the black contour. Locations of seismic sequences of Zacoalco (1) and Guadalajara (2) are shown by their common focal mechanisms. Modified from Pacheco *et al*. (1999). Star corresponds with the approximate epicenter for the 1568 earthquake.

data are useful for $M \geq 3.0$ events only. However, a few earthquakes of smaller magnitudes also produced useful recordings when they occurred late at night or early in the morning. In total there were eight well-recorded events at these stations. These events, along with *PGA*, *PGV*, and *PGD* values, are listed in Table 1. We note that many historical monuments of the city, including the cathedral, are located only ~ 2 km eastward of the station GDLC (Figure 2). Hence, it is likely that the ground motions near these monuments were similar to those recorded at the station GDLC.

Figure 3 shows displacement seismograms at the station GDLP of six of the eight earthquakes listed in Table 1. The traces begin 0.5 s before the *P*-wave arrival. The vertical dotted lines in the top three frames indicate arrival of *P* and *S* waves. (*S*-*P*) time of the events which occurred during December 2015 is 2.5 s. The remarkable similarity of the waveforms and nearly the same (*S*-*P*) times of these events suggest nearly the same location and focal mechanism of these events. The bottom three frames correspond to the activity in May 2016. The largest shock of the sequence (11 May, 2016, M_w4.8) appears somewhat complex but still with (*S*-*P*) time of 2.5 s. Although the waveform of 15 May, 2016 event (bottom, second frame) differs somewhat from the others (probably reflecting its greater depth as reflected in the impulsive *P* wave), its (*S*-*P*) time is still about 2.5 s. The (*S*-*P*) time of the smallest event shown in the figure (bottom, third frame) is 0.1 s less than the others, suggesting its location ~1 km closer to the station than others.

The largest event of the sequence (11 May, 2016; 22:35) was located using *P* and *S* phases at the two local accelerographic stations and many broadband stations of SSN (distance > 100 km). Because of its size, this was the best-recorded event. Even so, the first motions could be read only at a handful of stations. The seismograms were converted to Seisan format (Havskov and Ottemöller, 1999) and the earthquake was located using the algorithm of Lienart and Havskov (1995) yielding the epicenter at 20.798 ºN, 103.539 ºW, with a poorly constrained depth of 8 km. Given the similarity of (*S*-*P*) times and the waveforms (Figure 3), we conclude that the earthquakes in Table 1 (and most of the events during the entire sequence) were tightly clustered, probably within a volume of 1 to 2 km radius.

The fault parameters of the 11 May, earthquake were determined by performing regional moment tensor (RMT) inversion using an algorithm implemented by A. Iglesias at the Servicio Sismológico Nacional (SSN, Mexican National Seismogical Service). The

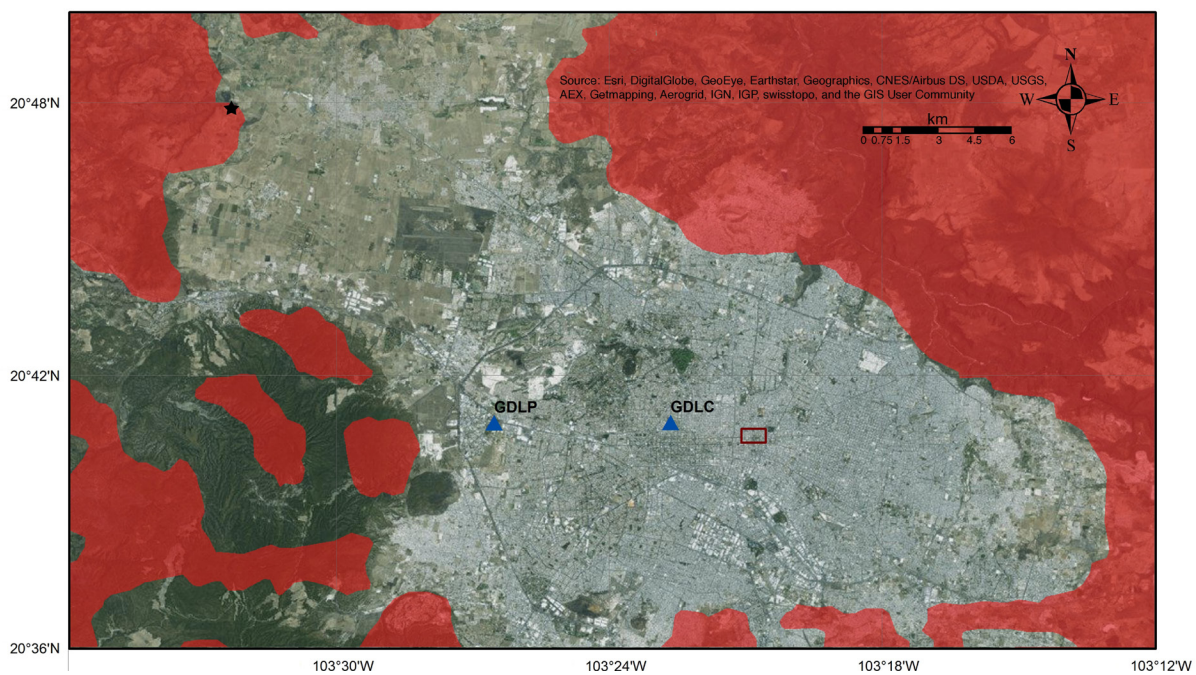

Figure 2. Map of Guadalajara and vicinity. Star: the epicenter of 11 May, 2016 (M_w4.8) earthquake. Triangles: accelerographic stations (GDLP and GDLC). Rectangle: area of famous monuments of the city. The red shaded area corresponds with presence of igneous intrusive rocks.

Table 1. *PGA*, *PGV*, and *PGD* of well-recorded events at two near-source stations ($R \sim 20$ km) during the December 2015 and May 2016 Guadalajara earthquake sequence.

			Station GDLP[1]			Station GDLC[2]		
			PGA cm/s^2 PGV cm/s PGD cm			PGA cm/s^2 PGV cm/s PGD cm		
Event number	Date Time	*M*w	NS	EW	Z	NS	EW	Z
1	2015-12-15 16:09	4.06	20.2 4.40E-01 2.70E-02	31.6 5.90E-01 4.50E-02	15.2 3.10E-01 1.60E-02	14.3 4.30E-01 4.20E-02	15.6 4.60E-01 3.70E-02	9.1 2.00E-01 1.00E-02
2	2015-12-15 16.32	2.88	3.7 6.30E-02 2.10E-03	4.1 6.70E-02 2.80E-03	2.5 4.70E-02 1.00E-03	- - -	- - -	- - -
3	2015-12-15 17:49	3.50	7.1 2.30E-01 1.30E-02	14.8 2.60E-01 1.90E-02	6.6 1.40E-01 9.10E-03	6.7 1.80E-01 1.30E-02	6.6 2.10E-01 1.60E-02	5.8 1.10E-01 4.20E-03
4	2015-12-17 7:59	3.50	15.3 3.60E-01 1.40E-02	17.3 5.30E-01 2.20E-02	12 2.30E-01 1.00E-02	6.7 1.70E-01 1.30E-02	7.3 2.20E-01 1.70E-02	6.6 1.70E-01 4.30E-03
5	2016-05-11 22:35	4.77	59.4 1.40E+00 7.70E-02	79.3 2.10E+00 2.10E-01	47.9 9.40E-01 3.50E-02	54.6 2.40E+00 1.40E-01	59 1.80E+00 1.90E-01	51.5 9.40E-01 6.70E-02
6	2016-05-15 1:43	3.15	1.9 5.50E-02 2.60E-03	1.56 5.10E-02 3.70E-03	1.95 4.50E-02 1.50E-03	1.57 4.90E-02 3.10E-03	1.58 4.10E-02 2.80E-03	1.56 3.80E-02 1.00E-03
7	2016-05-16 8:14	2.77	1.08 2.30E-02 8.30E-04	1.89 3.50E-02 1.80E-03	1.08 2.10E-02 4.90E-04	8.00E-01 1.40E-02 7.50E-04	1.12 2.10E-02 1.10E-03	6.80E-01 1.40E-02 4.00E-04
8	2016.05-29 6:40	2.88	7.70E-01 1.90E-02 7.90E-04	4.80E-01 1.30E-02 4.10E-04	7.30E-01 1.70E-02 4.10E-04	7.00E-01 1.90E-02 9.10E-04	3.50E-01 1.20E-02 6.00E-04	5.60E-01 1.20E-02 3.00E+04

[1]GDLP: Guadalajara, Universidad Panamericana.
[2]GDLC: Guadalajara, Colegio Cervantes.

method is described in some detail in UNAM Seismology Group (2010). System chooses appropriate broadband stations according to reported magnitude. Records from stations relatively close to the epicenter are discarded to avoid finite fault effects, and stations far from the epicenter are discarded to ensure good signal to noise ratio. Records of selected stations are integrated to obtain displacements and are band-pass filtered using frequencies that depend on magnitude criteria. This procedure tries to use low frequencies (where displacement spectrum is flat), avoiding high frequencies at which the structure is poorly known. Selected seismograms are inverted using a time domain scheme implemented by Dreger (2003). Computation time is dramatically reduced using a set of stored Green functions, which are computed at nodes of a grid of distances *vs*. depths and using an average *S*-wave velocity model. For Mexico, the SSN uses a model reported by Campillo *et al*. (1996).

The regional centroid moment tensor solution of the 11 May, earthquake reported by the SSN yields the following fault parameters: strike $\varphi = 21^{\circ}$, dip $\delta = 49^{\circ}$, strike $\lambda = -86^{\circ}$, and $M_0 = 1.8 \times 10^{16}$ Nm (M_w4.77). An inversion using a different combination of broadband stations $\varphi = 2^{\circ}$, $\delta = 49^{\circ}$, $\lambda = -123^{\circ}$, with $M_0 = 9.9 \times 10^{15}$ Nm (M_w4.60). As illustrated in Figure 4, both of these mechanisms are consistent with the first motion data; both show a nearly horizontal

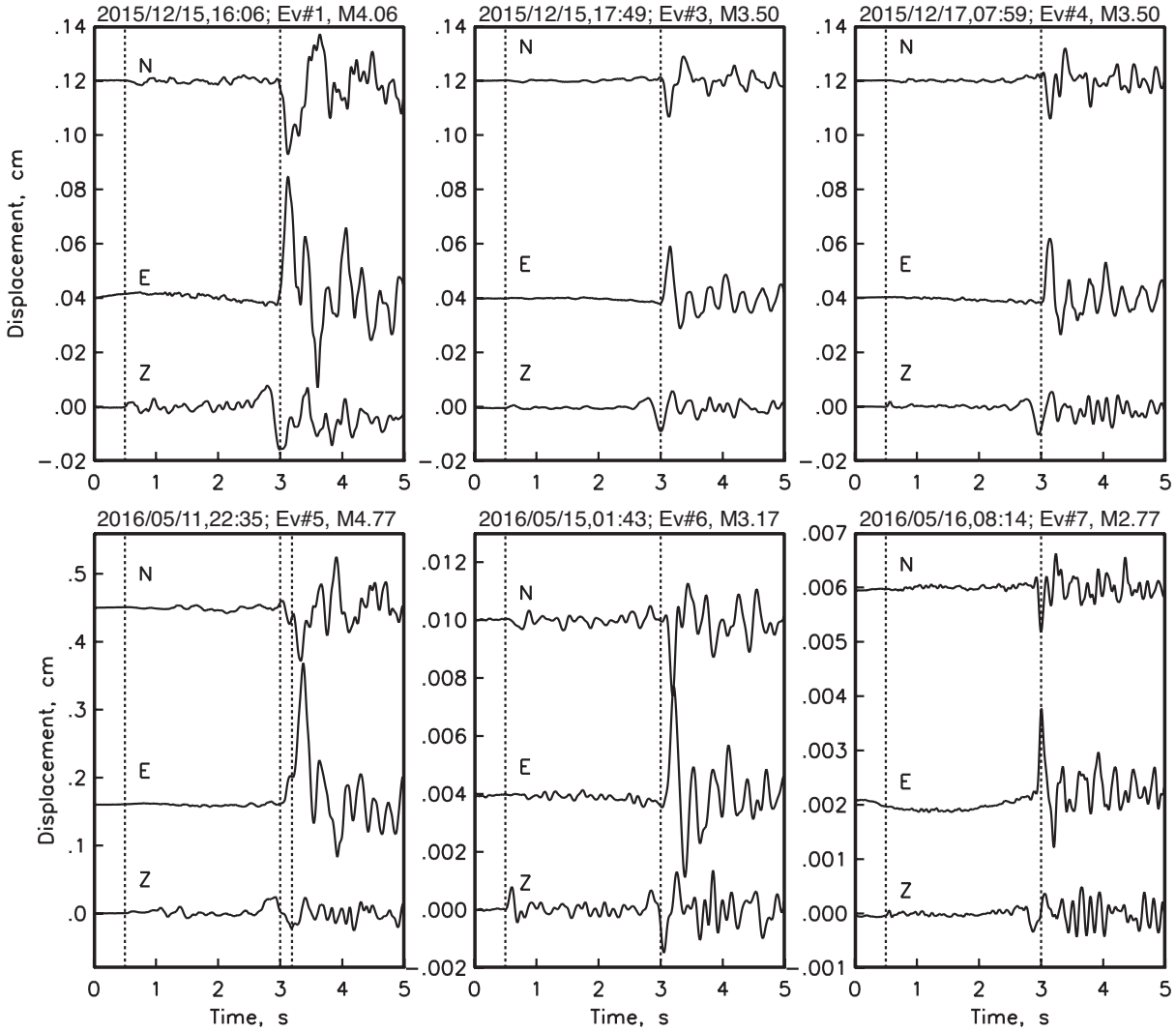

Figure 3. Displacement seismograms at the station GDLP of six of the larger earthquakes of the sequence which had clear signal at the station. Traces begin 0.5 s before *P*-wave arrival. Vertical dotted lines in the top three frames indicate the arrival of *P* and *S* waves, respectively. (*S*-*P*) time for these events, which occurred in December 2015, is 2.5 s. The remarkable similarity of the waveforms and nearly the same (*S*-*P*) times of these events suggest nearly the same location and focal mechanism of these events. The bottom three frames correspond to the activity in May 2016. The largest shock of this sequence appears complex but still with (*S*-*P*) of 2.5 s. Although the waveform of 15 May, 2016 event (second bottom frame) differs from others (probably reflecting its larger depth; note the impulsive *P* waves), its (*S*-*P*) time is still about 2.5 s. (*S*-*P*) time of the smallest event shown in the figure (bottom third frame) is 0.1 s less than the others, suggesting that it was located about 1 km closer to the station than others.

tensional axis trending ~ 110º. The figure also shows displacement traces of the earthquake at the station GDLP along with infinite space synthetics (Singh *et al*., 2000) corresponding to the two mechanisms. In these synthetics the effect of the free surface is approximately taken into account by multiplying infinite-space synthetics by two. The first solution above (φ = 21º, δ = 49º, λ = -86º) provides a better fit to the observed *S* pulse and is our preferred focal mechanism. We note that the mechanisms in Figure 4 differ from those reported 60 km to the south in the Zacoalco graben during the seismic sequence of 1997, which involved a NE-SW extension, consistent with the orientation of the rift (Pacheco *et al*., 1999).

To estimate the magnitudes of smaller events of the sequence listed in Table 1, Fourier acceleration spectra of the *Z*-component at the broadband station AAIG in Aguascalientes (Figure 1) was computed. All events listed in Table 1 were well recorded at this station. The spectra and the spectral ratios of 11

May, 20016 earthquake with respect to each of the other seven events are illustrated in Figures 5a and 5b, respectively. Taking the seismic moment of the 11 May earthquake as 1.8×10^{16} Nm, we estimated moments (hence M_w) of other events from the level of spectral ratios at low frequencies. Table 1 lists M_w of all events. If we take $M_0 = 9.9 \times 10^{15}$ Nm for the 11 May earthquake, as obtained from the second regional CMT solution, then M_w of all events will be 0.18 unit less.

Q along the Central-West TMVB

Attenuation parameter, Q, in the central and eastern TMVB has been studied by several authors. As discussed by Singh *et al*. (2007), the reported estimates of Q are inconsistent among the studies (see Figure 6). To our knowledge, no estimation of Q is available for the central-west segment of the TMVB.

The earthquake of 11 May, 2016 was recorded by eight broadband seismographs in the TMVB, extending from Ahuacatlán, near Ceboruco volcano (station ANIG) in the west and to Popocatepetl volcano (station PPIG) in the east, covering a distance range of about 650 km (Figure 1a). We use this dataset, along with the accelerograms in Guadalajara, to obtain a preliminary estimate of an average Q for the central-west TMVB. Note that we have included data from station AAIG in the analysis even though the wave path is not entirely through the TMVB. A procedure which has been used before in similar studies was used (e.g., Singh *et al*., 1982; Ordaz and Singh, 1992; García *et al*., 2004). Here the method is briefly described.

The Fourier acceleration spectral amplitude, $A(f, R)$, of the intense part of the ground motion of an event at distance R, considering the far-field point-source approximation, can be written as

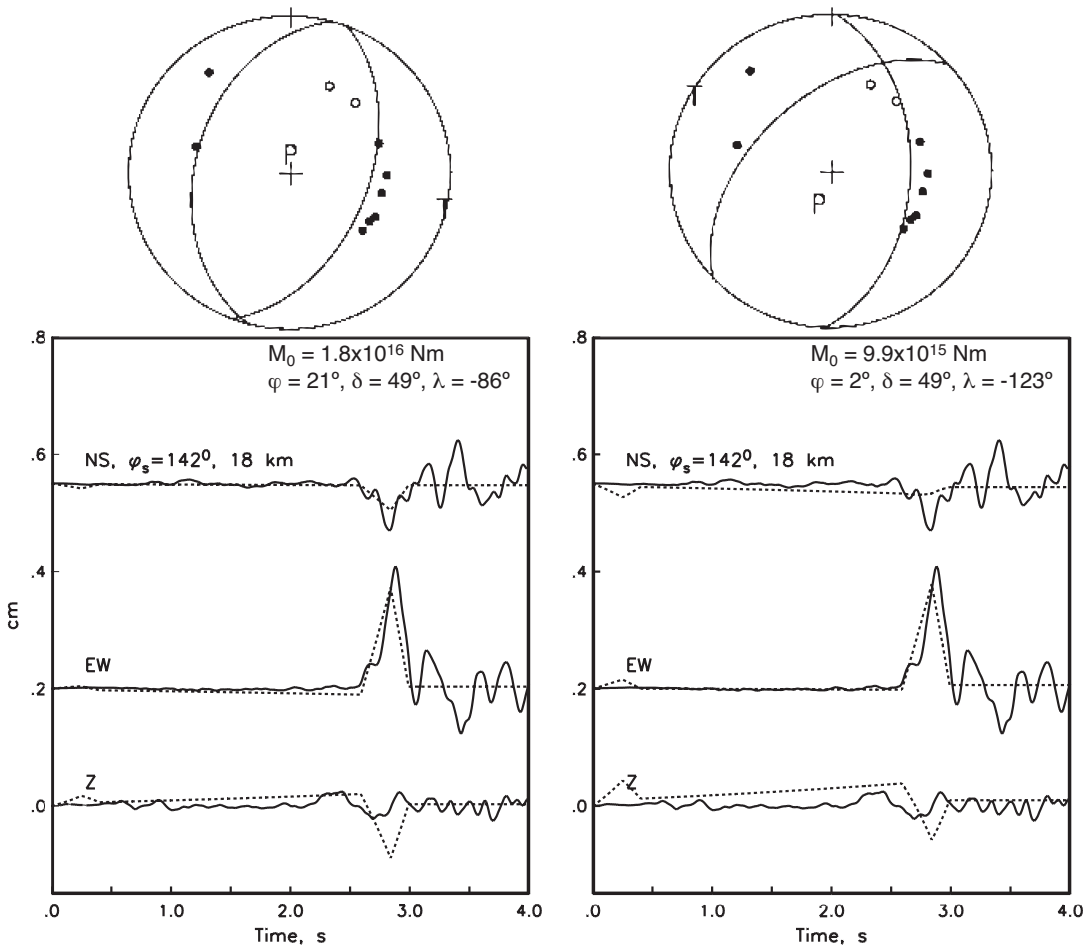

Figure 4. (Top) Focal mechanism of 11 May, 2016 earthquake. Two regional CMT solutions, using a different combination of broadband stations, are shown. First motions agree with both solutions. (Bottom) Displacement traces at station GDLP and infinite space synthetics corresponding to the two regional CMT solutions.

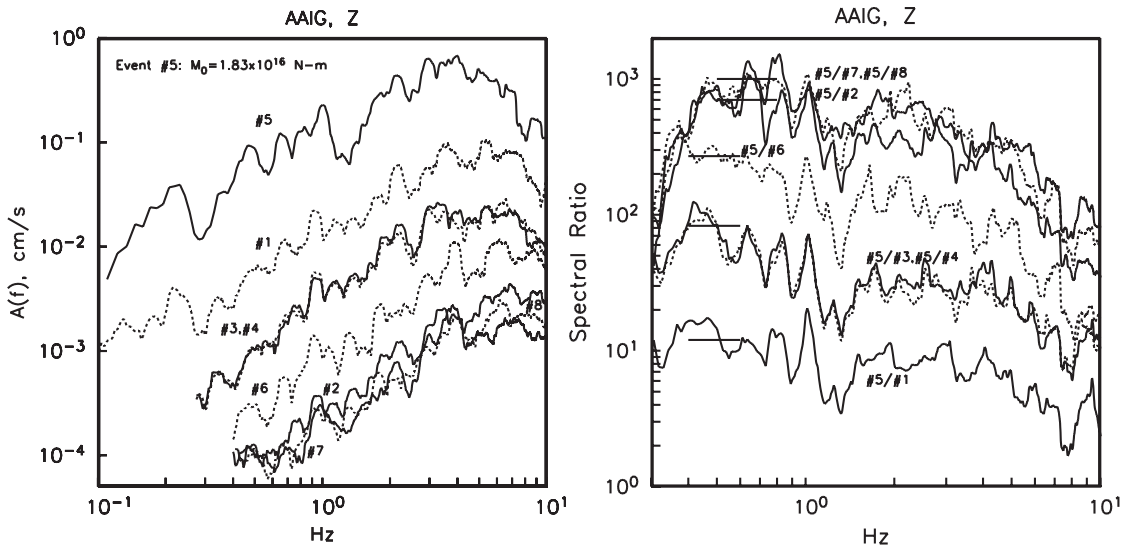

Figure 5. (Left) Fourier acceleration spectra (*Z*-component) of eight earthquakes at station AAIG (Figure 1). (Right) Spectral ratios of May 11, 2016 event (M_w4.8) with respect to the other seven events. As the seismic moment of 11 May, 2016 is known (M_0 = 1.83x10^{16} Nm), the ratios at low frequencies yield an estimate the moment (hence M_w) of the other seven events (Table 1).

$$A(f,R) = C \cdot G(R)\,[\{f^2 \dot{M}_0(f)\}\,Site(f)\,e^{-\pi\kappa f} B(f)]\,[e^{-\pi f R/\beta Q(f)}] \qquad (1)$$

where,

$$C = FPR_{\theta\varphi}(2\pi)^2/(4\pi\rho\beta^3). \qquad (2)$$

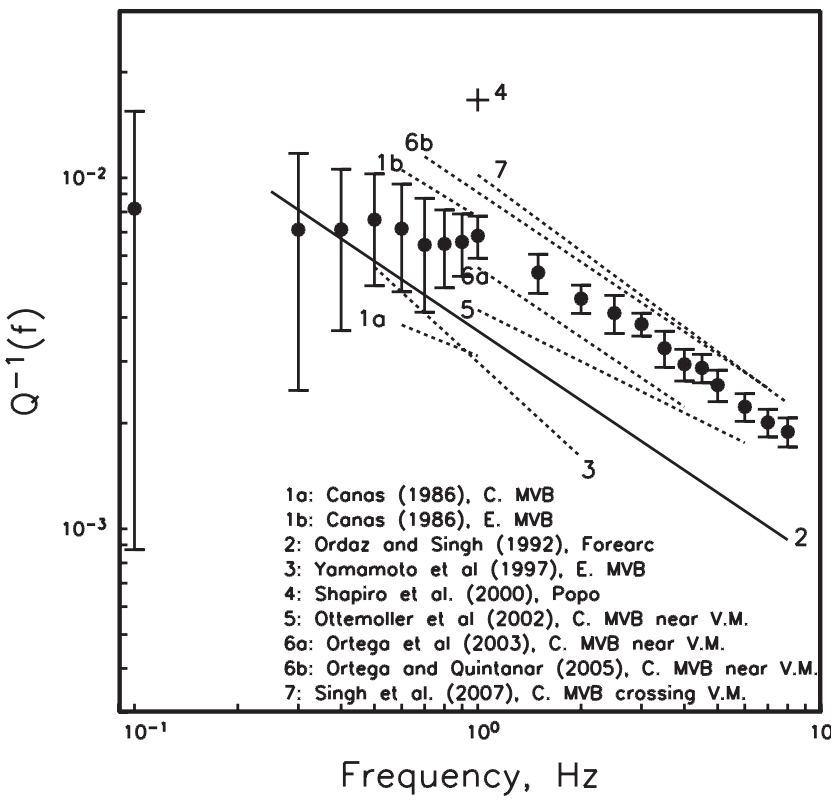

Figure 6. $Q^{-1}(f)$ of central-west TMVB estimated in this study (dots) and in other segments of TMVB reported in previous works. For comparison, Q^{-1} of *Lg* waves in the forearc region is also shown. Modified from Singh *et al*. (2007).

In equations above, $\dot{M}_0(f)$ is the moment rate spectrum so that $\dot{M}_0(f) \rightarrow M_0$ (the seismic moment) as $f \rightarrow 0$, R = hypocentral distance, $R_{\theta f}$ = average radiation pattern (0.55), F = free surface amplification (2.0), P takes into account the partitioning of energy in the two horizontal components ($1/\sqrt{2}$), b = shear-wave velocity at the source (taken here as 3.5 km/s), r = density in the focal region (assumed 2.85 g/cm^3), and $Q(f)$ = quality factor, which includes both anelastic absorption and scattering. The attenuation in the near-surface layer and the finite bandwidth of the observed spectrum imposed by the sampling rate are accounted by the parameter κ (Singh *et al*., 1982; Anderson and Hough, 1984) and/or the Butterworth filter, $B(f)$. Following Boore (1983), we take $B(f) = (1.0 + (f/f_m)^8)^{-0.5}$. We will assume that κ is independent of R. *Site* (f) in Equation (1) is the local site effect. We take the geometrical spreading term, $B(R)$, in Equation (1) as 1 / R for $R \leq$ 100 km and 1 / $(100R)^{0.5}$ for $R >$ 100 km. Taking logarithm of Equation (1) yields:

$$\log[A(f,R)] = \log C + \log G(R) + [\log\{f^2 \dot{M}_0(f)\} + \log B(f) + \log Site(f) - 1.36\kappa f] - [1.36\{Rf/\beta Q(f)\}]. \quad (3)$$

The terms in the first square bracket on the right-hand side depend on f but are independent of distance R. Equation (3) was solved in the least squares sense to obtain $Q^{-1}(f)$ and the quantity in the first square bracket at each frequency. Isolating the source acceleration spectrum, $f^2 \dot{M}_0(f)$ would require knowledge of *Site*(f), κ, and f_m. Here the only interest is Q^{-1}. Figure 6 shows Q^{-1} as a function of f. A least squares fit to the data in the frequency range 1 – 8 Hz yields $Q(f) = 141f^{0.63}$. The figure also shows $Q^{-1}(f)$ for the TMVB reported in previous studies and that obtained by Ordaz and Singh (1992) for interplate earthquakes in the forearc region of Mexico. As expected, a stronger attenuation (low Q) is, generally, observed in the TMVB than in the forearc region. However, as mentioned earlier, there is a large variation in the reported $Q^{-1}(f)$ in the TMVB. This may partly reflect smaller scale variation in the attenuation. Unfortunately, there are large differences in the reported $Q^{-1}(f)$ for the same region also (see, e.g., the values reported for the central or the eastern MVB in Figure 6). Thus, the variability in the reported $Q^{-1}(f)$ is partly also due to the difference in the data set as well as the methodology used in the analysis.

Ground motion in Guadalajara during larger, postulated earthquakes

Observed *PGA*, *PGV*, and *PGD* at GDLP and GDLC during the Guadalajara sequence are plotted as a function of M_w in Figure 7. It is clearly of practical interest to estimate these ground motion parameters for postulated larger earthquakes which may occur in the same source region. Here the motions from $M_w \leq 6.0$ events are estimated. The occurrence of a M_w5.5-6.0 earthquake in the same source region as the sequence or within R~20 km from the center of Guadalajara certainly does not seem farfetched. The San Cristóbal de la Barranca town, which suffered destruction (García Acosta and Suárez Reynoso, 1996) during the 11 February, 1875 earthquake is ~ 30 km NNE of the source region present sequence. The region is seismically active

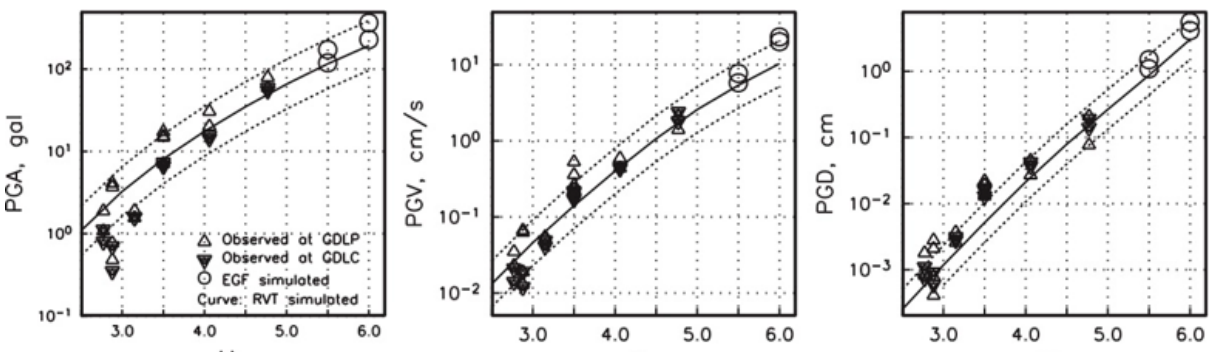

Figure 7. Observed, horizontal *PGA*, *PGV*, and *PGD* at stations GDLP and GDLC, located in Guadalajara (R~20 km), as a function of M_w. The curve shows prediction from RVT (see text). Circles indicate synthesized peak motions for postulated earthquakes of M_w5.5 and 6.0 using recordings of 15 December, 2015 (M4.1) as empirical Green's functions.

with potential for large earthquakes; thus it is relevant to estimate plausible ground motions during the scenario earthquakes. In this paper, two techniques were used, one based on random vibration theory (RVT) and the other exploiting summation of empirical Green's functions (EGFs).

Estimation based on RVT

If the Fourier's acceleration amplitude spectrum $A(f, R)$ and duration of the intense ground motion at a site can be estimated, then the peak ground motion parameters can be obtained through the application of RVT (see Boore, 2003 for an extensive review of the method). Here, $A(f, R)$ was estimated using Equation (1). We assume that the sources follow Brune ω^{-2} model, i.e.,

$$\dot{M}_0(f) = M_0 f_c^2/(f^2 + f_c^2),$$

where M_0 is the seismic moment, and f_c is the corner frequency which is related to the source radius, a, by $f_c = 2.34\beta / 2\pi a$ (Brune, 1970). The radius, in turn, is related to stress drop, $\Delta\sigma$, by $\Delta\sigma = (7/16)(M_0/a^3)$. We further assume that $\Delta\sigma$ is constant and equals 100 bar. As estimated above, we take $Q(f) = 141f^{0.63}$. An inspection of spectra at stations GDLP and GDLC suggest f_m = 18 Hz. The high-frequency fall off of the observed spectra additionally requires κ = 0.01 s. The spectrum was first computed using the parameters above and Equation (1) but neglecting the site amplification term, i.e., assuming *Site*(f) = 1. The ratio of observed to the computed spectrum yields an estimate of *Site*(f). The process is illustrated in figures 8a and 8b which show median and plus/minus one standard deviation curves of the observed horizontal spectra at stations GDLP and GDLC for 15 December, 2015 (M_w4.1) and 11 May, 2016 (M_w4.8) earthquakes, respectively. The figures also show the computed spectrum assuming *Site* (f) =1. The ratio of the observed median spectrum to the computed spectrum, *Site*(f), is shown in Figure 8c for the two events, along with the median *Site*(f). We use the median *Site*(f) in Equation (1) to estimate median $A(f,R)$ at stations GDLP and GDLC. A critical parameter needed in the application of RVT is the duration of intense part of the ground motion, T_s, which was taken as $T_s = 1/f_c + 0.05R + C$, where R is in km. We take $C = 3.0$ based on an earlier analysis of an earthquake sequence in Morelia (Singh *et al*., 2012). we note that C = 0 in the relation proposed by Herrmann (1985). The predicted *PGA*, *PGV*, and *PGD* curves as a function M_w are shown in Figure 7. The dashed curves in the figure correspond to twice and half the predicted RVT curve. These curves bracket most of the observed data. From RVT simulation, the expected *PGA*, *PGV*, and *PGD* at the accelerographic stations from a M_w6.0 earthquake in the source region of the sequence with $\Delta\sigma$ = 100 bar are 195 cm/s^2, 10 cm/s, and 3 cm, respectively. The computations with $\Delta\sigma$ = 30 bar and 300 bar were repeated. The estimated values fall between the dashed curves in Figure 7. Assuming 30 to 300 bar as the likely range for the stress drop, then the dashed curves in Figure 7 provide the range of the expected peak values.

Estimation based on random summation of empirical Green's function

The recordings of a smaller earthquake can be used as empirical Green's functions (EGFs) to synthesize expected ground motions during a postulated larger earthquake in the same source region. Here we use the recorded motion at the station GDLP during the 15 December, 2015 earthquake (M_w4.1) as the EGF. We follow method proposed by Ordaz *et al*. (1995) which assumes that far-field and point-source approximations are valid. The summation scheme obeys the ω^2-source scaling law at all frequencies and produces realistic time histories. The method requires specification of only the seismic moments and the stress drops of the EGF and the target events. Here we assume the same stress drop, $\Delta\sigma$, for the EGF and target events and take it as 100 bar. Figure 7 shows synthesized peak ground motions on NS and EW components (average of 30 simulations) for the postulated M_w 5.5 and 6.0 earthquakes. The peak values follow the trend of the recorded data and are in agreement, within a factor of two, with the RVT predictions. Simulated motions assuming $\Delta\sigma$ of 30 and 300 bar are, generally, lower and higher by about 20 to 40%, respectively.

The EGF recordings and sample simulated time histories corresponding M_w5.5 and 6.0 earthquakes are displayed in Figure 9. The simulated traces appear realistic. They provide an estimate of expected ground motions in the center of Guadalajara during these scenario earthquakes.

Discussion and Conclusions

The similarity of waveforms and constant (*S-P*) time of 2.5 s at the accelerographic station GDLP for all well-recorded eight events of the earthquake sequence suggest that the activity was confined to a small volume, probably about 1 to 2 km in radius, and the focal mechanisms were nearly the same. The

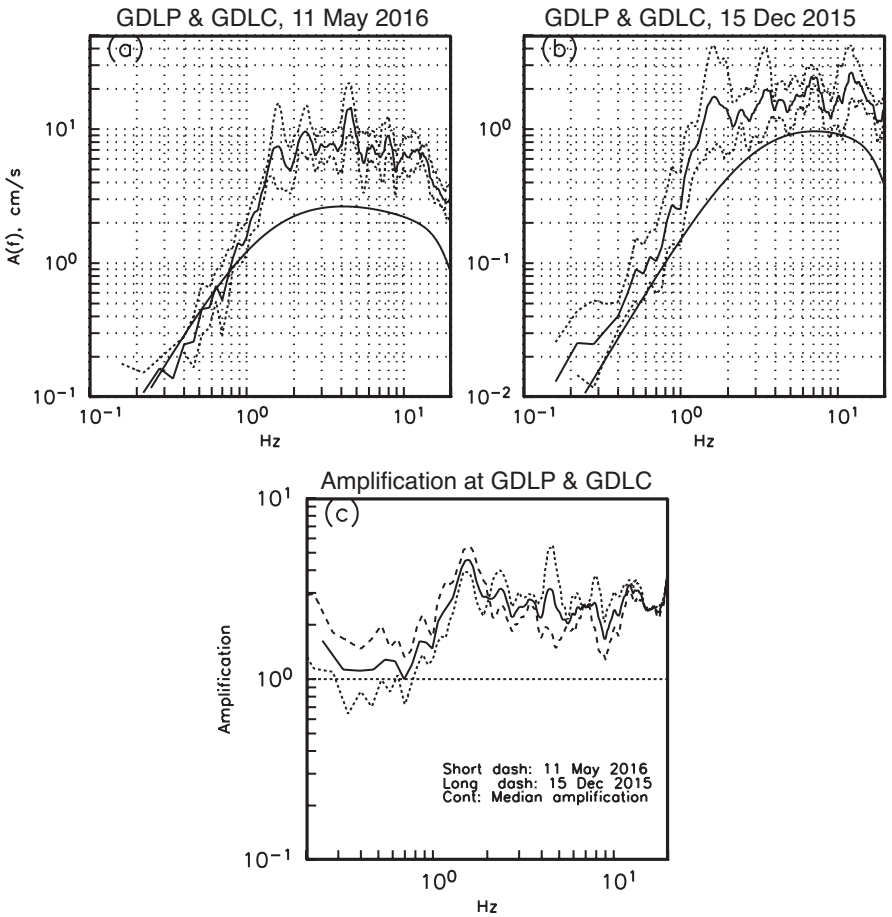

Figure 8. (a) Median and plus/minus one standard deviation of observed Fourier acceleration spectra (horizontal components) at stations GDLP and GDLC during the 11 May, 2016 (M_w4.8) earthquake. Also shown are corresponding theoretical spectra assuming ω^{-2} Brune source model with $\Delta\sigma$ = 100 bar, $Q(f)$ = 141$f^{0.63}$, f_{max} = 18 Hz, and κ = 0.01 s and ignoring the site effect. (b) Same as (a) but for the 15 December, 2015 (M_w4.1) earthquake. An estimation of median site effect at stations GDLP and GDLC is obtained from the ratio of observed to theoretical spectra. (c) Estimated site effects during 15 December, 2015 and 11 May, 2016 earthquakes. The continuous curve shows the median site effect.

focal mechanism of the largest earthquake of the sequence (11 May, 2016; M_w4.8) reveals normal-faulting on a NNE-SSW oriented fault, with a nearly horizontal *T* axis trending ~ 110º. This mechanism is not consistent with the NE-SW direction of motion measured on fault strike by Barrier *et al*. (1990) ~ 35 km WNW of Guadalajara.

The sequence occurred in a region where Sierra Madre Occidental volcanic province abuts the TMVB. About 80 km north of Guadalajara, near the town of Teul, large NNE trending 22 – 27 Ma old normal faults have been mapped (Moore *et al*., 1994). -N-S trending normal faults (age < 10 Ma) are found about 50 km north of Guadalajara near the town of San Cristóbal. According to Moore *et al*. (1994) the trend of these faults suggests a reactivation of older Basin and Range structures. It is possible that the present earthquake sequence occurred on one these reactivated structures.

From an analysis of the recordings of the largest event of the sequence, we obtain an estimate of the attenuation parameter, Q, in the central-west TMVB as Q = 141$f^{0.63}$. We note that this estimate is preliminary, as it is based on only one event. However, given the uncertainty in the regression, the trend is not expected to change appreciably if, and when, more data are available and are included in a similar analysis. Previous estimations of Q in the TMVB have been limited to the central and eastern segments. They differ significantly among the studies. The present Q estimate is

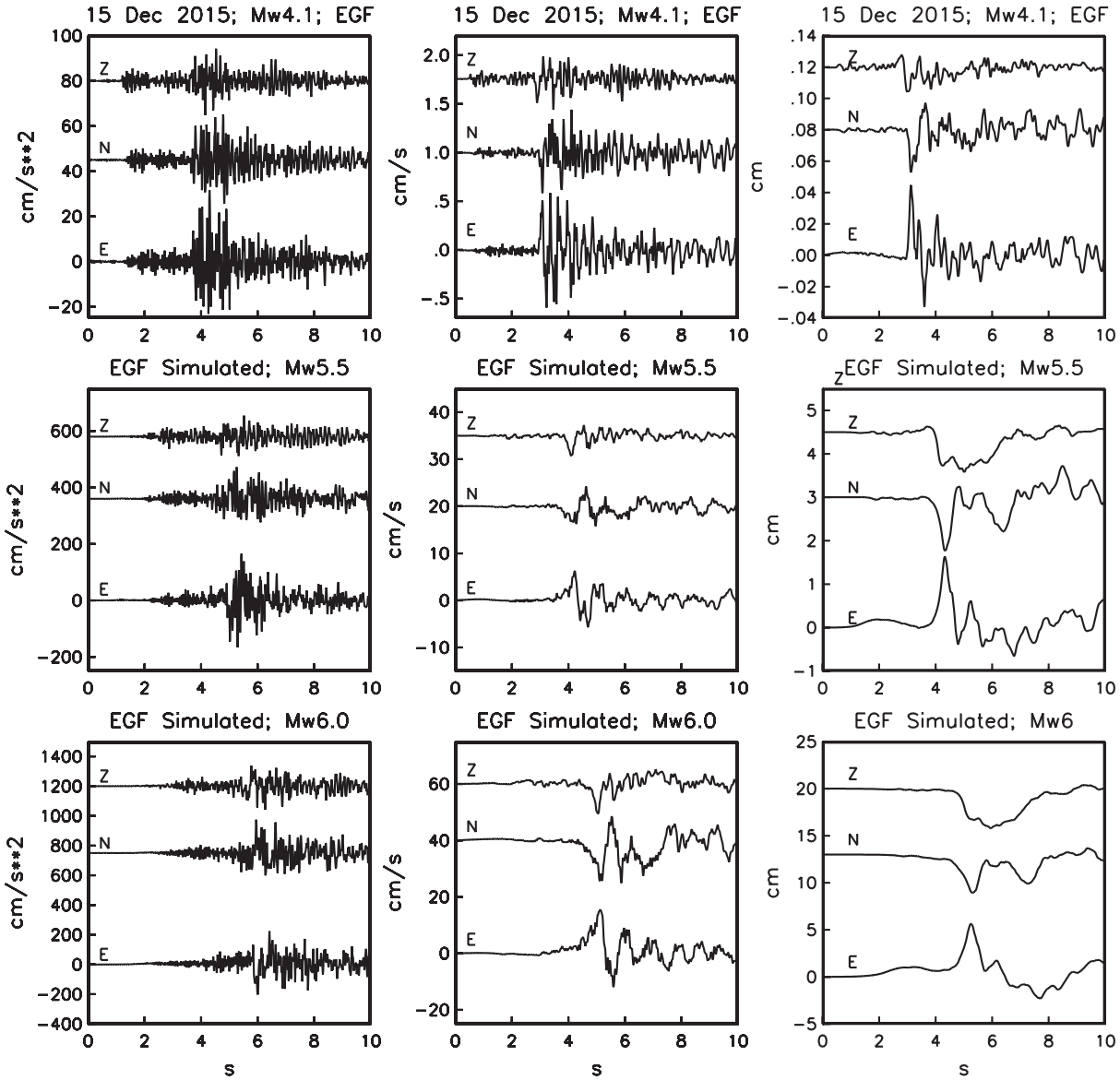

Figure 9. (Top frames) Acceleration, velocity, and displacement traces at station GDLP during the 15 December, 2015 earthquake used as EGFs. (Middle frames) Synthesized motions for a postulated M_w5.5 earthquake. (Bottom frames) Synthesized motions for a postulated M_w6.0 earthquake. Stress drops of the EGF and target events have been taken as 100 bar. Sample time histories are one realization of the synthesis.

somewhat higher than those reported in the central TMVB for paths crossing the Valley of Mexico. The Q reported here is an average over a 650 km-long path; it may be much lower for short paths crossing active volcanoes. Almost all Q estimates for the TMVB are smaller than that in the forearc region of Mexico. Lower Q (higher attenuation of seismic waves) in the TMVB may be attributed to heating and partial melting of crustal material, presence of fluids, and enhanced scattering from heterogeneities and fractures resulting from active tectonics of the volcanic belt.

Damage caused by large historical earthquakes of 1568 and 1875 are a testimony to the seismic hazard faced by Guadalajara. The causative faults of these events, however, are not known and the magnitudes are uncertain. There is also infrequent seismic activity at a small-magnitude level in the city. Ordoñez (1912) reported a swarm-like local seismic activity. Whether the activity in the city is diffused or confined to some structures is unknown. As a result of these uncertainties, scenario earthquakes for the city are difficult to postulate. Clearly, a dense

seismic network is needed in and around the metropolitan area of Guadalajara which has a population of about 4.5 million. Such a network, along with paleoseismic studies, may go a long way in identifying active faults in the region and, hence, in realistic estimation of seismic hazard. In this study, we have taken advantage of the strong motion recordings in Guadalajara during the recent seismic sequence and have estimated ground motions from $M_w \leq 6$ scenario earthquakes in the same source region. The ground motion estimates obtained from RVT and EGF techniques are in reasonable agreement with each other. These are some of the likely scenario earthquakes. The parameters used in the simulation were obtained from the strong-motion recordings. They could also be useful in the simulation of motions from other postulated scenario earthquakes.

Acknowledgments

SSN data were obtained by the Servicio Sismológico Nacional (México) and accelerographic data from Guadalajara were provided by Instrumentación Sísmica, Instituto de Ingeniería, UNAM. We especially thank the personnel of both of these institutions for station maintenance, data acquisition, transmission, processing, and distribution. The research was partly funded by DGAPA, UNAM project IN107216.

References

Allan J.F., Nelson S.A., Luhr J.F., Carmichael I.S.E., Wopat M., Wallace P.J., 1991, Pliocene-recent rifting in SW Mexico and associated Volcanism: An exotic terrain in the making. In: Dauphin, J.P., Simoneit, B.R.T., (Eds.), *The Gulf and the Peninsular Province of the Californias*, *AAPG Mem.*, 47, 425-445.

Anderson J.G., Hough S.E., 1984, A model for the shape of the Fourier amplitude spectrum of acceleration at high frequencies. *Bull. Seismol. Soc. Am.*, 74, 5, 1969-1993.

Barrier E., Bourgois J., Michaud F., 1990, Le sisteme de rifts actifs du point triple de Jalisco: vers un proto-golfe de Jalisco. *C.R. Acad. Sci. Paris,* 310, 1513-1520.

Boore D.M., 1983, Stochastic simulation of high-frequency ground motions based on seismological models of radiated spectra. *Bull. Seism. Soc. Am.,* 73, 1865-1884.

Boore D.M., 2003, Simulation of ground motion using the stochastic method. *Pageoph,* 160, 635-676.

Brune J.N., 1970, Tectonic stress and the spectra of seismic shear waves from earthquakes. *J. Geophys. Res.,* 75, 4997-5009.

Camacho H., Flores T., 1922, Memoria relativa al Terremoto Mexicano del 3 de Enero de 1920. *Boletín del Instituto de Geológico de México*, 38-39.

Campillo M., Singh S.K., Shapiro N., Pacheco J., Hermann R.B., 1996, Crustal structure of the Mexican volcanic belt, based on group velocity dispersion. *Geofísica Internacional*, 35, 4, 361-370.

Canas J.A., 1986, Estudio de factor inelástico Q de la coda de los terremotos correspondientes a las regions central y oriental del eje volcánico de México. *Geofísica Internacional*, 25, 503-520.

Dreger D.S., 2003, TDMT_INV: Time Domain Seismic Moment Tensor INVersion, *International Handbook of Earthquake and Engineering Seismogy*, 81B, 1627.

García D., Singh S.K., Herráiz H., Pacheco J.F., Ordaz M., 2004, Inslab earthquakes of central Mexico: Q, source spectra and stress drop. *Bull. Seism. Soc. Am.,* 94, 789-802.

García Acosta V., Suárez Reynoso G., 1996, Los sismos en la historia de México, tomo I. FCE, UNAM, CIESAS, Mexico City, 718 pp.

Havskov J., Ottemöller L., 1999, Electronic seismologist: SeisAn earthquake analysis software. *Seism. Res. Lett.,* 70, 532-534.

Herrmann R.B., 1985, An extension of random vibration theory estimates of strong ground motion at large distances. *Bull. Seism. Soc. Am.,* 75, 1447-1453.

Johnson C.A., Harrison C.G.A., 1990, Neotectonics in Central Mexico. *Phys. Earth Planet. Int.*, 64, 187-210.

Lienart B.R., Havskov J., A computer program for locating earthquakes both locally and globally, *Seism. Res. Lett.*, *66*, 26-36, 1995.

Michaud F., Bourgois J., Parrot J.F., Taud H., Kasser M., 1994, Le point triple de Jalisco (Mexique): évolution tectonique á partir du traitement do données MNT-SPOT. *C. R. Acad. Sci. Paris*, 318, 1117-1124.

Moore G., Marone C., Carmichael I.S.E., Renne P., 1994, Basaltic volcanism and extension near the intersection of the Sierra Madre

volcanic province and the Mexican Volcanic Belt.*Geol. Soc. Am. Bull.*, 106, 383-394.

Ordaz M., Singh S.K., 1992, Source spectra and spectral attenuation of seismic waves from Mexican earthquakes, and evidence of amplification in the hill zone of Mexico City. *Bull. Seism. Soc.Am.*, 82, 24-43.

Ordaz M., Arboleda J., Singh S.K., 1995, A scheme of random summation of an empirical Green´s function to estimate ground motions from future large earthquakes. *Bull. Seism. Soc. Am.*, 85, 1635-1647.

Ordoñez E., 1912, The recent Guadalajara earthquakes. *Bull. Seism. Soc. Am.*, 2, 134-137.

Ortega R., Quintanar L., 2005, A study of local magnitude scale in the Basin of Mexico: Mutually consistent estimate of logA0 and ground motion scaling. *Bull. Seism. Soc. Am.*, 95, 605–613.

Ortega R., Herrmann R.B., Quintanar L., 2003, Earthquake groundmotion scaling in central Mexico, *Bull. Seism. Soc. Am.*, 93, 397–413.

Ottemöller L., Shapiro N.M., Singh S.K., Pacheco J.F., 2002, Lateral variation of Lg wave propagation in southern Mexico. *J. Geophys. Res.*, 107 (B1), doi: 10.1029/2001JB000206

Pacheco J.F., Mortera C., Delgado H., Singh S.K., Valenzuela R.W., Shapiro N.M., Santoyo M.A., Hurtado A., Barrón R., Gutiérrez E., 1999, Tectonic significance of an earthquake sequence in the Zacoalco half-graben, Jalisco, Mexico. *J. South American Earth Sciences*, 12, 557-565.

Pasquaré G., Vezzoli L., Zanchi A., 1987, Morphological and structural model of Mexican Volcanic Belt, *Geofísica Internacional*, 26, 159-176.

Shapiro N.M., Singh S.K., Iglesias-Mendoza A., Cruz-Atienza V.M., Pacheco J.F., 2000, Evidence of low Q below Popocateptl volcano and its implications to seismic hazard in México City, *Geophys. Res. Lett.*, 27, 2753–2756.

Singh S.K., Apsel R., Fried J., Brune J.N., 1982, Spectral attenuation of SH-wave along the Imperial fault. *Bull. Seism. Soc. Am.*, 72, 2003-2016.

Singh S.K., Ordaz M., Pacheco J.F., Courboulex F., 2000, A simple source inversion scheme for displacement seismograms recorded at short distances. *J. Seismology*, 4, 267-284, 2000.

Singh S.K., Iglesias A., García D., Pacheco J.F., Ordaz M., 2007, *Q* of *Lg* waves in the Central Mexican Volcanic Belt.*Bull. Seism. Soc. Am.*, 97, 1259-1266.

Singh S., Iglesias A., Garduño V.H., Quintanar L., Ordaz M., 2012, A source study of the October, 2007 earthquake sequence of Morelia, Mexico and ground-motion estimation from larger earthquakes in the region. *Geofísica internacional*, 51, 1, 73-86.

Suárez G., García-Acosta V., Gaulon R., 1994, Active crustal deformation in the Jalisco block, Mexico: evidence for a great historical earthquake in the 16th century. *Tectonophysics*, 234*,* 1, 117-127.

Suter M., López-Martínez M., Quintero Legorreta O., Carrillo-Martínez M., 2001, Quaternary intra-arc extension in the central Trans-Mexican Volcanic Belt. *GSA Bulletin*, 113, 693–703.

UNAM Seismology Group, 2010, Intraslab Mexican earthquakes of 27 April 2009 (M_w5.8) and 22 May 2009 (M_w5.6): a source and ground motion study. *Geofísica Internacional*, 49, 153-163.

Urbina F., Camacho H., 1913, La zona megaseísmica Acambay-Tixmadejé. Estado de México, conmovida el 19 noviembre 1912. *Bol. Inst. Geol. Méx.*, 32, 125 pp.

Yamamoto J., Quintanar L., Herrmann R.B., Fuentes, C., 1997, Lateral variations of Lg coda Q in southern Mexico. *Pageoph*, 149, 3, 575-599.

Zúñiga F.R., Pacheco J.F., Guzmán-Speziale M., Aguirre-Dıaz G.J., Espíndola V.H., Nava E., 2003, The Sanfandila earthquake sequence of 1998, Queretaro, Mexico: activation of an undocumented fault in the northern edge of central Trans-Mexican Volcanic Belt. *Tectonophysics*, 361, 3, 229-238.

Geofísica Internacional (2017) 56-2: 187-217

Original paper

Shear Wave Splitting and Mantle Flow in Mexico: What Have we Learned?

Raúl W. Valenzuela* and Gerardo León Soto

Received: November 15, 2016; accepted: December 08, 2016; published on line: April 01, 2017

Resumen

El presente artículo es un resumen y análisis de los estudios de partición de ondas transversales (shear wave splitting) para el manto superior que se han realizado en México durante la última década. Cuando una onda sísmica entra en un medio anisótropo se parte (o se separa), esto quiere decir que se producen una onda rápida y otra lenta. Se necesitan dos parámetros para cuantificar la anisotropía. Dichos parámetros son la dirección de polarización rápida y el tiempo de retardo entre la onda rápida y la lenta. Se presenta un ejemplo de la aplicación de la técnica empleando la fase *SKS* ya que la mayoría de las observaciones usan datos telesísmicos. Sin embargo, también se incluyen los resultados de dos estudios que usaron ondas *S* locales de sismos intraplaca. Se explican aspectos importantes para interpretar las mediciones de partición. Entre ellos se incluyen la ubicación de la anisotropía en función de la profundidad, la relación entre la estructura cristalina de la olivina y el flujo del manto, el papel que juega el movimiento absoluto de placas y el papel que juegan los movimientos relativos de placas con un énfasis en las zonas de subducción. Una justificación importante para el estudio de la anisotropía sísmica es que permite conocer las características del flujo en el manto superior así como su relación con procesos tectónicos. México tiene muchos y diversos ambientes tectónicos. Algunos de ellos se encuentran actualmente activos y otros lo fueron en el pasado, pero en cualquier caso han dejado su marca en la forma de anisotropía sísmica. Esto ha dado lugar a una gran variedad de mecanismos para producir el flujo del manto. De manera general la presentación se ha organizado en las siguientes regiones: península de Baja California, la región Mexicana Occidental de Cuencas y Sierras, el norte y noreste de México, la Fosa Mesoamericana, la península de Yucatán y la anisotropía en la base del manto. La relación entre la anisotropía y el flujo del manto se analiza con base en las características particulares de cada región.

Palabras clave: partición de ondas *S,* anisotropía del manto superior, flujo del manto, movimientos de placas, Fosa Mesoamericana, placas de Cocos, Rivera, Pacífico y América del Norte.

R. W. Valenzuela*
Departamento de Sismología
Instituto de Geofísica
Universidad Nacional Autónoma de México
Ciudad Universitaria
Delegación Coyoacán, 04510
Mexico CDMX, México
**Corresponding author: raul@geofisica.unam.mx*

G. León Soto
Instituto de Investigaciones en Ciencias de la Tierra
Universidad Michoacana de San Nicolás de Hidalgo
Morelia, Mich., Mexico

Abstract

A review is presented of the shear wave splitting studies of the upper mantle carried out in Mexico during the last decade. When a seismic wave enters an anisotropic medium it splits, which means that a fast and a slow wave are produced. Two parameters are used to quantify anisotropy. These are the fast polarization direction and the delay time between the fast and the slow wave. An example of the measurement technique is presented using an *SKS* phase because most observations are based on teleseismic data. Results of two studies using local *S* waves from intraslab earthquakes are also discussed. Key aspects of the interpretation of splitting measurements are explained. These include the depth localization of anisotropy, the relationship between olivine fabrics and mantle flow, the role of absolute plate motion, and the role of relative plate motions with a special focus on subduction zones. An important motivation for studying seismic anisotropy is that it makes it possible to constrain the characteristics of upper mantle flow and its relationship to tectonic processes. Mexico has many diverse tectonic environments, some of which are currently active, or were formerly active, and have left their imprint on seismic anisotropy. This has resulted in a wide variety of mechanisms for driving mantle flow. Broadly speaking, the discussion is organized into the following regions: Baja California peninsula, Western Mexican Basin and Range, northern and northeastern Mexico, the Middle America Trench, the Yucatán peninsula, and lowermost mantle anisotropy. Depending on the unique characteristics encountered within each region, the relationship between anisotropy and mantle flow is explored..

Key words: shear wave splitting, upper mantle anisotropy, mantle flow, plate motions, Middle America Trench, Cocos, Rivera, Pacific, and North American plates.

Introduction

Seismic anisotropy is a process whereby elastic waves travel faster in a preferred direction and slower in other directions. It occurs for both *P* and *S* waves, e. g. Savage (1999) and Park and Levin (2002). Different seismic phases, analyzed with different methods, can be used to measure anisotropy. These include studies relying on the refracted *Pn* phase, tomography of both body and surface waves, shear wave splitting, surface wave scattering, and the receiver function technique; see Park and Levin (2002) and Long (2013) for a review. It is the purpose of this paper to focus on shear wave splitting and its relationship to upper mantle flow in Mexico.

When a shear wave propagates through an anisotropic medium, its component polarized parallel to the fast direction gets ahead of its orthogonal component, which is thus known as the slow wave. In this case the fast wave "splits" from the slow one. This phenomenon is the equivalent of the birefringence observed for light (electromagnetic) waves traveling at different speeds within a calcite crystal, as described in optics textbooks, e. g. Hecht (1987). Two parameters are needed to quantify shear wave splitting. These are the polarization direction of the fast wave, ϕ, an angle usually measured clockwise from north, and the delay time, δt, between the fast and the slow wave, e. g. Silver and Chan (1991). Olivine is a major component of the upper mantle and it is an anisotropic mineral (Stein and Wysession, 2003). Mantle anisotropy is the result of the strain induced lattice preferred orientation (LPO) of upper mantle minerals, predominantly olivine (Silver and Chan, 1991; Savage, 1999). As explained below, seismic anisotropy can oftentimes be used to tell the direction of mantle flow and can also be related to different tectonic processes.

Worldwide, shear wave splitting studies of the upper mantle, using teleseismic phases, were published starting in the 1980s once broadband seismometers became widely available (e. g. Ando and Ishikawa, 1982; Ando *et al.,* 1983; Ando, 1984; Kind *et al.,* 1985; Bowman and Ando, 1987; Silver and Chan, 1988, 1991; Vinnik *et al.,* 1989a, 1989b, 1992; Vinnik and Kind, 1993). The methods, as well as the results, have been extensively discussed in several excellent reviews (Silver, 1996; Savage, 1999; Park and Levin, 2002; Long and Silver, 2009a; Long and Becker, 2010). Given that subduction zones play a dominant role as drivers of plate tectonics, their anisotropy structure has been extensively studied (e. g. Long and Silver, 2008, 2009b; Long, 2013; Long and Wirth, 2013; Lynner and Long, 2014a, 2014b; Paczkowski *et al.,* 2014a, 2014b). Shear wave splitting results have been compiled in excellent databases by Liu (2009) for North America, and by Wüstefeld *et al.* (2009) worldwide.

Many studies in Mexico have used teleseismic, core-transmitted phases such as *SKS.* In the earliest work, Barruol and Hoffmann (1999) made a few measurements of shear wave splitting parameters at UNM, the only Geoscope station in Mexico. Later on, van Benthem (2005) made an attempt to present a unified view of upper mantle anisotropy and flow for the entire country, but only a handful of stations were available then. He used data from the permanent network operated by Mexico's Servicio Sismológico Nacional, SSN (Singh *et al.,* 1997), and from the temporary NARS-Baja California deployment (Trampert *et al.,* 2003; Clayton *et al.,* 2004). Later studies were focused, for the most part, on particular regions of the country, using data mostly from temporary arrays. Research in northwestern Mexico (Obrebski *et al.,* 2006; Obrebski, 2007; van Benthem *et al.,* 2008; Long, 2010) used data from the permanent networks Red Sísmica del Noroeste de México, RESNOM (Grupo RESNOM, 2002), and Red Sísmica de Banda Ancha del Golfo de California, RESBAN (Castro *et al.,* 2011), in addition to the temporary NARS-Baja California deployment (Trampert *et al.,* 2003; Clayton *et al.,* 2004). A number of dense, temporary arrays have been used to study subduction of the oceanic Cocos (MASE, 2007; Pérez-Campos *et al.,* 2008; VEOX, 2010; Melgar and Pérez-Campos, 2011; Kim *et al.,* 2011) and Rivera (Yang *et al.,* 2009) plates beneath the continental North American plate. The data from these experiments have been used subsequently to make upper mantle shear wave splitting measurements (Stubailo and Davis, 2007, 2012a, 2012b, 2015; Bernal-Díaz *et al.,* 2008; León Soto *et al.,* 2009; Rojo-Garibaldi, 2011; Bernal-López, 2015; Stubailo, 2015; Bernal-López *et al.,* 2016) and have been helpful to constrain the subslab mantle flow. Additionally, Lynner and Long (2014a) carried out source-side splitting measurements of subslab anisotropy using teleseismic *S* waves after accounting for anisotropy beneath the stations. León Soto and Valenzuela (2013) used *S* phases from local, intraslab earthquakes deeper than 50 km recorded by the VEOX experiment in order to measure anisotropy in the mantle wedge. Recent work has quantified anisotropy using *SKS* data from new SSN stations (Ponce-Cortés, 2012; van Benthem *et al.,* 2013). It is now over a decade since the first results of shear wave splitting in the upper mantle in Mexico were published. It is the purpose of this paper to present a coherent picture of mantle flow for the country. This is appropriate because of the growth the permanent SSN network has experienced (Valdés-González *et al.,* 2005, 2012). Furthermore, the use of permanent and temporary networks together provides a thorough picture, both geographically and in time. Permanent networks are made up of fewer stations located farther apart, but cover a larger area over a long period of time. On the other hand, temporary networks densely cover a smaller area for a few years.

Measurement of Shear Wave Splitting Parameters

Many shear wave splitting studies of the upper mantle in Mexico (van Benthem, 2005; Obrebski *et al.,* 2006; Obrebski, 2007; Stubailo and Davis, 2007, 2012a, 2012b, 2015; van Benthem *et al.,* 2008, 2013; Bernal-Díaz *et al.,* 2008; León Soto *et al.,* 2009; Long, 2009a, 2010; Rojo-Garibaldi, 2011; Ponce-Cortés, 2012; Stubailo, 2015; Bernal-López, 2015; Bernal-López *et al.,* 2016) have worked with core-transmitted phases such as *SKS, sSKS, SKKS,* and *PKS* because they offer several advantages that will be discussed shortly. Most importantly, in the isotropic case **KS* waves are radially (i. e. *SV*-) polarized and thus should not be observed on the transverse component, making it easier to verify that the measured parameters (ϕ, δt) are reliable. The technique used to quantify splitting, however, is more general and can be applied to shear waves containing both *SV* and *SH* energy from local events (e. g. León Soto *et al.,* 2009; León Soto and Valenzuela, 2013).

As mentioned above, the use of core-transmitted waves provides several advantages. (1) For a **KS* phase, the compressional wave traveling through Earth's liquid outer core (the *K* segment) produces only an upgoing *SV*-polarized wave upon entering the mantle. Consequently, in the isotropic case, the **KS* wave will be recorded on the radial component alone and will not be observed on the transverse. Seismic records showing a **KS* arrival on the transverse component are often an indicator of seismic anisotropy under the station (Figure 1a). (2) Given that *SKS* is a teleseismic arrival, its incidence angle at the station is nearly vertical (~10°). *SKS* is most useful for splitting measurements at epicentral distances between 85° and 110° and can thus be used to study anisotropy in regions of no seismic activity such as continental interiors (Silver and Chan, 1988). (3) Since the width of the first Fresnel zone for **KS* phases is on the order of 100 km (Eakin *et al.,* 2015), they provide good lateral resolution and have been used to tell differences between adjacent tectonic domains (e. g. Silver and Chan, 1988; 1991; Silver and Kaneshima, 1993; Silver, 1996; Sheehan *et al.,* 1997). Most often,

the anisotropy measured from **KS* phases is interpreted to reside in the upper mantle. Care should be taken, however, because core-transmitted phases lack depth resolution and anisotropy can thus accrue anywhere along the upgoing path through the mantle and crust beneath the station (Silver and Chan, 1991; Silver, 1996; Savage, 1999). This issue will be further discussed below.

The procedure to determine the fast polarization direction and the delay time in shear wave splitting analysis is explained in detail by Silver and Chan (1991). Therefore, in the present work, the covariance method is presented in an abridged manner and it is illustrated through an *SKS* measurement. Figure 1a shows the *SKS* wave on the radial and transverse components. Observation of *SKS* as a small, but clear arrival on the transverse component is a plausible indicator of anisotropy beneath the station. In order to measure the anisotropy parameters (ϕ, δt), a window containing the *SKS* pulse in the north-south and east-west components is cut. Subsequently, the N-S and E-W components are rotated in one degree intervals, with ϕ ranging from -90° to 90°. Additionally, for each trial value of ϕ, one component is time-shifted by a time step Δt relative to the other, and the corresponding elements of the covariance matrix are calculated. The *SKS* wave has a dominant period between 10 and 20 s. Observed values of δt usually range from 0.5 to 2.0 s. In the example of Figure 2, Δt = 0.05 s, corresponding to data recorded at 20 samples per second (sps), while trial values of δt fall between 0 and 8 s. In this example Δt = 0.05 s is considered a useful upper bound. Smaller time steps Δt can be chosen for seismograms recorded at greater sampling rates. Small time delays ($\delta t \approx$ 0.5 s) are at the resolution limit for core-transmitted waves (Silver and Chan, 1991). In our experience, however, times delays ~0.4 s have been resolved in records having a good signal-to-noise ratio. Furthermore, station-averaged splitting parameters obtained using the method of Wolfe and Silver (1998) provide increased reliability (see below). In the presence of anisotropy, for a well resolved splitting measurement, the covariance matrix will have two nonzero eigenvalues, λ_1 and λ_2 (Silver and Chan, 1991). While searching through parameter space, and considering that noise is present in the records, one has to look for the combination (ϕ, δt) which will produce the most nearly singular covariance matrix (Silver and Chan, 1991). This is usually accomplished by finding the minimum of λ_2, i. e. λ_2^{min} (Figure 2), as in Silver and Chan (1988, 1991). In this plot, the eigenvalues λ_2 obtained for all combinations of ϕ and δt are normalized by dividing by λ_2^{min}. The location of λ_2^{min} is represented by the dot at (74°, 0.95 s).

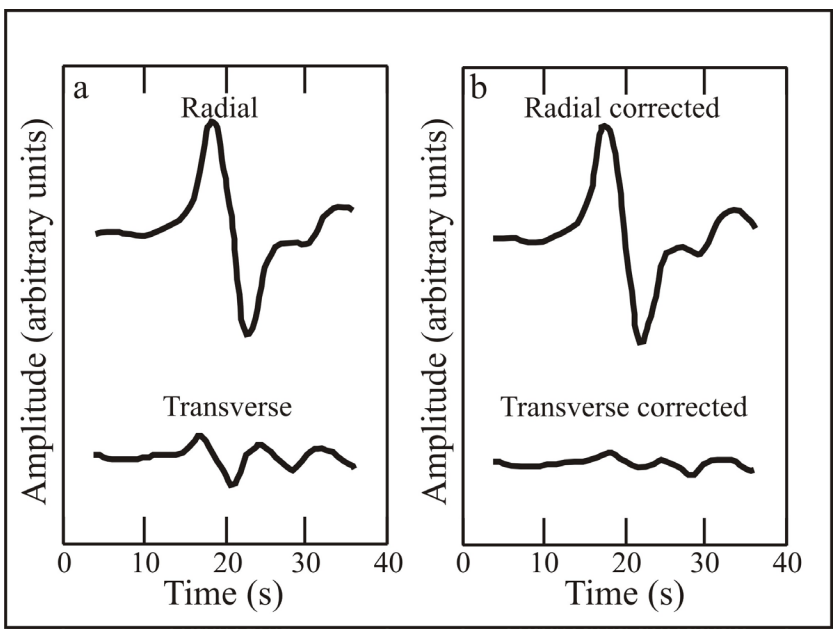

Figure 1. *SKS* wave from the April 8, 1999 event in the Japan Subduction Zone (43.60° N, 130.53° E, h=560 km, M_w = 7.2) recorded at SSN broadband station Mazatlán (MAIG). The epicentral distance is 95.37°. (a) The radial and transverse components are shown. (b) The radial and transverse components are shown after correcting for splitting using the values that were measured. Figure from van Benthem *et al.* (2008).

Other eigenvalue-based measures of linearity such as maximizing λ_1, or λ_1/λ_2, or minimizing $\lambda_1\lambda_2$, have been used by various authors, but these are all equivalent (Silver and Chan, 1991). Finding λ_2^{min} is useful to evaluate the uncertainty of the measured parameters (ϕ, δt) by applying Eq. (16) of Silver and Chan (1991). The first contour around the dot in Figure 2 defines the 95% confidence region for the measurement. In the method of Wolfe and Silver (1998), the contour plots of each individual measurement (earthquake) made at a given station are stacked in order to obtain a robust average measurement for the station having a smaller confidence region. In our experience, small time delays ($\delta t \approx 0.5$ s) are often associated with a large uncertainty in the fast polarization direction. In these cases the stacking method (Wolfe and Silver, 1998) produces well constrained station averages.

Several checks are needed to make sure that the measured splitting parameters are reliable. (1) The N-S and E-W components are rotated and time-shifted by the observed (ϕ, δt) into the fast and slow orthogonal components (Figure 3). Visual inspection of the seismograms should show that the fast and slow shear waveforms are similar, and the fast shear wave should arrive earlier by an amount approximately equal to the measured δt. The fast and slow shear waves must be similar because they originate from the same shear wave within the isotropic medium. Essentially, the covariance method works by finding the values (ϕ, δt) which result in the largest cross-correlation, i. e. similarity, between the fast and slow waves. (2) In the presence of anisotropy, particle motion is elliptically polarized (Figure 4a). Applying a correction to the original components in the amount of (ϕ,

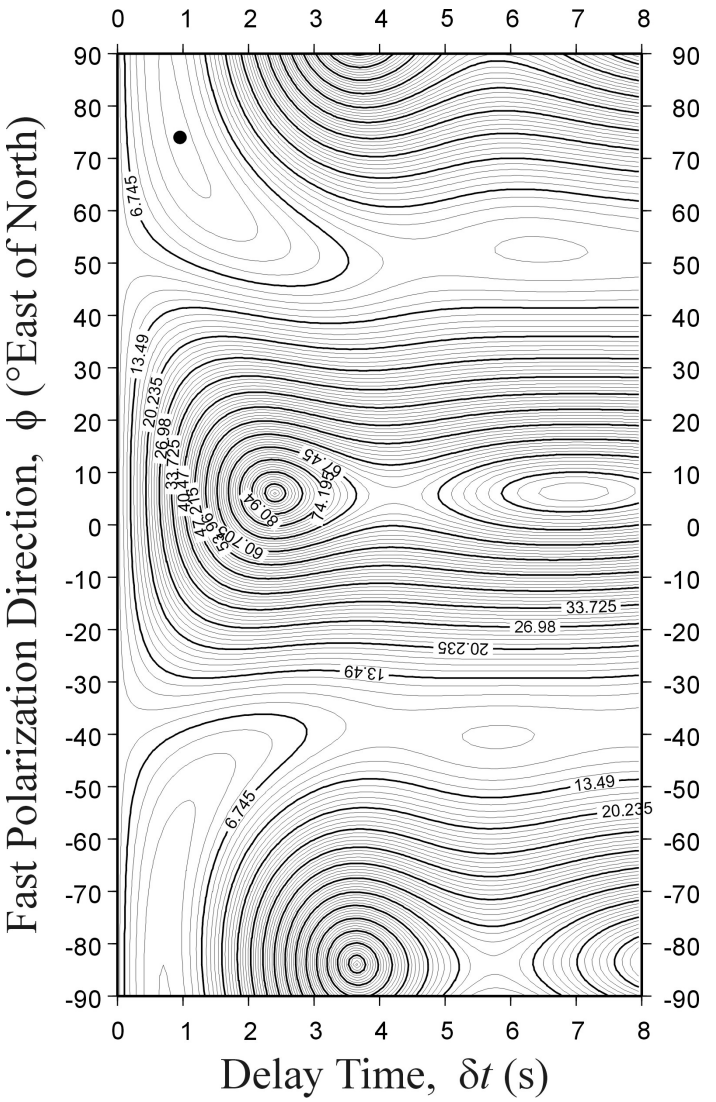

Figure 2. Contour plot showing the minimum value in (ϕ, δt)-space as indicated by the dot. In this case the fast polarization direction is N74°E and the delay time is 0.95 s. The first contour around the dot bounds the 95% confidence region. Figure from van Benthem *et al.* (2008).

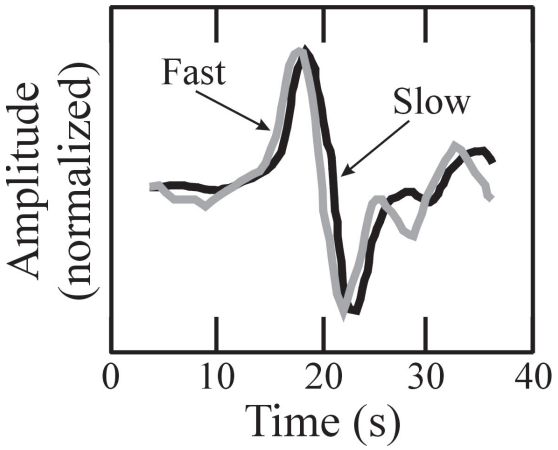

Figure 3. Once the fast polarization direction is known, the N-S and E-W horizontal records are rotated through the angle ϕ in order to obtain the slow and fast components of the *SKS* pulse. The slow and fast components are shown normalized to the same amplitude. Figure from van Benthem *et al.* (2008).

δt) removes the anisotropy, thus resulting in linear particle motion, as shown in Figure 4b for the radial and transverse components of the *SKS* example. (3) In the special case of **KS* waves, removal of the anisotropy returns the energy from the "uncorrected" transverse **KS* wave to the "corrected" radial **KS* pulse, effectively removing it from the "corrected" transverse component (Figure 1b). The amplitude of the "corrected" radial **KS* pulse is larger than the amplitude of the "uncorrected" radial **KS,* although this effect is too small to notice in Figure 1b.

Variations of the method described above have been used by different authors. In the special case of **KS* core-transmitted phases, the energy on the trial transverse component can be minimized instead of λ_2 (Silver and Chan, 1988, 1991). Additionally, given that **KS* on the transverse component in an isotropic medium is zero, and if the delay time, δt, is small compared to the characteristic period of the wave being used, then the transverse component **KS* within an anisotropic medium is approximately proportional to the time derivative of **KS* on the observed radial component (Silver and Chan, 1988, 1991; Vinnik *et al.,* 1989b). Vinnik *et al.* (1989b) take advantage of this fact and synthesize the trial transverse component **KS* waveform from the observed radial component. The parameters (ϕ, δt) are determined by minimizing the difference between the synthetic and observed transverse **KS* pulse.

Interpreting Shear Wave Splitting Measurements

In order to interpret the results of shear wave splitting measurements, it is necessary to resolve certain issues such as the actual localization of the anisotropy along the path from the core-mantle boundary to the stations, the relationship between simple shear and the direction of mantle flow depending on the various fabrics of olivine, and the relationship between tectonic processes and the anisotropy they cause. These topics are discussed in the present section.

Depth Localization of Anisotropy

Given that for **KS* phases anisotropy accrues all along the upgoing path through the mantle and crust beneath the station (Silver and Chan, 1991; Silver, 1996; Savage, 1999), it is important to determine where the main contribution to anisotropy is localized. Careful studies using stations that have data sampling from many different back azimuths, as well as comparison of splitting parameters measured from similar back azimuths at nearby stations

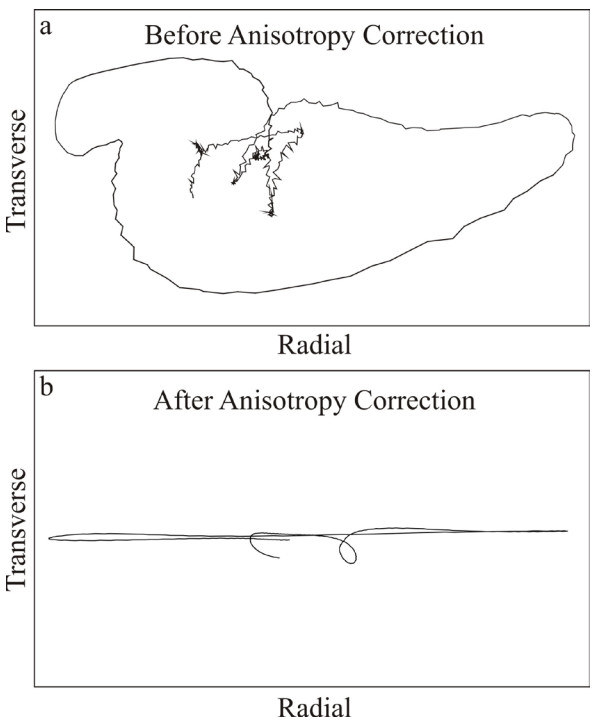

Figure 4. A further check is the comparison of the radial and transverse particle motion. (a) Before correcting for the anisotropy the particle motion is elliptical. (b) Once a correction for the measured anisotropy is applied, the particle motion becomes nearly linear. Figure from van Benthem *et al.* (2008).

(Ando *et al.,* 1983; Silver and Chan, 1988; Savage and Silver, 1993; Gao *et al.,* 1994; Alsina and Snieder, 1995; Hirn *et al.,* 1995; Guilbert *et al.,* 1996; Sheehan *et al.,* 1997; Savage, 1999), concluded that in many cases most of the observed anisotropy is found in the upper mantle, with little to no splitting below 400-600 km depth (Vinnik *et al.,* 1992, 1995, 1996; Barruol and Mainprice, 1993; Mainprice and Silver, 1993; Savage, 1999). In fact, most shear wave splitting studies base their interpretations on tectonic processes occurring in the upper mantle. In some regions, however, evidence has emerged for anisotropy in the lowermost upper mantle and in the uppermost lower mantle (Wookey *et al.,* 2002; Chen and Brudzinski, 2003; Wookey and Kendall, 2004; Foley and Long, 2011; Di Leo *et al.,* 2012; Kaneshima, 2014; Lynner and Long, 2014a), as well as in the D" layer at the base of the mantle (Long, 2009a). Additionally, the contribution from the crust must also be assessed. Shear wave splitting measurements of crustal anisotropy around the world have obtained delay times ranging mostly from 0.1 to 0.3 s, and averaging to 0.2 s (Kaneshima, 1990; Silver and Chan, 1991; Silver, 1996; Crampin and Gao, 2006). Several causes for crustal anisotropy have been proposed (e. g. Balfour *et al.,* 2005, 2012). One common explanation suggests that fluid-filled cracks align preferentially in the direction of maximum compressive stress (Crampin, 1994; Balfour *et al.,* 2005, 2012) and are located in the top 10 to 15 km of the crust (Kaneshima *et al.,* 1988; Kaneshima, 1990; Crampin, 1994; Silver, 1996). Mineral alignment associated with foliation in schist or shearing in fault zones is another possible source of anisotropy (Balfour *et al.,* 2005, 2012; Boness and Zoback, 2006). It has been suggested that in the upper crystalline crust, anisotropy may be due to cracks and produced as a result of stress, whereas in the lower crust it may be caused by mineral alignment from sheared and metamorphosed rocks (Babuska and Cara, 1991; Savage, 1999; Balfour *et al.,* 2012). If two or more anisotropic layers are present under a station, and if the fast axes of these layers are not oriented in the same direction, then it is not possible to calculate a simple, arithmetic sum of the delay times in each layer. The measured, apparent splitting parameters (ϕ_a, δt_a) can be expressed as trigonometric functions of the splitting parameters of the individual layers (ϕ_1, δt_1) and (ϕ_2, δt_2); see Savage and Silver (1993), Silver and Savage (1994), and Özalaybey and Savage (1994, 1995). Typical delay times determined from **KS* phases are on the order of 1 s, which is about five times the average crustal delay time of 0.2 s (Silver, 1996). To summarize, the crustal contribution to **KS* splitting is small, and it is generally agreed that the main contribution to the splitting parameters comes from the uppermost mantle (Silver, 1996). Furthermore, in order that the physical mechanisms explained below can give rise to anisotropy, it is necessary that anisotropy be localized in the upper mantle.

Olivine Fabrics and Mantle Flow

Observations of upper mantle xenoliths (Christensen, 1984; Nicolas and Christensen, 1987; Mainprice and Silver, 1993), together with laboratory experiments (Zhang and Karato, 1995; Jung *et al.,* 2006), have established that when flow occurs in simple shear, the *a* axis of olivine, and consequently the fast polarization direction, ϕ, becomes oriented in the direction of mantle flow (Silver, 1996; Savage, 1999; Jung *et al.,* 2006; Wiens *et al.,* 2008). The olivine fabric described in the preceding studies eventually became known as A-type. Experimental results have shown that A-type LPO fabric develops under relatively low stresses, high temperature, and low water content (Karato *et al.,* 2008). Therefore, it has traditionally been accepted that A-type olivine prevails under the continental and oceanic crust (Karato *et al.,* 2008), and it is also expected in the mantle wedge core (Kneller *et al.,* 2005; Jung *et al.,* 2006; Long and Silver, 2008). Subsequently, Jung and Karato (2001) reported on the existence of B-type fabric and showed that in this case the fast polarization direction, ϕ, is perpendicular to the direction of mantle flow. B-type olivine develops under low temperature, high water content, and high stress conditions and is often present in the mantle wedge tip (Kneller *et al.,* 2005; Jung *et al.,* 2006; Long, 2013). Later work has continued down the alphabet and has characterized C-, D- and E-type olivine (e. g., Jung and Karato, 2001; Kneller *et al.,* 2005; Jung *et al.,* 2006; Karato *et al.,* 2008). For instance, B-, C- and E-types exist under moderate to high water content conditions (Kneller *et al.,* 2005; Jung *et al.,* 2006). For the purposes of the present review, it suffices to say that C-, D-, and E-type fabrics all show seismic fast axes oriented in the direction of mantle flow (Jung *et al.,* 2006; Long, 2009b), and are thus similar to A-type olivine in this regard.

Relation of Splitting to Tectonic Processes

One important aspect of interpreting shear wave splitting measurements concerns the relationship they hold with various tectonic

processes. These can be generally divided into processes affecting sites in the stable continental interior and sites located at plate boundaries. Of the latter, subduction zones have received special attention. These relationships are explored below.

Absolute Plate Motion

Under this hypothesis, the hot spot reference frame absolute plate motion (APM) of the rigid lithosphere drags the asthenosphere underneath, driving mantle flow in the same direction as APM (Silver, 1996). This effect is strongest at the lithosphere-asthenosphere boundary and decreases with increasing depth. In this view, the asthenosphere is a shear zone that concentrates strain, decouples the lithosphere from the slowly moving mantle below and produces anisotropy (Silver, 1996). This hypothesis is also known as simple asthenospheric flow, SAF, (Silver, 1996) and predicts that observed fast polarization directions are aligned with the direction of APM. It is frequently accepted that anisotropy produced by APM is the result of an active, ongoing process (Silver, 1996). In the absence of "fossil", lithospheric anisotropy from earlier tectonic events (see below), splitting measurements in the stable plate interiors are best explained by the APM hypothesis. Predictions from SAF work reasonably well for sites in fast-moving plates such as North America (Silver and Chan, 1991), although local tectonic effects can also be important. Several experiments in the United States have shown that North American APM explains the fast axes in the stable continental interior (e. g. Fouch *et al.,* 2000; Refayee *et al.,* 2014; Hongsresawat *et al.,* 2015).

Relative Plate Motion

This hypothesis is most relevant at plate boundaries, whether they be current or ancient. It posits that tectonic processes acting at plate boundaries cause deformation of the crust which extends into the lithospheric mantle and it is also called vertically coherent deformation, or VCD (Silver and Chan, 1988, 1991; Silver, 1996). Three different types of plate boundaries exist, and these are: transcurrent, convergent, and divergent (e. g. Levin, 1986). The expected alignment of the seismic fast polarization directions depends on the type of plate boundary as follows. For strike-slip, or transcurrent, boundaries, the seismic fast polarization direction is expected to align parallel to the transcurrent structure (Silver, 1996; Savage, 1999). Collisional structures often involve oblique convergence with a significant transcurrent component in a process referred to as transpression (Vauchez and Nicolas, 1991; Silver, 1996; Savage, 1999). Therefore, a component of mantle flow occurs parallel to the strike of transpressional structures, thus leading to strike-parallel seismic fast axes (Nicolas, 1993; Silver, 1996; Savage, 1999). For divergent boundaries the fast axis should become parallel to the extension direction outside the ridge (Silver, 1996; Blackman and Kendall, 1997; Savage, 1999), but directly below the ridge it may be parallel to the ridge axis (Blackman and Kendall, 1997; Savage, 1999).

During a tectonic episode, deformation and creation of seismic anisotropy may occur at temperatures in excess of 900°C. Once the lithospheric mantle temperature drops below this threshold, anisotropy may become "fossilized" (Silver and Chan, 1988, 1991; Silver, 1996) or "frozen-in" (Vinnik *et al.,* 1992; Savage, 1999). Barring the occurrence of a more recent tectonic event, fossil or ancient anisotropy may be preserved and can be detected at present. Under stable continental cratons, anisotropy may have remained frozen since the Archean, i. e. between 2.6 and 3.8 Ga (Silver and Chan, 1991; Silver and Kaneshima, 1993; Silver, 1996; Savage, 1999).

Subduction Systems

Subduction zones represent a particular case of convergent boundaries. Oceanic lithosphere originally created at spreading centers is recycled back into the mantle in subduction zones (e. g. Levin, 1986; Stein and Wysession, 2003). Furthermore, the negative buoyancy of subducting slabs is believed to provide the main force driving plate tectonics (Stegman *et al.,* 2006). Additionally, deep earthquakes occurring within some slabs down to depths of 660 km are useful sources to sample mantle anisotropy, both locally and teleseismically (Savage, 1999; Long and Silver, 2009b; Long, 2013). So, seismic anisotropy in subduction zones has come under close scrutiny (e. g. Savage, 1999; Long and Silver, 2008, 2009b; Long, 2013; Long and Wirth, 2013; Lynner and Long, 2014a, 2014b; Paczkowski *et al.,* 2014a, 2014b). Yet, the anisotropic structure of subduction zones is complicated because it is hard to separate the different contributions from the subslab mantle, the slab itself, the mantle wedge, and the overlying plate (Savage, 1999; Long and Silver, 2008). Generally, two different processes are recognized to control upper mantle flow and anisotropy in subduction systems. These are downdip motion of the slab and trench migration (Long and Silver, 2008).

Downdip motion of the slab.- Viscous coupling between the downgoing slab and the surrounding asthenospheric mantle drives mantle flow parallel to the subduction direction (Savage, 1999; Long and Silver, 2008). Within the mantle wedge this is called *corner flow,* whereas beneath the slab it is known as *entrained flow* (Long and Silver, 2008). Under the assumption of A-type (or similar) olivine, seismic fast axes are expected to align in the direction of relative plate motion between the overriding and subducting plates, or roughly trench-perpendicular, both above and below the slab. In this case mantle flow is two-dimensional (2-D). Because of their nearly vertical incidence angles, *SKS* anisotropy measurements are only sensitive to the horizontal component of upper mantle flow.

Trench migration.- Trenches are not stable with respect to a fixed reference frame (Stegman *et al.,* 2006). Slabs move in a downdip slab-parallel direction and also in a slab-perpendicular direction (Schellart, 2004), either backward (trench retreat or slab rollback) or forward (trench advance). Slabs do not have an infinite width in the trench-parallel direction. Instead, their width is finite and ranges between 200 and 5000 km (Stegman *et al.,* 2006). Consequently, trench migration induces toroidal flow around the lateral edges of the slab within a roughly horizontal plane (Schellart, 2004; Stegman *et al.,* 2006). Slab rollback drives 3-D *return flow* of the mantle from beneath the slab, around the slab edge, and into the mantle wedge (Schellart, 2004; Stegman *et al.,* 2006). It has been further proposed that a barrier, probably at the top or the bottom of the transition zone, keeps mantle from flowing under the slab tip (Russo and Silver, 1994; Savage, 1999; Schellart, 2004; Long and Silver, 2008, 2009b). Such a barrier could be due to the increased viscosity at the upper-lower mantle boundary, or to the high pressure beneath the slab produced by the sinking slab (Schellart, 2004). It has been suggested that this barrier causes trench-parallel mantle flow, both beneath the slab (Russo and Silver, 1994; Long and Silver, 2008, 2009b) and in the mantle wedge fore-arc (Long and Silver, 2008). Additionally, a mechanism is needed to decouple the subslab mantle from the slab itself so that flow does not become entrained. It has been proposed that the asthenosphere which is in contact with the bottom of the slab experiences a large amount of shear strain, forming a thin layer which becomes entrained and which acts as a weak decoupling zone (Phipps Morgan *et al.,* 2007; Long and Silver, 2008, 2009b). This thin asthenospheric layer is subjected to shear heating during deformation, and is therefore hot and buoyant as a result of increased temperature and reduced viscosity (Long and Silver, 2009b). Since LPO is of A-type (or similar), trench-parallel flow produces trench-parallel fast polarization directions in the subslab mantle (Long and Silver, 2008, 2009b). Within the mantle wedge fore-arc, trench-parallel flow is hypothesized to lead to high mantle flow velocities, which in turn removes cool wedge material (Long and Silver, 2008). The resulting high temperatures are compatible with A-type (or similar) LPO and with trench-parallel fast axes (Long and Silver, 2008).

Thorough reviews have shown that trench-parallel fast axes are predominant in the subslab mantle and it has been suggested that trench migration is the main agent driving trench-parallel mantle flow in subduction systems (Long and Silver, 2008, 2009b; Long, 2013). The Cascadia, Greek, and Mexican subduction zones represent exceptions where mantle flow is entrained beneath the slab, producing trench-perpendicular fast polarization directions (Long and Silver, 2008, 2009b; Long, 2013). Most of the previous studies were based on *SKS* measurements of seismic anisotropy, with appropriate corrections from local events in the mantle wedge where available (Long and Silver, 2008, 2009b). Recent work obtained source-side measurements of subslab anisotropy using intraslab sources after making the appropriate corrections for anisotropy under the receiver (Lynner and Long, 2013, 2014a, 2014b). These studies found additional subduction zones with trench-perpendicular fast axes in Central America, Alaska-Aleutians, Ryukyu, western Sumatra, and northern Kurils (Lynner and Long, 2014a). Thus, Lynner and Long (2014a) concluded that subslab seismic fast axes are more common than previously believed (Long and Silver, 2008, 2009b).

Several mechanisms have been proposed to account for the differences between subduction zones where subslab fast axes are trench-parallel and those with trench-perpendicular observations. A thorough discussion of these models is outside the scope of the present review, but they will be listed. The reader is referred to the original articles, or alternatively, to the summary by Bernal-López *et al.* (2016). The first mechanism is shear heating (Long and Silver, 2008, 2009b) as described above. Song and Kawakatsu (2012) proposed that the oceanic asthenosphere has orthorhombic anisotropy, and that the dip of the slab controls the orientation of the seismic

fast axes. Numerical modeling by Paczkowski et al. (2014a, 2014b) found that long and steep slabs are consistent with trench-parallel fast axes, whereas short slabs which do not penetrate into the lower mantle should produce trench-perpendicular fast polarization directions. Lastly, Lynner and Long (2014a, 2014b) suggested that differences in slab age, with a dividing line around 95 Ma, produce different lithospheric structures, such that trench-perpendicular fast axes are associated with younger lithosphere and trench-parallel fast polarization directions are correlated with older lithosphere.

Shear Wave Splitting Observations in Mexico

Figure 5a shows the averaged splitting parameters calculated from individual **KS* measurements made at each station of the permanent SSN, RESNOM, and RESBAN, and the temporary NARS-Baja California networks. The densest coverage is found in tectonically and seismically active regions. These are the transform-extensional boundary between the North America and Pacific plates in the Gulf of California (northwestern Mexico), and subduction of the Rivera and Cocos plates under the North America and Caribbean plates at the Middle America Trench (MAT) in southern Mexico. A few SSN stations are located in northern and northeastern Mexico, and in the Yucatán peninsula in easternmost Mexico. The ensuing discussion is organized around the various tectonic regions. Figure 5b shows the locations of various geographic features in Mexico discussed in the text.

Baja California Peninsula

Station-averaged shear wave splitting measurements for the Baja California Peninsula (van Benthem, 2005; Obrebski *et al.,* 2006; Obrebski, 2007; van Benthem *et al.,* 2008; Liu, 2009; Ponce-Cortés, 2012) are summarized in Figure 6. Results can be organized into three different regions based on the observed splitting parameters and also on the geologic and tectonic history. These regions are the northern peninsula, the southern peninsula, and one single measurement at the southernmost tip of the peninsula. Furthermore, observed shear wave splitting fast axes are consistent with those obtained from Rayleigh wave tomography at periods from 80 to 100 s along the entire length of the peninsula (Zhang *et al.,* 2007, 2009; van Benthem *et al.,* 2008). Interestingly, the velocity structure determined from surface waves is also consistent with these three different regions. At periods from 50 to 80 s, slow velocities are observed under the northern peninsula and at its southenmost tip, whereas fast velocities are obtained in between (Zhang *et al.,* 2007, 2009). Zhang *et al.* (2007) interpreted the high velocities in the southern half of the peninsula as the remnants of the stalled Magdalena and Guadalupe microplates, and associated the slow velocities under the northern half to the slab window created during subduction of the Farallon plate. The splitting fast axes in the northern peninsula are generally oriented E-W and have delay times ranging from 0.70 to 2.20 s (Obrebski *et al.,* 2006; Obrebski, 2007); see Figure 6. These observations are consistent with shear wave splitting measurements across the international boundary in California (Savage and Silver, 1993; Özalaybey and Savage, 1995; Polet and Kanamori, 2002; Hongsresawat *et al.,* 2015). Savage and Silver (1993) and Özalaybey and Savage (1995) observed a pattern of E-W fast axes in California between the southern end of the subducting Gorda plate and as far south as the southern end of the state, and also in western Nevada. They explained this pattern by mantle upwelling and subsequent horizontal flow which fills the slabless window left by the subducted Farallon plate. For southwestern California, Silver and Holt (2002) proposed that differential motion between the North American plate and sinking fragments of the Farallon plate control asthenospheric flow. Obrebski *et al.* (2006) thus proposed asthenospheric flow induced by a sinking fragment of the Farallon plate as their preferred mechanism to explain the anisotropy observed under northern Baja California. Alternatively, Bohannon and Parsons (1995) suggested that a fragment of the Farallon plate may have been captured east of the former trench. Magnetotelluric measurements by Romo *et al.* (2001) are consistent with the existence of a captured fragment. Therefore, fossil anisotropy in a captured fragment of the Farallon plate is also a possible explanation for the observed anisotropy (Obrebski *et al.,* 2006).

Shear wave splitting observations in the southern half of the Baja California peninsula are indicative of little to no anisotropy (van Benthem *et al.,* 2008); see Figure 6. Several stations have short delay times between 0.50 and 0.75 s, whereas other stations produce null measurements which can be interpreted either as the absence of detectable anisotropy ($\delta t <$ 0.5 s) or the lack of data with the proper back azimuth to return a split measurement (Figure 6). The young Guadalupe and Magdalena microplates subducted under southern Baja California (Bohannon and Parsons, 1995). Subduction of the Magdalena microplate

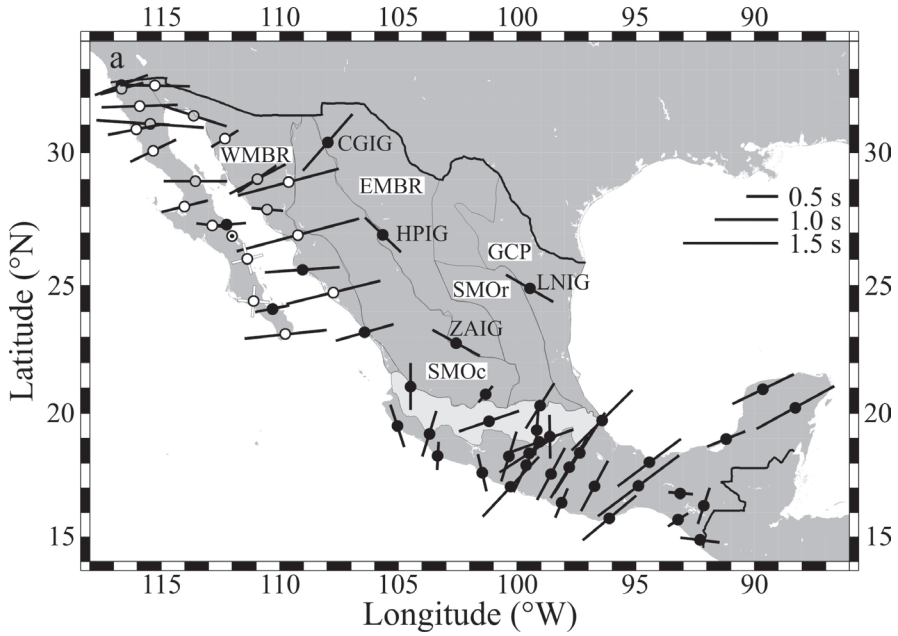

Figure 5a. Station-averaged splitting parameters in Mexico. The length of the bars is proportional to δt, as indicated in the legend. Black dots represent SSN stations (van Benthem, 2005; van Benthem *et al.,* 2008, 2013; Ponce-Cortés, 2012), gray dots are for RESNOM and RESBAN stations (Obrebski *et al.,* 2006; Obrebski, 2007), and white dots stand for the NARS-Baja California deployment (van Benthem, 2005; Obrebski *et al.,* 2006; Obrebski, 2007; van Benthem *et al.,* 2008; Liu, 2009). Thick black lines represent the international borders; with the United States to the north, and with Guatemala and Belize to the south. The TMVB is indicated by light shading. Tectonic provinces of northern Mexico are labeled: Western Mexican Basin and Range (WMBR), Sierra Madre Occidental (SMOc), Eastern Mexican Basin and Range (EMBR), Sierra Madre Oriental (SMOr), and Gulf Coastal Plain (GCP). Tectonic provinces after Ortega-Gutiérrez *et al.* (1992).

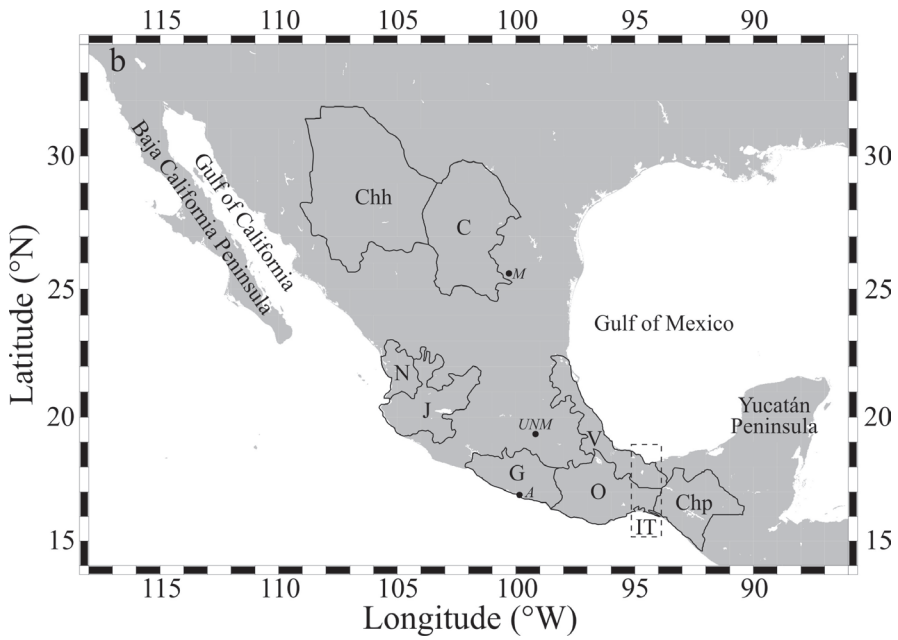

Figure 5b. Map showing geographic features in Mexico discussed in the text. Outlines represent Mexican states: Chihuahua (Chh), Coahuila (C), Nayarit (N), Jalisco (J), Veracruz (V), Guerrero (G), Oaxaca (O), and Chiapas (Chp). Dots are cities: Monterrey (*M*) and Acapulco (*A*). Location of seismic station *UNM* in Mexico City is shown. IT stands for Isthmus of Tehuantepec.

produced arc magmatism between 24 and 12.5 Ma (Sedlock *et al.,* 1993; Sedlock, 2003; Fletcher *et al.,* 2007). By 12.5 Ma, the southern Baja California peninsula was positioned over the thermal anomaly of the former Magdalena ridge, causing asthenospheric upwelling through the broken Magdalena slab (Fletcher *et al.,* 2007). Given that shear wave splitting measurements are only sensitive to horizontal flow, van Benthem *et al.* (2008) proposed vertical upwelling as the explanation for the small delay times observed. A second possibility is that shear wave splitting measurements may be influenced by fossil anisotropy (or rather, the absence of anisotropy) in the remants of the stalled Magdalena and Guadalupe microplates (van Benthem *et al.,* 2008).

A single station in the southernmost tip of the peninsula records an average delay time of 1.30 s and a fast axis oriented roughly E-W, a pattern which is most consistent with anisotropy in the northern half of the peninsula (van Benthem *et al.,* 2008); see Figure 6. In addition to the velocity and anisotropy structures determined from surface waves (Zhang *et al.,* 2007, 2009) as discussed above, the geological units on the peninsula are also consistent with the shear wave splitting observations. In the northern half, and at the southernmost tip, of the peninsula granitic rocks are exposed (Ortega-Gutiérrez *et al.,* 1992). In fact, the souterhnmost granitic unit was continuous with rocks on the mainland in Jalisco and Nayarit states before the peninsula

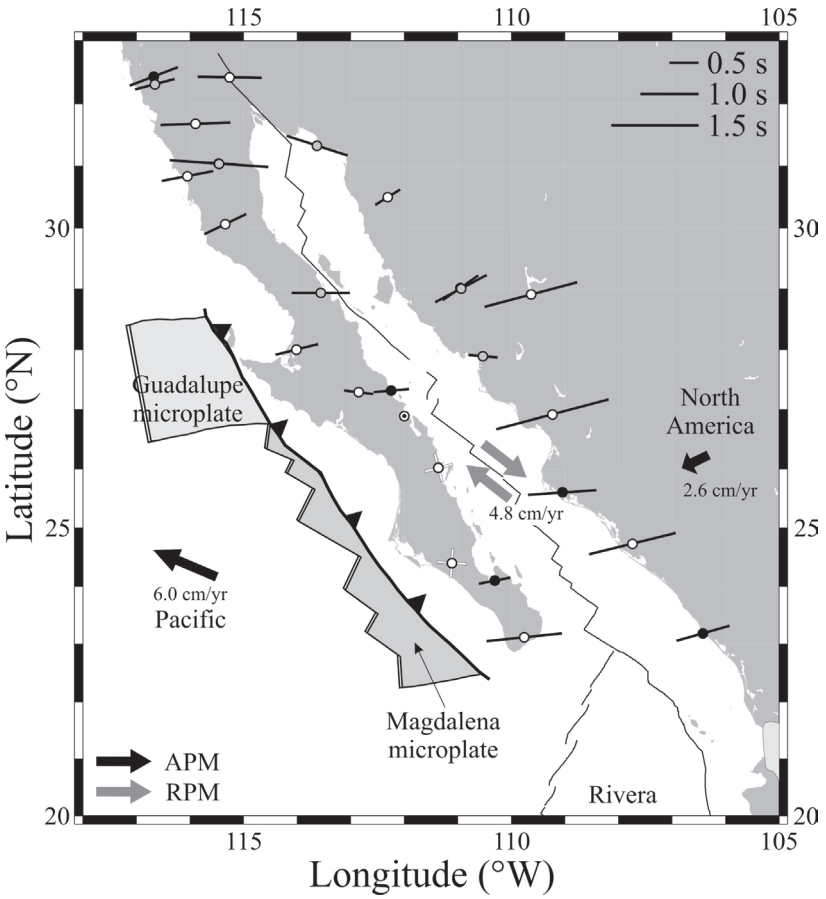

Figure 6. Station-averaged splitting parameters in northwestern Mexico. The length of the bars is proportional to δt, as indicated in the legend. Black dots represent SSN stations (van Benthem, 2005; van Benthem *et al.,* 2008; Ponce-Cortés, 2012), gray dots are for RESNOM and RESBAN stations (Obrebski *et al.,* 2006; Obrebski, 2007), and white dots stand for the NARS-Baja California deployment (van Benthem, 2005; Obrebski *et al.,* 2006; Obrebski, 2007; van Benthem *et al.,* 2008; Liu, 2009). Black arrows indicate the direction of absolute plate motion (APM) of the Pacific and North American plates (Gripp and Gordon, 2002). Gray arrows show the direction of the relative plate motion (RPM) between these two plates (DeMets *et al.,* 1994). Location of Guadalupe and Magdalena microplates relative to the Baja California peninsula at the time subduction stopped (12.3 Ma) from Fletcher *et al.* (2007). Barbed line represents the paleotrench. The Baja California peninsula, and the Guadalupe and Magdalena microplates are currently part of the Pacific plate.

rifted away (Ortega-Gutiérrez *et al.,* 1992). In between the peninsular granitic rocks, in most of the southern peninsula, igneous extrusive rocks associated to subduction of the Magdalena microplate are exposed (Ortega-Gutiérrez *et al.,* 1992; Sedlock *et al.,* 1993; Sedlock, 2003; Fletcher *et al.,* 2007). Therefore, the large delay times and E-W fast axes observed in the northern half and at the southermost tip of the peninsula record the mantle flow pattern produced by subduction of the extinct Farallon plate (van Benthem *et al.,* 2008). In between, in most of the southern half of the peninsula, subduction of the young Guadalupe and Magdalena microplates resulted in a vertical mantle flow pattern and different rock units (van Benthem *et al.,* 2008). While subduction of the Farallon and Magdalena plates occurred simultaneously, Cenozoic, extrusive volcanism only occurred associated to the young Magdalena microplate (Ortega-Gutiérrez *et al.,* 1992). This volcanism is not observed at the southernmost tip of the peninsula, in the Los Cabos and Trinidad blocks, which are distinct from the Comondú volcanics in the rest of the southern Baja California peninsula (Ortega-Gutiérrez *et al.,* 1992; Sedlock *et al.,* 1993; Fletcher *et al.,* 2007).

In addition to the work discussed above (Obrebski *et al.,* 2006; van Benthem *et al.,* 2008, O06 and B08, respectively), **KS* shear wave splitting measurements using NARS-Baja California data were made by Long (2010). While the measurements of O06 and B08 are broadly consistent with those of Long (2010) at many stations, Long (2010) identified discrepancies between the measurements made by O06 and B08 and her own measurements at several stations. Some of these differences may arise as a consequence of the different bandpass filters used. Long (2010) worked at relatively low frequencies, whereas O06 and B08 leaned towards using broader bandpass filters to the extent that the signal-to-noise ratio of the data allowed it. Also, a major focus of the work by Long (2010) was on frequency-dependent shear wave splitting. The complex splitting patterns and observed frequency dependence argue for anisotropic structure that is highly heterogeneous, and both lateral and vertical variations in anisotropy are likely (Long, 2010). While O06 and B08 recognized the complexity of the dataset, their approach was to come up with the simplest possible tectonic interpretation. Furthermore, the measurements made at permanent stations by O06 and B08 are generally supportive of their NARS-Baja California interpretations. Obrebski and Castro (2008) addressed some of the complex anisotropy questions in the crust/lithosphere working with receiver functions at selected stations of the NARS-Baja California array. In spite of the complex tectonic environment and the different filters chosen, however, the results from O06 and B08 are generally consistent with those of Long (2010). For instance, B08 agree with Long (2010) on the existence of a region of weak and/or complex anisotropy in the southern half of the peninsula. Additionally, some E-W fast axes in the northern half of the peninsula are consistent between O06 and Long (2010), and also some ENE-WSW fast axes in the Western Mexican Basin and Range (next subsection) are consistent between B08 and Long (2010). With respect to the interpretation of results, Long (2010) agrees that the Guadalupe microplate plays a role in controlling the weak anisotropy observed in the southern half of the Baja California peninsula. Unlike van Benthem *et al.* (2008), however, she proposed that coherent mantle flow is inhibited by the lodged fragments of the Guadalupe microplate. On the other hand, Wang *et al.* (2009) report on the existence of several buoyant mantle upwellings associated to some of the basins in the Gulf of California. Thus, Long (2010) proposed that the orientation of the fast axes at the three northernmost peninsular stations of the NARS-Baja California deployment is the result of horizontal flow away from the upwelling centered in the Wagner Basin.

Western Mexican Basin and Range

The Western Mexican Basin and Range (WMBR) is an extensional province bounded to the west by the Gulf of California and to the east by the Sierra Madre Occidental, or SMOc (Sedlock *et al.,* 1993). The WMBR is the southern continuation of the well-known Basin and Range province in the southwestern United States (Sedlock *et al.,* 1993). Shear wave splitting measurements in the southern WMBR show fast polarization directions consistently oriented ENE-WSW and large delay times ranging between 0.95 and 2.00 s (Obrebski *et al.,* 2006; van Benthem *et al.,* 2008); see Figure 6. In the northern WMBR delay times are generally less than 1 s and fast axes orientations are somewhat variable (Obrebski *et al.,* 2006); see Figure 6. Across the United States-Mexico border, in southwestern Arizona fast polarization directions are also oriented ENE-WSW but these gradually rotate to NE-SW as one moves towards central, northern, and eastern Arizona (Ruppert, 1992; G. Zandt, COARSE deployment, University of Arizona, unpublished data, 2004; Fouch and Gilbert, 2007; Hongsresawat *et al.,* 2015). Broadly speaking, the ENE-WSW fast axes observed in

the WMBR are aligned in the same direction as the APM of North America, which is oriented ~N254°E (Gripp and Gordon, 2002); Figure 6. Additionally, the ENE-WSW fast polarization directions are also oriented with the regional extension direction during the Miocene (Sedlock *et al.,* 1993 and references therein). In the latest Miocene, as rifting started along the axis of the modern Gulf of California, the extension direction changed to its current configuration which is roughly NW-SE (Sedlock *et al.,* 1993 and references therein). Based on the previous arguments, Obrebski *et al.* (2006) and van Benthem *et al.* (2008), proposed that both mechanisms are responsible for the observed anisotropy. The APM mechanism implies that the rigid lithosphere drags the asthenosphere beneath and aligns the olivine crystals in the upper mantle (Silver, 1996). On the other hand, fossil anisotropy would have been preserved since the Miocene in the lithosphere. Fossil anisotropy has also been proposed in the Northern Basin and Range (Great Basin of Nevada) as a consequence of extension, even as present-day extension is occurring in a different direction (Savage *et al.,* 1990). These two explanations for the observed anisotropy are not mutually exclusive, and in fact suggest that anisotropy is coherent in the lithosphere and the asthenosphere. Long (2010) also studied anisotropy in the WMBR. She proposed that anisotropy in two of her NARS-Baja California stations is controlled by the APM of North America, which is consistent with O06 and B08. In their work, however, O06 and B08 had access to permanent stations which were not available to Long (2010). Therefore O06 and B08 proposed that the APM mechanism acts over a larger area. In the paper by Long (2010), null measurements in the northernmost NARS WMBR station is explained as a local effect which is dominant over the APM. Long (2010) suggested that under this station mantle flow is vertical as a consequence of an upwelling center in the Delfín Basin as documented by Wang *et al.* (2009).

Northern and Northeastern Mexico

Seismic stations in northern Mexico are sparse. Figure 5a shows the available **KS* measurements. CGIG is the northernmost station within this region. Its fast polarization direction runs NE-SW (Ponce-Cortés, 2012). This direction stands in contrast with the ENE-WSW fast axes of stations in the WMBR located to the south and southwest (Figure 5a). It is also different from the roughly NW-SE fast axes of stations HPIG and ZAIG located to the south-southeast (Figure 5a). Station CGIG is located south of New Mexico state across the Mexican border with the United States. Shear wave splitting measurements using data from the USArray Transportable Array (TA) in southwestern New Mexico show fast polarization directions oriented NE-SW to NNE-SSW (Refayee *et al.,* 2014; Hongsresawat *et al.,* 2015) and seem to be broadly consistent with the fast axis at CGIG. Refayee *et al.* (2014) proposed that anisotropy in western New Mexico and southern and eastern Texas is controlled by the edge of the North American craton. As the lithospheric continental root moves southwest, it drives asthenospheric flow around the western edge of the craton, then around the southern edge, and finally around the southeastern edge (Figure 9 in Refayee *et al.,* 2014). The southernmost edge of the North American craton is not well defined seismically due to a lack of data in Mexico, but it seems to extend under northeastern Chihuahua and northern Coahuila (Burdick *et al.,* 2012; Refayee *et al.,* 2014). Geologic and seismic evidence for the location of the southeastern edge of the craton seem to agree. The seismically defined edge of the craton (Refayee *et al.,* 2014) is consistent with the location of the Ouachita-Marathon orogenic belt in Arkansas and eastern and south-central Texas (Sedlock *et al.,* 1993 and references therein). The continuation of the Ouachita-Marathon system in Mexico is not clear, but it is agreed that, within the limitations of the data, it should be in northern Chihuahua and Coahuila (Sedlock *et al.,* 1993 and references therein). Given the similarities between the fast axis at CGIG and the fast axes in southwestern New Mexico, and the plausible location of the southernmost edge of the North American craton in northern Mexico, it is proposed in the present study that the orientation of the fast axis at CGIG is controlled by asthenospheric mantle flow around the edge of the craton. It is hoped that the availability of new data in the future will provide a sharper image of anisotropy in this region.

The fast polarization directions at stations HPIG, ZAIG, and LNIG in northern and northeastern Mexico are aligned WNW-ESE to NW-SE (van Benthem, 2005; Ponce-Cortés, 2012; van Benthem *et al.,* 2013) and are different from the orientation of the fast axes at all other stations in Mexico (Figure 5a). Stations HPIG and ZAIG are roughly located at the intersection of the Sierra Madre Occidental and the Eastern Mexican Basin and Range, or EMBR (Ortega-Gutiérrez *et al.,* 1992). The seismic fast axes at these two stations are oriented with the trend of the SMOc. The SMOc represents a coherent block which has not undergone significant extension

and deformation, flanked to the west by the WMBR, and to the east by the EMBR. Both the western and eastern Mexican Basin and Range are extensional domains and are the southern continuation of the Basin and Range (BR) province of the southwestern United States (Henry and Aranda-Gomez, 1992; Sedlock *et al.,* 1993). The WMBR and the EMBR are characterized by north-northwest-elongate basins and ranges, similar to the province in the United States (Henry and Aranda-Gomez, 1992). ENE-WSW extension started as early as 30 Ma and continues to the present (Henry and Aranda-Gomez, 1992). At this point a comparison will be made with the Colorado Plateau (CP) and the Basin and Range of the United States. Like the SMOc in Mexico, the CP is a region that has not been subjected to extension and deformation (Savage and Silver, 1993; Levander *et al.,* 2011) but it is surrounded by a Cenozoic extensional regime to the west and south in the BR, and to the east in the Rio Grande Rift (Savage and Sheehan, 2000 and references therein). Shear wave splitting measurements have found seismic fast axes parallel to the western and northern boundaries of the CP (Savage and Silver, 1993; Sheehan *et al.,* 1997). Savage and Silver (1993) proposed that the contrast in physical properties such as heat flow anomalies, gravity and magnetic anomalies, and crustal thickness between the plateau and the surrounding extensional regions tends to align the seismic fast axes parallel to the plateau boundary. In the present study it is suggested that the situation between the CP and adjacent BR is similar to the one observed between the SMOc and the EMBR, thus providing the same mechanism to explain boundary-parallel fast axes in Mexico. The new SSN station PDIG is located between HPIG and ZAIG and in their same tectonic environment, so an interesting test of this hypothesis will be to determine whether the fast axes are consistently oriented at all three stations. It should also be mentioned that the fast axis at CGIG is oriented differently from the fast axes at HPIG and ZAIG (Figure 5a) even as the three stations are located in a similar tectonic environment.

The fast axis at station LNIG is oriented WNW-ESE (Ponce-Cortés, 2012); see Figure 5a. The nearest shear wave splitting measurements are found across the international border with the United States and are not consistent with the direction at LNIG. Fast polarization directions in eastern Texas, near the coast of the Gulf of Mexico, are oriented roughly NE-SW to ENE-WSW (Gao *et al.,* 2008; Satsukawa *et al.,* 2010; Refayee *et al.,* 2014; Hongsresawat *et al.,* 2015) and with the APM of North America. Station LNIG is located ~40 km east of the Sierra Madre Oriental (SMOr) in a wide transition zone between the SMOr and the Gulf of Mexico Coastal Plain (Ramos-Zuñiga *et al.,* 2012). The SMOr is made up of a sequence of carbonate and clastic marine sedimentary rocks of Late Jurassic and Cretaceous ages which were complexly folded and overthrusted during the Laramide orogeny (Ramos-Zuñiga *et al.,* 2012 and references therein). In the region between Monterrey and Veracruz, Laramide shortening occurred in the Late Paleocene to Middle Eocene, i. e. from about 57 to 46 Ma (Sedlock *et al.,* 1993 and references therein). Shortening was oriented ENE-WSW to NE-SW and produced a foreland fold and thrust belt trending roughly NNW-SSE (Sedlock *et al.,* 1993 and references therein). The Gulf Coastal Plain is a thick sequence of clastic sediments of Tertiary age characterized by extensional deformation (Ramos-Zuñiga *et al.,* 2012 and references therein). The most obvious structural feature near LNIG is theSMOr. Based on the VCD model (Silver, 1996) of lithospheric deformation during orogenies, transpressional structures are expected to produce strike-parallel fast axes. Yet, the WNW-ESE fast axis at LNIG is oriented oblique (~45°) to the NNW-SSE trend of the SMOr. So, the available evidence does not suggest that the compression which created the SMOr is responsible for the fast polarization direction measured at LNIG. Maybe station LNIG is far enough away from the SMOr that other, unknown factors control its anisotropy. Hopefully, future shear wave splitting measurements at the new SSN stations MNIG and GTIG, north-northwest and south-southeast of LNIG, respectively, will shed light on this issue. These stations are also located near the SMOr.

The Mexican Middle America Trench

In the Mexican segment of the Middle America Trench, the oceanic Rivera and Cocos plates subduct under the continental North American plate (Figure 7a). The Rivera plate is located at the western end of the trench and moves at a relative velocity which increases from 1.7 cm/yr in the northwest to 2.9 cm/yr in the southeast according to model PVEL (DeMets *et al.,* 2010); see Figure 7a. It moves in the direction ~N35°E. The larger Cocos plate is located southeast of the Rivera plate and moves at a faster relative velocity. Its velocity increases from 5.1 cm/yr in the northwest to 7.3 cm/yr in the southeast in the direction ~N31°E. The Rivera slab subducts at an angle between ~50° (Pardo and Suárez, 1993, 1995) and 60-65° (Yang *et al.,* 2009) which is actually steeper than the adjacent Cocos slab. This

segment of the Cocos slab dips at ~30° (Pardo and Suárez, 1995) to ~40° (Dougherty *et al.,* 2012). Between the MAT and the coastline, the boundary between the Cocos and Rivera plates is continued by the bathymetric feature known as El Gordo Graben, which further extends on land as the N-S trending Colima rift. A gap between the Rivera and Cocos slabs was imaged tomographically at depths greater than 150 km (Yang *et al.,* 2009). Towards the east, it has been proposed (Bandy, 1992; Bandy *et al*., 2000; Dougherty *et al*., 2012) that the Cocos slab is fragmenting into a North Cocos plate and a South Cocos plate along the projection of the Orozco Fracture Zone (OFZ). The slab dip angle changes abruptly across this tear in the Cocos slab from ~40° in the west side to ~25° in the east (Dougherty *et al.,* 2012). Based on fundamental mode Rayleigh wave phase velocity dispersion measurements, Stubailo *et al.* (2012) also argue for the existence of a tear in the Cocos slab underneath the projection of the OFZ. Farther east still, a region of flat slab subduction is encountered (Pardo and Suárez, 1995; Pérez-Campos *et al.,* 2008; Husker and Davis, 2009). Dougherty and Clayton (2014) presented evidence for a possible slab tear within the subducted South Cocos plate near the abrupt eastern termination of the Trans-Mexican Volcanic Belt (TMVB). They observed an abrupt dip change from ~10° in the west side to ~25° in the east across this proposed tear in the slab. Other researchers established earlier that the slab dips at ~25° on the eastern side (Pardo and Suárez, 1995; Rodríguez-Pérez, 2007; Melgar and Pérez-Campos, 2011; Kim *et al.,* 2011). Based on a receiver function study and on isodepth seismicity patterns, Rodríguez-Domínguez (2016) proposed that the rupture may possibly be at an early stage of development. Fasola *et al.* (2016) argue that the slab is not torn in the updip region. They propose instead that the transition from flat to steeper subduction occurs rapidly via a sharp flexure. Going farther east still, the Tehuantepec Ridge (TR) intersects the MAT. The TR has long been recognized as a sharp contrast in the properties of the Cocos plate. The oceanic crust of the Guatemala Basin in the southeast is older and deeper than the region northwest of the TR; see Manea *et al.* (2005) for a review. The Tehuantepec Ridge is extended onshore under the North American plate (Manea and Manea, 2008). By the time the Cocos slab reaches the Mexico-Guatemala border it subducts even more steeply at 45° (Rodríguez-Pérez, 2007).

Most studies of upper mantle anisotropy in the MAT have involved teleseismic, core-transmitted **KS* phases recorded by stations in Mexico as reviewed below. These have shown predominantly trench-perpendicular fast polarization directions, which are often interpreted as the result of subslab entrained flow. The source-side splitting study by Lynner and Long (2014a) stands out because they used teleseismically recorded *S* waves from intraslab earthquakes in Mexico in order to sample subslab anisotropy in Mexico. One advantage of the method is the use of events at epicentral distances between 40 and 80°, thus increasing the number of events that can be used for shear wave splitting measurements (relative to studies limited to the use of core-transmitted **KS* phases at distances greater than 85°). It is necessary to account for anisotropy beneath the station. Corrections are obtained from previous **KS* measurements at the stations. It is best to use stations where no anisotropy has been detected, or else stations that show a simple pattern that can be characterized by a single anisotropic layer (Lynner and Long, 2014a). Another advantage of the method, compared to **KS* studies, is that subslab anisotropy can be quantified without the need to account for anisotropy in the mantle wedge and the overriding plate (Lynner and Long, 2014a). Lynner and Long (2014a) applied the source-side splitting technique to subduction in Central America, including Mexico. They obtained plate motion-parallel (i. e. approximately trench-perpendicular) fast polarization directions along the entire length of the MAT. For the specific case of Mexico, their results of subslab anisotropy are consistent with the **KS* studies to be reviewed in here.

Teleseismic shear wave splitting measurements in the Rivera segment of the MAT are shown in Figures 7b and 8. Under the Rivera slab (area between the western and central polygons in Figure 8), the fast axes are oriented in the direction of relative plate motion between the Rivera and North American plates (i. e., trench-perpendicular) and are thus interpreted to result from both subslab entrained flow and from corner flow in the mantle wedge (León Soto *et al.,* 2009). The fast axes of the three stations in the western polygon (Figure 8) are oriented in a semi-circular pattern around the western edge of the Rivera slab. These orientations are clearly different from those in the adjacent stations to the east. León Soto *et al.* (2009) proposed that this pattern shows slab rollback driving mantle flow around the slab edge from beneath the slab into the mantle wedge. The central polygon (Figure 8) shows yet a different pattern of fast polarization directions for stations within the Colima rift. León-Soto *et al.* (2009) pointed out that the pattern is

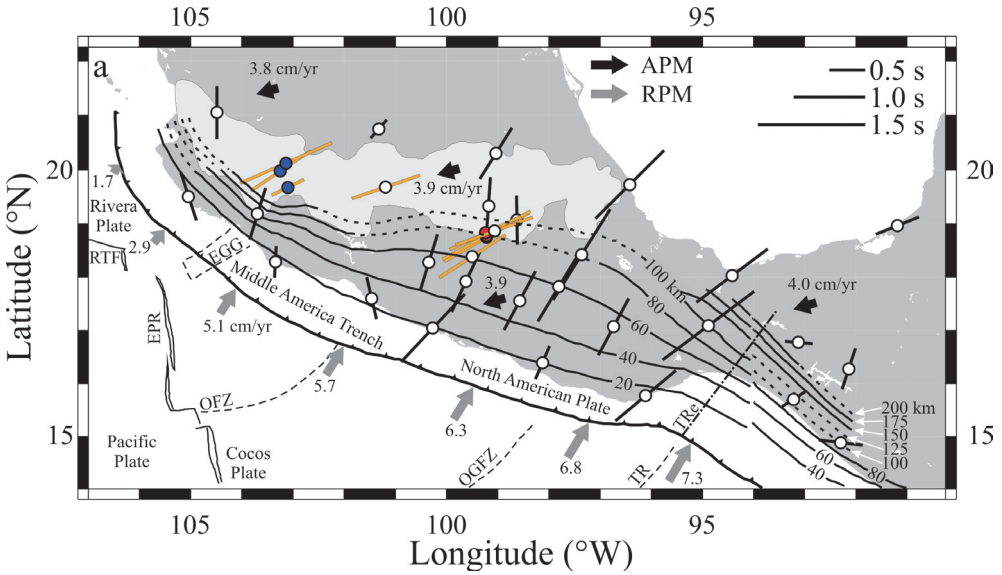

Figure 7a. Station-averaged splitting parameters in southern Mexico. The length of the bars is proportional to δt, as indicated in the legend. White dots represent SSN permanent stations (van Benthem, 2005; Ponce-Cortés, 2012; van Benthem *et al.,* 2013). (a) Blue dots are for MARS stations (León Soto *et al.,* 2009) and red dots stand for the MASE array (Rojo-Garibaldi, 2011; Bernal-López, 2015; Bernal-López *et al.,* 2016). Orange bars indicate stations where the fast polarization direction is oriented with the APM of North America. Black arrows indicate the direction of absolute plate motion (APM) for North America (Gripp and Gordon, 2002). Gray arrows show the direction of the relative plate motion (RPM) of both the Rivera and Cocos plates with respect to North America (DeMets *et al.,* 2010). RPM velocities are given in cm/yr. The Middle America Trench is represented by the line with small triangles. The Trans-Mexican Volcanic Belt (TMVB) is indicated by the light shading. Solid lines represent the isodepth contours of hypocenters within the subducting Rivera and Cocos plates. Lines are dashed where no hypocenters were available. Contours west of 94°W are from Pardo and Suárez (1995) while contours east of 94°W are from Rodríguez-Pérez (2007). In all cases, contours deeper than 100 km are from Rodríguez-Pérez (2007). Also shown are the Rivera Transform Fault (RTF), East Pacific Rise (EPR), El Gordo Graben (EGG), Orozco Fracture Zone (OFZ), O'Gorman Fracture Zone (OGFZ), and Tehuantepec Ridge (TR). TRe represents the extension of the Tehuantepec Ridge as subducted under the North American plate, from Manea and Manea (2008).

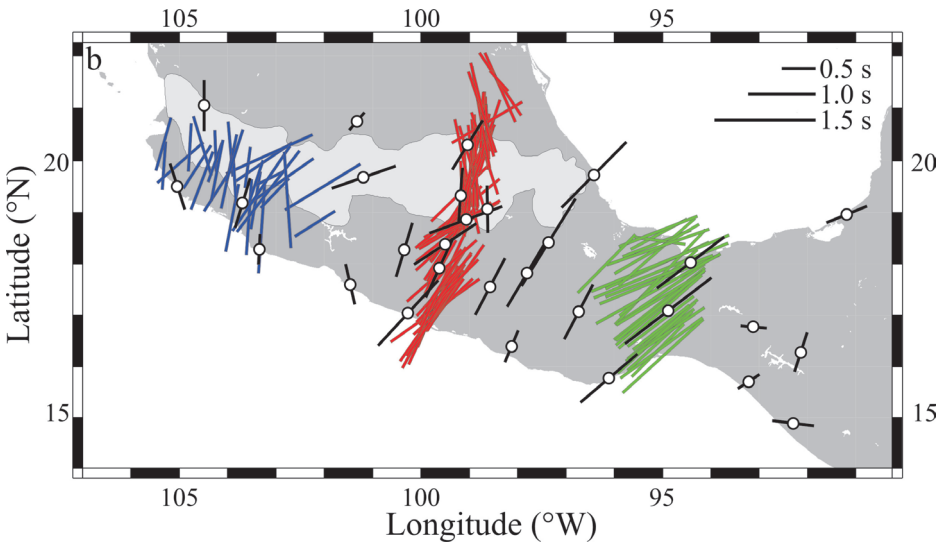

Figure 7b. (b) Same data as Figure 7a, but data from the following temporary arrays were added: blue bars represent MARS stations (León Soto *et al.,* 2009), red bars are for MASE stations (Rojo-Garibaldi, 2011; Bernal-López, 2015; Bernal-López *et al.,* 2016), and green bars stand for the VEOX deployment (Bernal-Díaz *et al.,* 2008; G. León Soto and R. W. Valenzuela, manuscript in preparation, 2017). No dots were plotted to avoid crowding the figure.

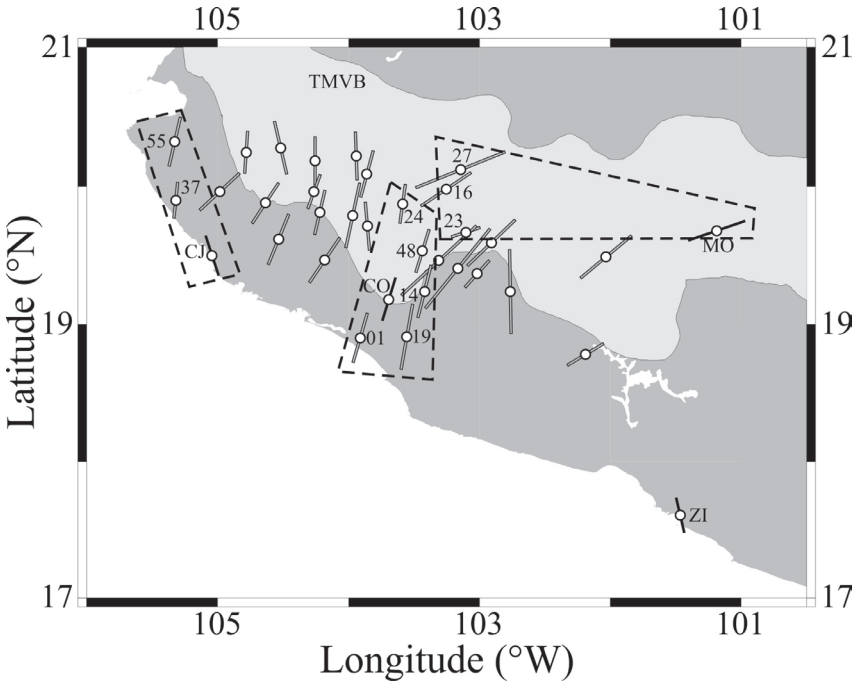

Figure 8. Station-averaged splitting parameters in the Rivera segment of the MAT. Filled bars represent SSN stations (van Benthem, 2005; León Soto *et al.,* 2009; van Benthem *et al.,* 2013) and empty bars stand for MARS stations (León Soto *et al.,* 2009). The stations enclosed by dashed-line polygons are discussed in the main text. MARS station codes were shortened by dropping the MA- prefix. The -IG suffix was dropped from SSN stations. Figure from van Benthem *et al.* (2013).

consistent with mantle flow through the slab gap between the Rivera and Cocos plates, and perhaps controls the location of Colima volcano within the rift (Yang *et al.,* 2009). Ferrari *et al.* (2001) documented rollback of the Rivera plate based on the trenchward migration of the volcanic front and further proposed asthenospheric infiltration into the mantle wedge from both the western and eastern edges of the subducted Rivera slab. Recent results of laboratory, analog models reveal complex patterns of toroidal flow between the Rivera and Cocos slabs (Neumann *et al.,* 2016) which agree with the anisotropy observations of León-Soto *et al.* (2009). In addition to using teleseismic data, León-Soto *et al.* (2009) also made shear wave splitting measurements with the MARS dataset using local, intraslab earthquakes in the depth range between 60 and 105 km as their sources. The paths from these hypocenters only sample the slab itself, the mantle wedge, and the continental crust, thus avoiding the subslab mantle altogether. They concluded that their results likely reflected anisotropy in the continental crust, with little contribution from the mantle wedge.

One single station is located where the subducted Orozco Fracture Zone meets the continent and where the tear between the North and South Cocos slabs has been proposed (station at the coastline at 101.5°W longitude in Figure 7a). The fast polarization direction at this station is clearly different from the fast axes to the east where the Cocos slab subducts subhorizontally (van Benthem, 2005; van Benthem *et al.,* 2013). Stubailo *et al.* (2012) interpreted the anisotropy patterns in their Rayleigh wave data in terms of toroidal mantle flow around the slab edges driven by slab rollback (Ferrari, 2004). The **KS* orientation of the fast axis at this single station shows that the direction of mantle flow is different from that at stations farther east and may be compatible with flow through the North Cocos-South Cocos slab gap. However, measurements from new, additional stations in this region are required in order to confirm this observation.

In the segment of the MAT between 96 and 101°W longitude the Cocos slab subducts subhorizontally (Pardo and Suárez, 1995;

Pérez-Campos *et al.,* 2008; Husker and Davis, 2009). In the fore-arc (i. e., the region between the shoreline and the TMVB) the fast polarization directions are oriented NE-SW, which is convergence-parallel, or trench-perpendicular. SSN stations afford good coverage of the area (van Benthem, 2005; Ponce-Cortés, 2012; van Benthem *et al.,* 2013); see Figure 7a. Additionally, this was the site of the dense MASE profile which ran north from Acapulco, through the TMVB, and farther north nearing the Gulf of Mexico (Stubailo and Davis, 2007, 2012a, 2012b, 2015; Rojo-Garibaldi, 2011; Bernal-López, 2015; Stubailo, 2015; Bernal-López *et al.,* 2016); see Figure 7b. Given the flat geometry of the slab, splitting measurements sample the subslab mantle flow. Physical conditions beneath the slab are expected to be low stress, low water content, and relatively high temperature, and so A-type olivine is predicted (Jung *et al.,* 2006; Long and Silver, 2008). Therefore, entrained subslab mantle flow and strong coupling between the slab and the subslab mantle are inferred (van Benthem *et al.,* 2013; Bernal-López *et al.,* 2016). The modern, active volcanic arc is located at the southern end of the TMVB (Macías, 2005). Under the TMVB the Cocos slab steepens abruptly and dips at ~75°, reaching a maximum depth of ~500 km (Pérez-Campos *et al.,* 2008; Husker and Davis, 2009; Kim *et al.,* 2010). Additionally, the TMVB is not subparallel to the offshore trench (Gill, 1981; Suarez and Singh, 1986; Ferrari *et al.*, 2012). In the back-arc (i. e., the region north of the TMVB and the northern TMVB) the seismic fast axes change orientation and align N-S, which is perpendicular to the strike of the steeply dipping slab (Rojo-Garibaldi, 2011; Ponce-Cortés, 2012; Bernal-López, 2015; Bernal-López *et al.,* 2016); see Figure 7b. This is true for the northern half of the MASE array and two nearby SSN stations. B-type olivine is frequently observed in the mantle wedge tip worldwide (Kneller *et al.,* 2005; Jung *et al.,* 2006; Long, 2013). In this particular segment of the Mexican subduction zone, however, high temperatures, in excess of 900°C, exist throughout the mantle wedge and dehydration of the slab occurs down to depths of 150 km (Manea and Manea, 2011). Therefore, Bernal-López *et al.* (2016) inferred that C-type olivine is present in the wedge tip. Physical conditions in the mantle wedge core usually are low stress, low water content, and relatively high temperature and so the existence of A-type olivine is expected (Kneller *et al.,* 2005; Jung *et al.,* 2006; Long and Silver, 2008). For both A- and C-type olivine, the fast axes align in the direction of mantle flow. Bernal-López *et al.* (2016) concluded that the N-S axes result from slab strike-perpendicular, 2-D corner flow in the mantle wedge, and also that the downgoing slab and the mantle around it are strongly coupled.

Stubailo (2015) also made shear wave splitting measurements using *SKS* and *SKKS* phases recorded by the MASE array. His results will be discussed here. For this purpose, it should be mentioned that the MASE splitting results in Figure 7b showing NE-SW fast axes in the fore-arc, and N-S axes in the back-arc were made from *SKS* phases only (Figure 5a in Bernal-López *et al.,* 2016). Measurements that only use *SKKS* phases do not show the N-S fast axes in the back-arc (Figure 5b in Bernal-López *et al.,* 2016). Instead, their *SKKS*-only measurements are consistently oriented NE-SW all along the array. The reasons for this discrepancy are discussed at length by Bernal-López *et al.* (2016). The possible causes are (1) back azimuthal dependence, perhaps an indication that two or more anisotropic layers are present under the station. (2) Differing paths to stations located at the southern and northern ends of the array, such that some rays could go through the steeply dipping slab, while others could avoid it altogether. (3) Anisotropy in the lowermost mantle as described by Long (2009a) from *SKKS* measurements at back azimuths roughly coincident with the *SKKS* observations of Bernal-López *et al.* (2016). In any case, measurements by Stubailo (2015) using both *SKS* and *SKKS* phases show fast axes mostly oriented NE-SW, in the range between N30°E and N60°E, for the entire length of the MASE array. In this regard, his results are more consistent with the *SKKS*-only measurements of Bernal-López *et al.* (2016). Stubailo (2015) stated that the NE-SW fast axes observed at the MASE array, and also at SSN stations east of MASE, are oriented in the APM direction for North America. Additionally, Stubailo *et al.* (2012), and also Stubailo (2015), made fundamental mode Rayleigh wave phase velocity dispersion measurements including anisotropy. They created a 3-D model extending down to 200 km depth. The model is made up of three layers: the continental crust, a mantle lithosphere about 50 to 60 km thick, and an asthenosphere 100 km thick. The surface wave seismic fast axes within the mantle lithosphere and the asthenosphere in the fore-arc, near the MASE stations, are oriented trench-parallel, which is inconsistent with the splitting directions. Taking into account the surface wave anisotropy pattern in the top 200 km of the Earth and the poor depth resolution afforded by shear wave splitting measurements, Stubailo (2015) proposed that the **KS* anisotropy was located deeper than

200 km. In a further step, Stubailo (2015) determined phase velocities of higher mode Rayleigh waves because overtones sample the deep structure that is poorly sampled by the fundamental mode. The higher mode phase velocity patterns, together with the sensitivity kernels, tentatively suggested that the anisotropy determined from shear wave splitting is located at depths of 200 to 400 km. The 200-400 km depth likely corresponds to the bottom of the asthenosphere, and it may be affected by the plate motion, explaining why the fast shear wave splitting direction is aligned with the plate motion of North America (Stubailo, 2015).

Between 94 and 96°W longitude, the teleseismic fast polarization directions show a slight clockwise rotation of ~25° relative to stations located over the subhorizontal slab to the west. Figure 7a shows measurements at three SSN stations (van Benthem, 2005; Ponce-Cortés, 2012; van Benthem *et al.,* 2013). Additional **KS* measurements from the VEOX array confirm the orientation of the fast axes (Bernal-Díaz *et al.,* 2008; Valenzuela-Wong *et al.,* 2015; G. León Soto and R. W. Valenzuela, manuscript in preparation, 2017); see Figure 7b. In addition to the possible tear in the slab and the change from flat to steeper subduction (Dougherty and Clayton, 2014) which were discussed above, other changes in subduction zone morphology take place here. (1) The MAT makes a bend around 96°W longitude and becomes oriented NW-SE. (2) The Tehuantepec Ridge intersects the MAT (Manea *et al.,* 2005) as previously discussed. (3) The coastline is farther away from the MAT than in the area located to the west, which implies the existence of a broad continental shelf. This is also the site where the enigmatic Yucatán slab was imaged in VEOX receiver functions (Kim *et al.,* 2011, 2014). It has been suggested that the Yucatán slab is a southwest-dipping structure opposing, and in fact cutting through, the long-recognized northeast-dipping Cocos slab (Kim *et al.,* 2011). In spite of the change in the **KS* fast polarization directions, these are still reasonably close to trench-perpendicular and are indicative of subslab entrained flow. The rotation of the fast polarization directions may be caused by the change in dip of the slab, the bend in the MAT, or perhaps by flow between the two edges of the (possibly) torn slab. Definitive settlement of this question may have to await for measurements from new stations in the area. It should also be noted that the orientation of the teleseismic fast axes shows a progressive clockwise rotation from the area of flat subduction to the west, to this area of steeper subduction, and finally to the Yucatán peninsula farther east (Figure 5a). The study by León Soto and Valenzuela (2013) also relied on VEOX data in the Isthmus of Tehuantepec. They made shear wave splitting measurements using *S* waves from deep, local intraslab earthquakes to constrain the characteristics of flow in the mantle wedge. They found that the orientations of the fast polarization directions can be divided into two regions, separated by the 100 km isodepth contour of the Cocos slab. The region southwest of the 100-km contour does not show a coherent pattern in the fast polarization directions. Given that for the shallower events the source-to-station paths through the mantle wedge are short, the anisotropy pattern may reflect a significant contribution from the overlying continental crust (León Soto and Valenzuela, 2013). To the northeast of the 100-km contour, the fast polarization directions are oriented on average N35°E and are trench-perpendicular. These measurements sample the mantle wedge core, where physical conditions are high temperature, low stress, and low water content and consequently the development of A-type olivine is expected. The observations are thus interpreted as 2-D corner flow driven by the downdip motion of the slab (León Soto and Valenzuela, 2013). Furthermore, the fast polarization directions obtained from local *S* waves are roughly consistent with the directions of the fast axes observed from **KS* phases as discussed above for this region. Taken together, the studies of van Benthem *et al.* (2013) and León Soto and Valenzuela (2013) are consistent with entrained flow under the Cocos slab.

The anisotropy pattern at the eastern end of the Mexican MAT is markedly different from that observed to the west and discussed above. These two regions are separated by the continuation of the Tehuantepec Ridge within the subducted Cocos plate. Between 92 and 94°W longitude, delay times are consistently small ($\delta t \leq 0.6$ s) and the fast axes are oriented in different directions, which is an indication of little anisotropy (Ponce-Cortés, 2012; van Benthem *et al.,* 2013); see Figure 7a. Given the nearly vertical incidence angles used for shear wave splitting measurements, these are only sensitive to the horizontal component of mantle flow. So, it is conceivably possible that mantle flow in this region is vertical, maybe within the mantle wedge, rather than beneath the slab. Since depth resolution of **KS* measurements is poor, however, it is hard to localize the depth of the observed anisotropy. Long and Silver (2008) proposed that in the mantle wedge, if neither 2-D corner flow nor 3-D flow driven by trench migration

is dominant, then the competing effects of the two result in an incoherent flow regime, which may be characterized by small δt values. The Yucatán slab is also inferred to exist in this region (Kim *et al.,* 2011, 2014). Receiver function images suggest that the Yucatán slab cuts off the Cocos slab and is thus expected to hinder 2-D mantle wedge flow for both systems (Kim *et al.,* 2011). Furthermore, Kim *et al.* (2011) proposed that 3-D flow should be important. Yet another possibility is that the region of little anisotropy beneath Chiapas is transitional between the trench-perpendicular fast axes underneath Guerrero and western Oaxaca, and the region of trench-parallel axes observed farther east along the MAT under Nicaragua and Costa Rica. Abt *et al.* (2009, 2010) reported trench-parallel fast polarization directions and mantle flow in both the mantle wedge and in the subslab mantle beneath Nicaragua and Costa Rica. This view, however, is complicated by the fact that Lynner and Long (2014a), using the source-side technique, found trench-perpendicular fast axes in the subslab mantle in the same segment of the MAT. In order to explain this discrepancy, Lynner and Long (2014a) proposed that the *S* raypaths in their study and the **KS* paths in the work by Abt *et al.* (2010) sample different volumes of the subslab mantle.

Stations Consistent With the Absolute Plate Motion of North America

As previously discussed, in the model of simple asthenospheric flow, the rigid lithosphere drags the asthenosphere beneath and drives mantle flow in the same direction as APM (Silver, 1996). This mechanism has been successful at explaining fast polarization directions in tectonically stable environments of the United States (e. g. Fouch *et al.,* 2000; Refayee *et al.,* 2014; Hongsresawat *et al.,* 2015). In Mexico, the case of fast polarization directions oriented with the APM of North America in the Western Mexican Basin and Range was discussed in section 4.2. A few other examples exist in Mexico. The absolute motion of the North American plate throughout southern Mexico is about 4 cm/yr and is oriented in a direction ~N254°E according to model HS3-NUVEL1A in Gripp and Gordon (2002); see Figure 7a. In easternmost Mexico, in the Yucatán peninsula, three SSN stations show fast axes oriented ENE-WSW and are aligned in the direction of North America APM (Ponce-Cortés, 2012; van Benthem *et al.,* 2013); see Figure 5a. For these stations the APM mechanism seems rather appropriate because they are located away from any modern plate boundaries (e. g., Cocos-North America or North America-Caribbean) and the MAT, and also from ancient collision zones (vertically coherent deformation).

Starting with early studies (van Benthem, 2005; van Benthem and Valenzuela, 2007; van Benthem *et al.,* 2013), seismic fast axes oriented in the direction of North America APM were found for three SSN stations inside or just south of the TMVB (orange bars and white circles in Figure 7a). Likewise, three MARS stations within the TMVB (León Soto *et al.,* 2009; van Benthem *et al.,* 2013) have their fast axes oriented in the direction of North America APM (eastern polygon in Figure 8, and orange bars and blue circles in Figure 7a). Additionally, three MASE stations at the southern end of the TMVB (Rojo-Garibaldi, 2011; Bernal-López *et al.,* 2016) have fast axes oriented in the direction of North America APM (orange bars and red circles in Figure 7a). In spite of the wide spacing in the location of these stations (their locations range from ~99 to ~103°W longitude) they share the fact that they are located within or just south of the TMVB. They also appear to be anomalous in the orientation of their fast axes when compared with most of the other nearby stations. It may be that these stations are far enough away from the MAT that they can escape the effects of subduction zone-related mantle flow and instead respond to APM. Yet, it is intriguing that most of the adjacent stations have their fast axes orientations and mantle flow controlled by subduction processes. Furthermore, while the stations are located on the North American plate, the subducted Cocos plate is found below and should have a dominant effect on asthenospheric flow.

Lowermost Mantle Anisotropy Observed With Stations in Mexico

All through the present review, *SKS* and *SKKS* measurements in Mexico have been interpreted to result from upper mantle anisotropy. The poor depth resolution of shear wave splitting measurements, however, must not be forgotten. A look at the work by Long (2009a) is instructive because she used stations in Mexico and found an anisotropic region in the lowermost mantle. So, a word of caution is warranted in order to avoid misinterpreting lower mantle anisotropy to the upper mantle. Simultaneous measurements of *SKS* and *SKKS* shear wave splitting from the same source and station usually return the same splitting parameters (ϕ, δt) because their raypaths converge in the uppermost mantle under the station. Long (2009a) identified 15 source-to-station pairs whereby the splitting parameters determined using *SKS* waves were different from

the parameters obtained from *SKKS* phases. Three stations were located in southwestern California, five belonged to the NARS-Baja California deployment in northwestern Mexico, and the last one was Geoscope station UNM (which is co-located with SSN station CUIG). The anomalous measurements were detected only for back azimuths oriented to the west and west-northwest. In most cases the *SKS* measurements returned null values, while the *SKKS* observations showed clear splitting. Given that the source-to-station paths of *SKS* and *SKKS* phases differ the most in the D" layer at the base of the mantle, Long (2009a) concluded that the anisotropy must be located there, instead of in the upper mantle. Analysis of the region sampled by the *SKKS* phases showed that anisotropy was located in a patch of D" beneath the eastern Pacific Ocean, and that it could be explained by a fragment of the Farallon slab subducted all the way down to the base of the mantle (Long, 2009a). It should also be mentioned that the anomalous *SKKS* observations are not distributed uniformly throughout the region as they are interspersed with normal *SKKS* measurements (Long, 2009a).

Conclusions

One important reason for the study of seismic anisotropy is that it provides a means to determine the direction of upper mantle flow and its relationship to tectonic processes. Mexico has a wide variety of tectonic environments. Some of them are currently active whereas others were active in the past. In either case, tectonic processes often leave a signature in the upper mantle in the form of seismic anisotropy. It is the purpose of this paper to present a review and summary of the different studies of upper mantle shear wave splitting conducted in Mexico during the last decade. Fast polarization directions in the northern half of the Baja California peninsula are oriented E-W and result from subduction of the former Farallon plate. In the southern half of the peninsula anisotropy is weak. Given that the shear wave splitting technique is only sensitive to the horizontal component of mantle flow, the observed anisotropy pattern may be consistent with vertical upwelling produced by the former Magdalena ridge. Measurements from one single station at the southernmost tip of Baja California are more consistent with anisotropy in the northern half of the peninsula and may be related to the angle of subduction of the former Farallon plate. In the Western Mexican Basin and Range the fast polarization directions are oriented ENE-WSW and are aligned with the APM of North America and also with the direction of extension during the Miocene. The origin of anisotropy may be both, current in the asthenosphere, and fossil in the lithosphere. Stations in northern Mexico are few and far between. One station in northern Chihuahua state has the fast axis oriented NE-SW and is consistent with observations across the United States border. Its anisotropy pattern seems to be controlled by asthenospheric mantle flow around the southern edge of the North American craton. A couple of stations are roughly located at the intersection of the Sierra Madre Occidental with the Eastern Mexican Basin and Range. Their fast axes are oriented NW-SE to WNW-ESE and are aligned with the trend of the SMOc. Thus, the contrast in physical properties between the underformed SMOc and the extended EMBR may orient the fast axes in the direction of the boundary between the two different tectonic provinces. The seismic fast axes for stations affected by subduction of the Rivera and Cocos plates under North America are predominantly oriented in the direction of relative plate convergence and are approximately trench-perpendicular. These are interpreted as subslab entrained flow. Also, trench-perpendicular corner flow is inferred in the mantle wedge above the Rivera plate and above the Cocos plate in eastern Oaxaca state. Flow is also interpreted to occur around the western edge of the Rivera slab and through the tear between the Rivera and Cocos slabs, consistent with the ongoing process of slab rollback. Under the fore-arc of the subhorizontal slab in Guerrero state, the NE-SW oriented fast axes are consistent with entrained subslab mantle flow. In the back-arc, north of the TMVB, the slab dips steeply and N-S fast polarization directions are consistent with slab strike-perpendicular corner flow in the mantle wedge. The fast axes of stations in the Isthmus of Tehuantepec are rotated ~25° clockwise relative to the fast axes of stations over the flat slab. Farther east, in Chiapas, the splitting parameters are indicative of weak anisotropy and may be related to disturbances in mantle flow caused by the proposed Yucatán slab. Alternatively, the fast axes there may be transitional between the trench-perpendicular fast axes beneath Guerrero and western Oaxaca, and the trench-parallel fast axes observed farther east along the MAT under Nicaragua and Costa Rica. The fast axes in the Yucatán peninsula are oriented ENE-WSW and are aligned with the APM of North America. The APM mechanism for these stations is consistent with their locations away from current plate boundaries and from former collision zones. Finally, observations in some NARS-Baja California stations and at Geoscope station UNM have been interpreted as anisotropy in

the lowermost mantle in a region beneath the eastern Pacific roughly parallel to the west coast of North America. It has been suggested that these observations can be explained by the subducted Farallon slab at that depth.

Acknowledgments

We are thankful to Karen Fischer for providing the computer code to measure the splitting parameters, and for giving a seminar that sent one of us (R. W. V.) down the long "anisotropy road"; Fernando Terán for the computer code to check the measurements; Manuel Velásquez for computer support; and Vlad Manea, Marina Manea, and Rob Clayton for discussions and suggestions. The suggestions made by Raúl Castro and Takeshi Mikumo greatly enriched the manuscript. We are grateful to the following colleagues who have collaborated with us in the anisotropy studies. They are, in rough chronological order, Jeremías Basurto, Antonio Lozada, Steven van Benthem, Raúl Castro, Mathias Obrebski, Alberto Bernal, Adriana González, Berenice R. Garibaldi, Gustavo Ponce, Iliana Olarte, and Leslie Alejandra Bernal. Mexico's Servicio Sismológico Nacional (SSN) data are available through the work of its staff, which involves station maintenance, data acquisition and distribution. We also wish to thank Centro de Investigación Científica y de Educación Superior de Ensenada for access to data from their network. We are also grateful to the many people whose foresight and hard work made the NARS-Baja California, MARS, MASE, and VEOX deployments a reality. This work was partly funded by Universidad Nacional Autónoma de México through Programa de Apoyo a Proyectos de Investigación e Innovación Tecnológica, PAPIIT grant IN112814. The contour plots and maps in this study were made using the Generic Mapping Tools (GMT) package (Wessel and Smith, 1998).

References

Abt D. L., Fischer K.M., Abers G.A., Strauch W., Protti J.M., González V., 2009, Shear wave anisotropy beneath Nicaragua and Costa Rica: Implications for flow in the mantle wedge, *Geochem. Geophys. Geosyst.,* 10, Q05S15, doi:10.1029/2009GC002375.

Abt D.L., Fischer K.M., Abers G.A., Protti M., González V., Strauch W., 2010, Constraints on upper mantle anisotropy surrounding the Cocos slab from *SK*(*K*)*S* splitting, *J. Geophys. Res.,* 115, B06316, doi:10.1029/2009JB006710.

Alsina D., Snieder R., 1995, Small-scale sublithospheric continental mantle deformation: Constraints from *SKS* splitting observations, *Geophys. J. Int.,* 123, 431-448.

Ando M., 1984, *ScS* polarization anisotropy around the Pacific Ocean, *J. Phys. Earth,* 32, 179-196.

Ando M., Ishikawa Y., 1982, Observations of shear-wave velocity polarization anisotropy beneath Honshu, Japan: Two masses with different polarizations in the upper mantle, *J. Phys. Earth,* 30, 191-199.

Ando M., Ishikawa Y., Yamazaki F., 1983, Shear wave polarization anisotropy in the upper mantle beneath Honshu, Japan, *J. Geophys. Res.,* 88, 5850-5864.

Babuska V., Cara M., 1991, *Seismic anisotropy in the Earth, Modern Approaches in Geophysics,* vol. 10. Kluwer Academic Publishers, Dordrecht, The Netherlands, 217 pp.

Balfour N.J, Savage M.K., Townend J., 2005, Stress and crustal anisotropy in Marlborough, New Zealand: Evidence for low fault strength and structure-controlled anisotropy, *Geophys. J. Int.,* 163, 1073-1086, doi: 10.1111/j.1365-246X.2005.02783.x.

Balfour N.J, Cassidy J.F., Dosso S.E., 2012, Crustal anisotropy in the forearc of the Northern Cascadia Subduction Zone, British Columbia, *Geophys. J. Int.,* 188, 165-176, doi: 10.1111/j.1365-246X.2011.05231.x.

Bandy W.L., 1992, Geological and Geophysical investigation of the Rivera-Cocos plate boundary: Implications for plate fragmentation, Ph. D. thesis, 195 pp., Texas A & M University, College Station, TX, USA.

Bandy W.L., Hilde T.W.C., Yan C.-Y., 2000, The Rivera-Cocos plate boundary: Implications for Rivera-Cocos relative motion and plate fragmentation, in *Cenozoic tectonics and volcanism of Mexico, Geol. Soc. Am. Spec. Pap.*, 334, edited by H. Delgado-Granados, G. Aguirre-Díaz and J. M. Stock, 1-28, Geological Society of America, Boulder, CO, USA.

Barruol G., Hoffmann R., 1999, Upper mantle anisotropy beneath the Geoscope stations, *J. Geophys. Res.,* 104, 10,757-10,773.

Barruol G., Mainprice D., 1993, A quantitative evaluation of the contribution of crustal rocks

to the shear wave splitting of teleseismic *SKS* measurements, *Phys. Earth Planet. Inter.,* 78, 281-300.

Bernal-Díaz A., Valenzuela-Wong R., Pérez-Campos X., Iglesias A., Clayton R.W., 2008, Anisotropía de la onda *SKS* en el manto superior debajo del arreglo VEOX, *Geos Boletín Informativo de la UGM,* 28, 2, 199-200.

Bernal-López L.A., 2015, Anisotropía sísmica y flujo del manto producidos por la placa de Cocos subducida en el sur de México, M. Sc. thesis, 65 pp., Centro de Sismología y Volcanología de Occidente, Universidad de Guadalajara, Puerto Vallarta, Jal., Mexico.

Bernal-López L.A., Garibaldi B.R., León Soto G., Valenzuela R.W., Escudero, C.R., 2016, Seismic anisotropy and mantle flow driven by the Cocos slab under southern Mexico, *Pure Appl. Geophys.,* 173, 3373-3393, doi:10.1007/s00024-015-1214-7.

Blackman D.K., Kendall J.M., 1997, Sensitivity of teleseismic body waves to mineral texture and melt in the mantle beneath a mid-ocean ridge, *Phil. Trans. R. Soc. Lond. A,* 355, 217-231.

Bohannon R.G., Parsons T., 1995, Tectonic implications of post-30 Ma Pacific and North American relative plate motions, *Geol. Soc. Am. Bull.,* 107, 937-959.

Boness N., Zoback M.D., 2006, Mapping stress and structurally-controlled crustal shear velocity anisotropy in California, *Geology,* 34, 825-828.

Bowman J.R., Ando M., 1987, Shear-wave splitting in the upper-mantle wedge above the Tonga subduction zone, *Geophys. J. R. Astron. Soc.,* 88, 25-41.

Burdick S., van der Hilst R.D., Vernon F.L., Martynov V., Cox T., Eakins J., Karasu G. H., Tylell J., Astiz L., Pavlis G.L., 2012, Model update March 2011: Upper mantle heterogeneity beneath North America from traveltime tomography with global and USArray Transportable Array data, *Seism. Res. Lett.,* 83, 23-28, doi:10.1785/gssrl.83.1.23.

Castro R.R., Perez-Vertti A., Mendez I., Mendoza A., Inzunza L., 2011, Location of moderate-sized earthquakes recorded by the NARS-Baja array in the Gulf of California region between 2002 and 2006, *Pure Appl. Geophys.,* 168, 1279-1292, doi:10.1007/s00024-010-0177-y.

Chen W.P., Brudzinski M.R., 2003, Seismic anisotropy in the mantle transition zone beneath Fiji-Tonga, *Geophys. Res. Lett.,* 30, 1682, doi:10.1029/2002GL016330.

Christensen N.I., 1984, The magnitude, symmetry and origin of upper mantle anisotropy based on fabric analyses of ultramafic tectonics, *Geophys. J. R. Astron. Soc.,* 76, 89-111.

Clayton R.W., Trampert J., Rebollar C., Ritsema J., Persaud P., Paulssen H., Pérez-Campos X., van Wettum A., Pérez-Vertti A., DiLuccio F., 2004, The NARS-Baja seismic array in the Gulf of California rift zone, *MARGINS Newsletter,* 13, 1-4.

Crampin S., 1994, The fracture criticality of crustal rocks, *Geophys. J. Int.,* 118, 428-438.

Crampin S., Gao, Y., 2006, A review of techniques for measuring shear-wave splitting above small earthquakes, *Phys. Earth Planet. Inter.,* 159, 1-14.

DeMets C., Gordon R.G., Argus D.F., Stein S., 1994, Effect of recent revisions to the geomagnetic reversal time scale on estimates of current plate motions, *Geophys. Res. Lett.,* 21, 2191-2194.

DeMets C., Gordon R.G., Argus D.F., 2010, Geologically current plate motions, *Geophys. J. Int.,* 181, 1-80.

Di Leo J.F., Wookey J., Hammond J.O.S., Kendall J.M., Kaneshima S., Inoue H., Yamashina T., Harjadi P., 2012, Mantle flow in regions of complex tectonics: Insights from Indonesia, *Geochem. Geophys. Geosyst.,* 13, Q12008, doi:10.1029/2012GC004417.

Dougherty S.L., Clayton R.W., 2014, Seismicity and structure in central Mexico: Evidence for a possible slab tear in the South Cocos plate, *J. Geophys. Res. Solid Earth,* 119, 3424-3447, doi:10.1002/2013JB010833.

Dougherty S.L., Clayton R.W., Helmberger D.V., 2012, Seismic structure in central Mexico: Implications for fragmentation of the subducted Cocos plate, *J. Geophys. Res.,* 117, B09316, doi:10.1029/2012JB009528.

Eakin C.M., Long M.D., Wagner L.S., Beck S.L., Tavera H., 2015, Upper mantle anisotropy beneath Peru from *SKS* splitting: Constraints

on flat slab dynamics and interaction with the Nazca Ridge, *Earth Planet. Sci. Lett.,* 412, 152-162, doi:10.1016/j.epsl.2014.12.015.

Fasola S., Brudzinski M.R., Ghouse N., Solada K., Sit S., Cabral-Cano E., Arciniega-Ceballos A., Kelly N., Jensen K., 2016, New perspective on the transition from flat to steeper subduction in Oaxaca, Mexico, based on seismicity, nonvolcanic tremor, and slow slip, *J. Geophys. Res. Solid Earth,* 121, 1835-1848, doi:10.1002/2015JB012709.

Ferrari L., 2004, Slab detachment control on mafic volcanic pulse and mantle heterogeneity in central Mexico, *Geology,* 32, 77-80, doi:10.1130/G19887.1.

Ferrari L., Petrone C.M., Francalanci L., 2001, Generation of oceanic-island basalt-type volcanism in the western Trans-Mexican volcanic belt by slab rollback, asthenosphere infiltration, and variable flux melting, *Geology,* 29, 507-510.

Ferrari L., Orozco-Esquivel T., Manea V., Manea M., 2012. The dynamic history of the Trans-Mexican Volcanic Belt and the Mexico subduction zone, *Tectonophysics,* 522-523, 122-149.

Fletcher J.M., Grove M., Kimbrough D., Lovera O., Gehrels G.E., 2007, Ridge-trench interactions and the Neogene tectonic evolution of the Magdalena shelf and southern Gulf of California: Insights from detrital zircon U-Pb ages from the Magdalena fan and adjacent areas, *Geol. Soc. Am. Bull.,* 119, 1313-1336.

Foley B.J., Long M.D., 2011, Upper and mid-mantle anisotropy beneath the Tonga slab, *Geophys. Res. Lett.,* 38, L02303, doi:10.1029/2010GL046021.

Fouch M.J., Gilbert H.J., 2007, Complex upper mantle seismic structure across the southern Colorado Plateau/Basin and Range I: Results from shear wave splitting analysis, *Eos Trans. AGU,* 88, 52, Fall. Meet. Suppl., Abstract S41B-0557.

Fouch M.J., Fischer K.M., Parmentier E.M., Wysession M.E., Clarke T.J., 2000, Shear wave splitting, continental keels, and patterns of mantle flow, *J. Geophys. Res.,* 105, 6255-6275.

Gao S., Davis P.M., Liu H., Slack P.D., Zorin Y. A., 1994, Seismic anisotropy and mantle flow beneath the Baikal rift zone, *Nature,* 371, 149-151.

Gao S.S., Liu K.H., Stern R.J., Keller G.R., Hogan J.P., Pulliam J., Anthony E.Y., 2008, Characteristics of mantle fabrics beneath the south-central United States: Constraints from shear-wave splitting measurements, *Geosphere,* 4, 411-417, doi:10.1130/GES00159.1.

Gill J.B., 1981, *Orogenic andesites and plate tectonics, Minerals and rocks,* 16, Springer, Berlin, Germany.

Gripp A.E., Gordon R.G., 2002, Young tracks of hotspots and current plate velocities, *Geophys. J. Int.,* 150, 321-361.

Grupo RESNOM, 2002, Estado actual de RESNOM y sismicidad de la región noroeste de México en el periodo septiembre-diciembre de 2001 (in Spanish), *Geos Boletín Informativo de la UGM,* 22, 43-48.

Guilbert J., Poupinet G., Mei J., 1996, A study of azimuthal *P* residuals and shear-wave splitting across the Kunlun range (northern Tibetan Plateau), *Phys. Earth Planet. Inter.,* 95, 167-174.

Hecht E., 1987, *Optics, 2nd edition.* Addison-Wesley Publishing Company, Reading, MA, USA, 676 pp.

Henry C.D., Aranda-Gomez J.J., 1992, The real southern Basin and Range: Mid-to late Cenozoic extension in Mexico, *Geology,* 20, 701-704.

Hirn A., Jiang M., Sapin M., Díaz J., Nercessian A., Lu Q. T., Lepine J. C., Shi D. N., Sachpazi M., Pandy M. R., Ma K., Gallart J., 1995, Seismic anisotropy as an indicator of mantle flow beneath the Himalayas and Tibet, *Nature,* 375, 571-574.

Hongsresawat S., Panning M.P., Russo R.M., Foster D.A., Monteiller V., Chevrot S., 2015, USArray shear wave splitting shows seismic anisotropy from both lithosphere and asthenosphere, *Geology,* 43, 667-670, doi:10.1130/G36610.1.

Husker A., Davis P.M., 2009, Tomography and thermal state of the Cocos plate subduction beneath Mexico City, *J. Geophys. Res.,* 114, B04306, doi:10.1029/2008JB006039.

Jung H., Karato S.-i., 2001, Water-induced fabric transitions in olivine, *Science,* 293, 1460-1463.

Jung H., Katayama I., Jiang Z., Hiraga T., Karato S., 2006, Effect of water and stress on the lattice-preferred orientation of olivine, *Tectonophysics,* 421, 1-22.

Kaneshima S., 1990, Origin of crustal anisotropy: Shear wave splitting studies in Japan, *J. Geophys. Res.,* 95, 11,121-11,133.

Kaneshima S., 2014, Upper bounds of seismic anisotropy in the Tonga slab near deep earthquake foci and in the lower mantle, *Geophys. J. Int.,* 197, 351–368, doi:10.1093/gji/ggt494.

Kaneshima S., Ando M., Kimura S., 1988, Evidence from shear-wave splitting for the restriction of seismic anisotropy to the upper crust, *Nature,* 335, 627-629.

Karato S.-i., Jung H., Katayama I., Skemer P., 2008, Geodynamic significance of seismic anisotropy of the upper mantle: New insights from laboratory studies, *Annu. Rev. Earth Planet. Sci.,* 36, 59-95, doi:10.1146/annurev.earth.36.031207.124120.

Kim Y., Clayton R.W., Jackson J.M., 2010, Geometry and seismic properties of the subducting Cocos plate in central Mexico, *J. Geophys. Res.,* 115, B06310, doi:10.1029/2009JB006942.

Kim Y., Clayton R.W., Keppie F., 2011, Evidence of a collision between the Yucatán block and Mexico in the Miocene, *Geophys. J. Int., 187,* 989-1000, doi: 10.1111/j.1365-246X.2011.05191.x.

Kim Y., Lim H., Miller M. S., Pearce F., Clayton R. W., 2014, Evidence of an upper mantle seismic anomaly opposing the Cocos slab beneath the Isthmus of Tehuantepec, Mexico, *Geochem. Geophys. Geosyst.,* 15, 3021-3034, doi:10.1002/2014GC005320.

Kind R., Kosarev G.L., Makeyeva L.I., Vinnik L.P., 1985, Observations of laterally inhomogeneous anisotropy in the continental lithosphere, *Nature,* 318, 358-361.

Kneller E.A, van Keken P.E., Karato S.-i., Park J., 2005, B-type olivine fabric in the mantle wedge: Insights from high-resolution non-Newtonian subduction zone models, *Earth Planet. Sci. Lett.,* 237, 781-797, doi:10.1016/j.epsl.2005.06.049.

León Soto G., Valenzuela R.W., 2013, Corner flow in the Isthmus of Tehuantepec, Mexico inferred from anisotropy measurements using local intraslab earthquakes, *Geophys. J. Int.,* 195, 1230-1238, doi:10.1093/gji/ggt291.

León Soto G., Ni J.F., Grand S.P., Sandvol E., Valenzuela R.W., Guzmán Speziale M., Gómez González J. M., Domínguez Reyes T., 2009, Mantle flow in the Rivera-Cocos subduction zone, *Geophys. J. Int.,* 179, 1004-1012, doi:10.1111/j.1365-246X.2009.04352.x.

Levander A., Schmandt B., Miller M.S., Liu K., Karlstrom K.E., Crow R.S., Lee C.-T. A., Humphreys E.D., 2011, Continuing Colorado plateau uplift by delamination-style convective lithospheric downwelling, *Nature,* 472, 461–465, doi:10.1038/nature10001.

Levin H.L., 1986, *Contemporary physical geology, 2nd edition.* Saunders College Publishing, Philadelphia, PA, USA, 558 pp.

Liu K.H., 2009, NA-SWS-1.1: A uniform database of teleseismic shear wave splitting measurements for North America, *Geochem. Geophys. Geosyst.,* 10, Q05011, doi:10.1029/2009GC002440.

Long M.D., 2009a, Complex anisotropy in D" beneath the eastern Pacific from *SKS-SKKS* splitting discrepancies, *Earth Planet. Sci. Lett.,* 283, 181-189.

Long M.D., 2009b, Going with the mantle flow, *Nat. Geosci.,* 2, 10-11.

Long M.D., 2010, Frequency-dependent shear wave splitting and heterogeneous anisotropic structure beneath the Gulf of California region, *Phys. Earth Planet. Inter.,* 182, 59-72, doi:10.1016/j.pepi.2010.06.005.

Long M.D., 2013, Constraints on subduction geodynamics from seismic anisotropy, *Rev. Geophys.,* 51, 76-112, doi:10.1002/rog.20008.

Long M.D., Becker T.W., 2010, Mantle dynamics and seismic anisotropy, *Earth Planet. Sci. Lett.,* 297, 341-354, doi:10.1016/j.epsl.2010.06.036.

Long M.D., Silver P.G., 2008, The subduction zone flow field from seismic anisotropy: A global view, *Science,* 319, 315-318, doi:10.1126/science.1150809.

Long M.D., Silver P.G., 2009a, Shear wave splitting and mantle anisotropy: Measurements,

interpretations, and new directions, *Surv. Geophys.,* 30, 407-461, doi:10.1007/s10712-009-9075-1.

Long M.D., Silver P.G., 2009b, Mantle flow in subduction systems: The subslab flow field and implications for mantle dynamics, *J. Geophys. Res.,* 114, B10312, doi:10.1029/2008JB006200.

Long M.D., Wirth E.A., 2013, Mantle flow in subduction systems: The mantle wedge flow field and implications for wedge processes, *J. Geophys. Res. Solid Earth,* 118, 583-606, doi:10.1002/jgrb.50063.

Lynner C., Long M.D., 2013,Sub-slab seismic anisotropy and mantle flow beneath the Caribbean and Scotia subduction zones: Effects of slab morphology and kinematics, *Earth Planet. Sci. Lett.* 361, 367-378, doi:10.1016/j.epsl.2012.11.007.

Lynner C., Long M.D., 2014a, Sub-slab anisotropy beneath the Sumatra and circum-Pacific subduction zones from source-side shear wave splitting observations, *Geochem. Geophys. Geosyst.,* 15, 2262–2281, doi:10.1002/2014GC005239.

Lynner C., Long M.D., 2014b, Testing models of sub-slab anisotropy using a global compilation of source-side shear wave splitting data, *J. Geophys. Res. Solid Earth,* 119, 7226-7244, doi:10.1002/2014JB010983.

Macías J.L., 2005, Geología e historia eruptiva de algunos de los grandes volcanes activos de México, *Bol. Soc. Geol. Mex.,* LVII, 379-424.

Mainprice D., Silver P.G., 1993, Interpretation of *SKS*-waves using samples from the subcontinental lithosphere, *Phys. Earth Planet. Inter.,* 78, 257-280.

Manea M., Manea V.C., 2008, On the origin of El Chichón volcano and subduction of Tehuantepec Ridge: A geodynamical perspective, *J. Volcanol. Geotherm. Res.,* 175, 459-471, doi:10.1016/j.jvolgeores.2008.02.028.

Manea V.C., Manea M., 2011, Flat-slab thermal structure and evolution beneath central Mexico, *Pure Appl. Geophys.,* 168, 1475-1487, doi:10.1007/s00024-010-0207-9.

Manea M., Manea V.C., Ferrari L., Kostoglodov V., Bandy W.L., 2005, Tectonic evolution of the Tehuantepec ridge, *Earth Planet. Sci. Lett.,* 238, 64-77.

MASE, 2007, Meso America subduction experiment, Caltech, dataset, Pasadena, CA, USA, doi:10.7909/C3RN35SP.

Melgar D., Pérez-Campos X., 2011, Imaging the Moho and subducted oceanic crust at the Isthmus of Tehuantepec, Mexico, from receiver functions, *Pure Appl. Geophys.,* 168, 1449-1460, doi:10.1007/s00024-010-0199-5.

Neumann F., Vásquez-Serrano A., Tolson G., Negrete-Aranda R., Contreras J., 2016, Toroidal, counter-toroidal, and upwelling flow in the mantle wedge of the Rivera and Cocos plates: Implications for IOB geochemistry in the Trans-Mexican Volcanic Belt, *Pure Appl. Geophys.,* 173, 3395-3417, doi:10.1007/s00024-015-1218-3.

Nicolas A., 1993, Why fast polarization directions of *SKS* seismic waves are parallel to mountain belts, *Phys. Earth Planet. Inter.,* 78, 337-342.

Nicolas A., Christensen N.I., 1987, Formation of anisotropy in upper mantle peridotites: A review, in *Composition, Structure and Dynamics of the Lithosphere-Asthenosphere System, Geodyn. Ser.,* 16, edited by K. Fuchs and C. Froidevaux, pp. 111-123, AGU, Washington, D. C., USA.

Obrebski M.J., 2007, Estudio de la anisotropía sísmica y su relación con la tectónica de Baja California, Ph. D. thesis, 221 pp., Centro de Investigación Científica y de Educación Superior de Ensenada, Ensenada, B. C., Mexico.

Obrebski M., Castro R.R., 2008, Seismic anisotropy in northern and central Gulf of California region, Mexico, from teleseismic receiver functions and new evidence of possible plate capture, *J. Geophys. Res.,* 113, B03301, doi:10.1029/2007JB005156.

Obrebski M., Castro R.R., Valenzuela R.W., van Benthem S., Rebollar C.J., 2006, Shear-wave splitting observations at the regions of northern Baja California and southern Basin and Range in Mexico, *Geophys. Res. Lett.,* 33, L05302, doi:10.1029/2005GL024720.

Ortega-Gutiérrez F., Mitre-Salazar L.M., Roldán-Quintana J., Aranda-Gómez J., Morán-Zenteno D., Alaniz-Alvarez S., Nieto-Samaniego A., 1992, Carta geológica de la República Mexicana, *Fifth edition,* scale 1:2,000,000, Instituto de Geología, Universidad Nacional Autónoma de México, Mexico City, Mexico.

Özalaybey S., Savage M.K., 1994, Double-layer anisotropy resolved from *S* phases, *Geophys. J. Int.,* 117, 653-664.

Özalaybey S., Savage M.K., 1995, Shear-wave splitting beneath western United States in relation to plate tectonics, *J. Geophys. Res.,* 100, 18,135-18,149.

Paczkowski K., Montési L.G.J., Long M.D., Thissen C.J., 2014a, Three-dimensional flow in the subslab mantle, *Geochem. Geophys. Geosyst.,* 15, 3989-4008, doi:10.1002/2014GC005441.

Paczkowski K., Thissen C.J., Long M.D., Montési L.G.J., 2014b, Deflection of mantle flow beneath subducting slabs and the origin of subslab anisotropy, *Geophys. Res. Lett.,* 41, 6734-6742, doi:10.1002/2014GL060914.

Pardo M., Suárez G., 1993, Steep subduction geometry of the Rivera plate beneath the Jalisco block in western Mexico, *Geophys. Res. Lett.,* 20, 2391-2394.

Pardo M., Suárez G., 1995, Shape of the subducted Rivera and Cocos plates in southern Mexico: Seismic and tectonic implications, *J. Geophys. Res.,* 100, 12,357-12,373.

Park J., Levin V., 2002, Seismic anisotropy: Tracing plate dynamics in the mantle, *Science,* 296, 485-489.

Pérez-Campos X., Kim Y., Husker A., Davis P.M., Clayton R.W., Iglesias A., Pacheco J.F., Singh S. K., Manea V.C., Gurnis M., 2008, Horizontal subduction and truncation of the Cocos plate beneath central Mexico, *Geophys. Res. Lett.,* 35, L18303, doi:10.1029/2008GL035127.

Phipps Morgan J., Hasenclever J., Hort M., Rüpke L., Parmentier E.M., 2007, On subducting slab entrainment of buoyant asthenosphere, *Terra Nova,* 19, 167-173, doi:10.1111/j.1365-3121.2007.00737.x.

Polet J., Kanamori H., 2002, Anisotropy beneath California: Shear wave splitting measurements using a dense broadband array, *Geophys. J. Int.,* 149, 313-327.

Ponce-Cortés J.G., 2012, Medición de la anisotropía de las ondas *SKS* en el manto superior, debajo de las estaciones permanentes del Servicio Sismológico Nacional instaladas a partir del año 2005, B. Sc. thesis, 79 pp., Facultad de Ingeniería, Universidad Nacional Autónoma de México, Mexico City, Mexico.

Ramos-Zuñiga L.G., Montalvo-Arrieta J.C., Pérez-Campos X., Valdés-González C., 2012, Seismic characterization of station LNIG as a reference site in northeast Mexico, *Geofís. Int.,* 51, 187-197.

Refayee H.A., Yang B.B., Liu K.H., Gao S.S., 2014, Mantle flow and lithosphere-asthenosphere coupling beneath the southwestern edge of the North American craton: Constraints from shear-wave splitting measurements, *Earth Planet. Sci. Lett.,* 402, 209-220, doi:10.1016/j.epsl.2013.01.031.

Rodríguez-Domínguez M.A., 2016, Transición del ángulo de subducción de la placa de Cocos en la zona centro-sur de México, M. Sc. thesis, 68 pp., Instituto de Geofísica, Universidad Nacional Autónoma de México, Mexico City, Mexico.

Rodríguez-Pérez Q., 2007, Estructura tridimensional de velocidades para el sureste de México, mediante el análisis de trazado de rayos sísmicos de sismos regionales, M. Sc. thesis, 83 pp., Instituto de Geofísica, Universidad Nacional Autónoma de México, Mexico City, Mexico.

Rojo-Garibaldi B., 2011, Anisotropía de las ondas *SKS* en el manto superior debajo de un arreglo sísmico entre Guerrero y Veracruz, B. Sc. thesis, 84 pp., Facultad de Ciencias, Universidad Nacional Autónoma de México, Mexico City, Mexico.

Romo J.M., García-Abdeslem J., Gómez-Treviño E., Esparza F.J., Flores C., 2001, Resultados preliminares de un perfil geofísico a través del desierto de Viscaíno en Baja California Sur, México (in Spanish), *Geos Boletín Informativo de la UGM,* 21, 96-107.

Ruppert S.D., 1992, Tectonics of western North America: A teleseismic view, Ph. D. thesis, 216 pp., Stanford University, Stanford, California, USA.

Russo R.M., Silver P.G., 1994, Trench-parallel flow beneath the Nazca plate from seismic anisotropy, *Science,* 263, 1105-1111.

Satsukawa T., Michibayashi K., Raye U., Anthony E.Y., Pulliam J., Stern R., 2010, Uppermost mantle anisotropy beneath the southern Laurentian margin: Evidence from Knippa peridotite xenoliths, Texas, *Geophys. Res. Lett.,* 37, L20312, doi:10.1029/2010GL044538.

Savage M.K., 1999, Seismic anisotropy and mantle deformation: What have we learned

from shear wave splitting?, *Rev. Geophys.,* 37, 65-106.

Savage M.K., Sheehan A.F., 2000, Seismic anisotropy and mantle flow from the Great Basin to the Great Plains, western United States, *J. Geophys. Res.,* 105, 13,715-13,734.

Savage M.K., Silver P.G., 1993, Mantle deformation and tectonics: Constraints from seismic anisotropy in the western United States, *Phys. Earth Planet. Inter.,* 78, 207-227.

Savage M.K., Silver P.G., Meyer R.P., 1990, Observations of teleseismic shear-wave splitting in the Basin and Range from portable and permanent stations, *Geophys. Res. Lett.,* 17, 21-24.

Schellart W.P., 2004, Kinematics of subduction and subduction-induced flow in the upper mantle, *J. Geophys. Res.,* 109, B07401, doi:10.1029/2004JB002970.

Sedlock R.L., 2003, Geology and tectonics of the Baja California peninsula and adjacent areas, in *Tectonic evolution of northwestern Mexico and the southwestern USA, Special Paper 374,* edited by S. E. Johnson, S. R. Paterson, J. M. Fletcher, G. H. Girty, D. L. Kimbrough and A. Martín-Barajas, pp. 1-42, Geological Society of America, Boulder, Colorado, USA, doi:10.1130/0-8137-2347-4.1.

Sedlock R.L., Ortega-Gutiérrez F., Speed R.C., 1993, *Tectonostratigraphic terranes and tectonic evolution of Mexico, Special Paper 278.* Geological Society of America, Boulder, Colorado, USA, 146 pp.

Sheehan A.F., Jones C.H., Savage M.K., Ozalaybey S., Schneider J.M., 1997, Contrasting lithospheric structure between the Colorado Plateau and Great Basin: Initial results from Colorado Plateau-Great Basin PASSCAL experiment, *Geophys. Res. Lett.,* 24, 2609-2612.

Silver P.G., 1996, Seismic anisotropy beneath the continents: Probing the depths of Geology, *Annu. Rev. Earth Planet. Sci.,* 24, 385-432.

Silver P.G., Chan W.W., 1988, Implications for continental structure and evolution from seismic anisotropy, *Nature,* 335, 34-39.

Silver P.G., Chan W.W., 1991, Shear wave splitting and subcontinental mantle deformation, *J. Geophys. Res.,* 96, 16,429-16,454.

Silver P.G., Holt W.E., 2002, The mantle flow field beneath western North America, *Science,* 295, 1054-1057.

Silver P.G., Kaneshima S., 1993, Constraints on mantle anisotropy beneath Precambrian North America from a transportable teleseismic experiment, *Geophys. Res. Lett.,* 20, 1127-1130.

Silver P.G., Savage M.K., 1994, The interpretation of shear-wave splitting parameters in the presence of two anisotropic layers, *Geophys. J. Int.,* 119, 949-963.

Singh S.K., Pacheco J., Courboulex F., Novelo D.A., 1997, Source parameters of the Pinotepa Nacional, Mexico, earthquake of 27 March, 1996 (M_w = 5.4) estimated from near-field recordings of a single station, *J. Seismol.,* 1, 39-45.

Song T.-R.A., Kawakatsu H., 2012, Subduction of oceanic asthenosphere: Evidence from sub-slab seismic anisotropy, *Geophys. Res. Lett.,* 39, L17301, doi:10.1029/2012GL052639.

Stegman D.R., Freeman J., Schellart W.P., Moresi L., May D., 2006, Influence of trench width on subduction hinge retreat rates in 3-D models of slab rollback, *Geochem. Geophys. Geosyst.,* 7, Q03012, doi:10.1029/2005GC001056.

Stein S., Wysession, M., 2003, *An introduction to seismology, earthquakes, and Earth structure.* Blackwell Publishing, Malden, MA, USA, 498 pp.

Stubailo I., 2015, Seismic anisotropy below Mexico and its implications for mantle dynamics, Ph. D. thesis, 119 pp., University of California, Los Angeles, CA, USA.

Stubailo I., Davis P., 2007, Shear wave splitting measurements and interpretation beneath Acapulco-Tampico transect in Mexico, *Eos Trans. AGU,* 88, 52, Fall Meet. Suppl., Abstract T51B-0539.

Stubailo I., Davis P.M., 2012a, Anisotropy of the Mexico subduction zone based on shear-wave splitting analysis (abstract), *Seism. Res. Lett.,* 83, 2, 379.

Stubailo I., Davis P.M., 2012b, Anisotropy of the Mexico subduction zone based on shear-wave splitting and higher modes analysis, Abstract T11A-2538 presented at 2012 Fall Meeting, AGU, San Francisco, CA, 3-7 Dec.

Stubailo I., Davis P.M., 2015, The surface wave, shear wave splitting, and higher mode seismic anisotropy comparison of the Mexican subduction zone (abstract), *Seism. Res. Lett.,* 86, 2B, 677.

Stubailo I., Beghein C., Davis P.M., 2012, Structure and anisotropy of the Mexico subduction zone based on Rayleigh-wave analysis and implications for the geometry of the Trans-Mexican Volcanic Belt, *J. Geophys. Res.,* 117, B05303, doi:10.1029/2011JB008631.

Suarez G., Singh S.K., 1986, Tectonic interpretation of the Trans-Mexican Volcanic Belt — Discussion, *Tectonophysics,* 127, 155-158.

Trampert J., Paulssen H., van Wettum A., Ritsema J., Clayton R., Castro R., Rebollar C., Pérez-Vertti A., 2003, New array monitors seismic activity near the Gulf of California in Mexico, *Eos Trans. AGU,* 84, 29, 32.

Valdés-González C., Cárdenas-Ramírez A., Cruz-Cervantes J.L., Estrada-Castillo J., Pérez-Santana J., Santiago-Santiago J. A., Jiménez-Cruz C., Gutiérrez-García A., Rubí-Zavala B., 2005, ¿20 años después del sismo de 1985, sísmicamente qué le falta a la red del Servicio Sismológico Nacional? (abstract), *Geos Boletín Informativo de la UGM,* 25, 1, 185.

Valdés-González C., Jiménez-Cruz C., Espíndola-Castro V.H., Estrada-Castillo J.A., Pérez-Santana J.A., Franco-Sánchez S. ., Cárdenas-Monroy C., Li-Tan Y., Cárdenas-Ramírez A. B., Cruz-Cervantes J.L., Navarro-Estrada F., Rodríguez-Rasilla I., Hurtado-Díaz A., Arreola-Manzano J., Caballero-Jiménez G.V., González-López A., Hernández-Valdivia L., Vidal-Amaro M., 2012, El Servicio Sismológico Nacional: Actividad sísmica 2011-2012 en México (abstract), *Geos Boletín Informativo de la UGM,* 32, 1, 262.

Valenzuela-Wong R., León-Soto G., van Benthem S., Bernal-Díaz A., Bernal-López L., Ponce-Cortés G., Rojo-Garibaldi B., 2015, Anisotropía sísmica y flujo del manto superior en la zona de subducción de las placas de Cocos y Rivera en México, Abstract SR02-2 presented at the 2015 Meeting "Avances y retos en Sismología, Ingeniería y Gestión de riesgos a 30 años del sismo de 1985", Mexico City, Mexico, 17-19 Sept.

Van Benthem S.A.C., 2005, Anisotropy and flow in the uppermantle under Mexico, M. Sc. thesis, 41 pp., Utrecht University, Utrecht, The Netherlands.

Van Benthem S.A., Valenzuela R.W., 2007, Upper mantle shear wave anisotropy for stations in Mexico and its relationship to subduction at the Middle America Trench, *Eos Trans. AGU,* 88, 23, Jt. Assem. Suppl., Abstract S51C-07.

Van Benthem S.A.C., Valenzuela R.W., Obrebski M., Castro R.R., 2008, Measurements of upper mantle shear wave anisotropy from stations around the southern Gulf of California, *Geofís. Int.,* 47, 127-143.

Van Benthem S.A.C., Valenzuela R.W., Ponce G.J., 2013, Measurements of shear wave anisotropy from a permanent network in southern Mexico, *Geofís. Int.,* 52, 385–402, doi:10.1016/S0016-7169(13)71485-5.

Vauchez A., Nicolas A., 1991, Mountain building: Strike-parallel motion and mantle anisotropy, *Tectonophysics,* 185, 183-201.

VEOX, 2010, Veracruz-Oaxaca subduction experiment, Caltech, dataset, Pasadena, CA, USA, doi:10.7909/C3MW2F2C.

Vinnik L.P., Kind R., 1993, Ellipticity of teleseismic *S*-particle motion, *Geophys. J. Int.,* 113, 165-174.

Vinnik L.P., Kind R., Kosarev G.L., Makeyeva L. I., 1989a, Azimuthal anisotropy in the lithosphere from observations of long-period *S*-waves, *Geophys. J. Int.,* 99, 549-559.

Vinnik L.P., Farra V., Romanowicz B., 1989b, Azimuthal anisotropy in the Earth from observations of *SKS* at Geoscope and NARS broadband stations, *Bull. Seism. Soc. Am.,* 79, 1542-1558.

Vinnik L.P., Makeyeva L.I., Milev A., Usenko A. Yu., 1992, Global patterns of azimuthal anisotropy and deformations in the continental mantle, *Geophys. J. Int.,* 111, 433-447.

Vinnik L., Romanowicz B., Le Stunff Y., Makeyeva L., 1995, Seismic anisotropy in the D" layer, *Geophys. Res. Lett.,* 22, 1657-1660.

Vinnik L.P., Green R.W.E., Nicolaysen L. O., 1996, Seismic constraints on dynamics of the mantle of the Kaapvaal craton, *Phys. Earth Planet. Inter.,* 95, 139-151.

Wang Y., Forsyth D.W., Savage B., 2009, Convective upwelling in the mantle beneath the Gulf of California, *Nature,* 462, 499-502.

Wessel P., Smith W.H.F., 1998, New, improved version of Generic Mapping Tools released, *Eos Trans. AGU,* 79, 579.

Wiens D.A., Conder J.A., Faul U.H., 2008, The seismic structure and dynamics of the mantle wedge, *Annu. Rev. Earth Planet. Sci.,* 36, 421-455, doi:10.1146/annurev.earth.33.092203.122633.

Wolfe C.J., Silver P.G., 1998, Seismic anisotropy of oceanic upper mantle: Shear wave splitting methodologies and observations, *J. Geophys. Res.,* 103, 749-771.

Wookey J., Kendall J.M., 2004, Evidence of midmantle anisotropy from shear wave splitting and the influence of shear-coupled *P* waves, *J. Geophys. Res.,* 109, B07309, doi:10.1029/2003JB002871.

Wookey J., Kendall J.M., Barruol G., 2002, Mid-mantle deformation inferred from seismic anisotropy, *Nature,* 415, 777–780.

Wüstefeld A., Bokelmann G., Barruol G., Montagner J.P., 2009, Identifying global seismic anisotropy patterns by correlating shear-wave splitting and surface-wave data, *Phys. Earth Planet. Inter.,* 176, 198-212, doi:10.1016/j.pepi.2009.05.006.

Yang T., Grand S.P., Wilson D., Guzmán-Speziale M., Gómez-González J.M., Domínguez-Reyes T., Ni J., 2009, Seismic structure beneath the Rivera subduction zone from finite-frequency seismic tomography, *J. Geophys. Res.,* 114, B01302, doi:10.1029/2008JB005830.

Zhang S., Karato S.-I., 1995, Lattice preferred orientation of olivine aggregates deformed in simple shear, *Nature,* 375, 774–777.

Zhang X., Paulssen H., Lebedev S, Meier T., 2007, Surface wave tomography of the Gulf of California, *Geophys. Res. Lett.,* 34, L15305, doi:10.1029/2007GL030631.

Zhang X., Paulssen H., Lebedev S, Meier T., 2009, 3D shear velocity structure beneath the Gulf of California from Rayleigh wave dispersion, *Earth Planet. Sci. Lett.,* 279, 255-262, doi:10.1016/j.epsl.2009.01.003.

Geofísica Internacional (2017) 56-2: 219-227

Short Note

Interior Imaging of El Castillo Pyramid, Chichen Itza, Mexico, Using ERT-3D Methods: Preliminary Results

René E. Chavez*, Andrés Tejero, Denisse L. Argote, Gerardo Cifuentes, Juan Esteban Hernández-Quintero and Alejandro García-Serrano

Received: December 08, 2016; accepted: March 17, 2017; published on line: April 01, 2017

Resumen

La famosa Pirámide del Castillo, ubicada en Chichén Itzá, hacia la parte norte de la Península de Yucatán, México, es una estructura emblemática de este sitio arqueológico y elegida como una de las siete maravillas hechas por el hombre. Los arqueólogos que restauraron esta estructura durante los años 30 descubrieron una pirámide más pequeña dentro de este edificio prehispánico, que correspondía a un período maya más antiguo. La posibilidad de encontrar otros períodos de construcción dentro de este edificio es muy importante para reconstruir la historia maya de la región. Estudios geofísicos anteriores llevados a cabo por los autores en 2014, utilizando nuevos arreglos de Tomografía de Resistividad Eléctrica (TRE), mostraron una cavidad natural parcialmente llena de agua dulce debajo de la Pirámide de El Castillo. Empleando una técnica similar, se desplegó una serie de electrodos planos en cada uno de los 9 cuerpos (o niveles) que conformaban la pirámide más la base de la estructura, manteniendo constante la distancia entre cada electrodo. Se realizó un control topográfico preciso para cada electrodo, el que se introdujo en el proceso de inversión. Se calcularon 37.520 observaciones dentro de la pirámide. Cinco de los 10 niveles de observación (19.400 puntos), han sido procesados hasta ahora. Se analizaron secciones horizontales y verticales de esta imagen invertida. Examinando las diferencias en los valores de resistividad y sus correspondientes gradientes se pudieron localizar, la primera subestructura (explorada en la década de 1930), así como inferir una segunda subestructura dentro de la anterior. Se levantó un perfil ERT-2D dentro de la pirámide de El Castillo, al interior de un túnel excavado en 1934 y la escalera de la primera pirámide interna. Los resultados de este estudio parecen confirmar la evidencia de una segunda subestructura dentro del interior de El Castillo. Dicho rasgo resistivo posee una cámara probablemente intacta (una habitación rectangular de 3 m de altura) en su parte superior y dimensiones inferidas de 10 m de altura y 23 m por lado en su base, suponiendo que el final de este perfil se encuentre en el centro de la subestructura 2. Cuando la inversión se lleve a cabo integrando los 10 niveles, se tendrá una mejor resolución para las porciones superiores del modelo de resistividad.

Palabras clave: Tomografía de resistividad eléctrica, proceso de inversión, pirámide El Castillo, Chichen Itza, México, Arqueología.

R. Chavez
G. Cifuentes[1]
J. E. Hernández-Quintero
Instituto de Geofísica
Universidad Nacional Autónoma de México
Ciudad Universitaria
Delegación Coyoacán, 04510
México, CDMX, México
*Corresponding author: exprene@geofisica.unam.mx

A. Tejero
A. García-Serrano
Facultad de Ingeniería
Universidad Nacional Autónoma de México
Ciudad Universitaria
Delegación Coyoacán, 04510
México, CDMX, México

D. Argote
Dirección de Estudios Arqueológicos
INAH
México, CDMX, México

Abstract

The famous El Castillo pyramid, located in Chichen Itza, towards the northern portion of the Yucatan Peninsula, Mexico, is an emblematic structure of this archaeological site and recognized as one of the man-made world seven wonders. The archaeologists that restored this structure during the 1930's discovered a smaller pyramid inside this pre-Hispanic edifice, which corresponded to an older Mayan period. The possibility of finding other construction periods inside this edifice should be important in order to reconstruct the Mayan history of the region. Previous geophysical studies carried out in 2014 by the authors, showed a buried natural cavity partially filled with water beneath El Castillo pyramid, using novel Electrical Resistivity Tomography (ERT) arrays. Employing a similar technique, a series of flat electrodes were deployed on each of the 9 bodies (or levels) conforming the pyramid plus the base of the structure, keeping a constant distance between each electrode. A precise topographic control for each electrode was fulfilled and introduced in the inversion process. 37,520 observations inside the pyramid were computed. So far, five of the 10 observation levels (19,400 points), were processed. Horizontal and vertical slices of this inverted image were analyzed. Examining the differences in the resistivity values and their gradients, allowed to locate the first substructure (explored in the 1930's), as well as to infer a second substructure inside the previous one. An ERT-2D profile was surveyed inside El Castillo pyramid at the interior of a tunnel excavated in 1934 and the stairway of the first inner pyramid. Results from this study seem to confirm the evidence of a second substructure within El Castillo's interior. Such feature possesses a probable intact chamber (a rectangular room 3 m high) on its upper part and inferred dimensions of 10 m high and 23 m per side at its base, assuming that the end of this profile lies on the middle of substructure 2. When the inversion will be carried out for the 10 levels, a better resolution will be reached for the upper portions of the resistivity model..

Key words: Electrical Resistivity Tomography, inversion process, El Castillo pyramid, Chichen Itza, Mexico, archaeology.

Introduction

El Castillo pyramid is located in the archaeological zone of Chichen Itza (Figure 1A), in the southeastern lowlands of Mexico, within the Yucatan Peninsula (Figure 1B). This magnificent building is probably the most important edifice within the archaeological site (Figure 1C).

Traditionally, archaeologists have considered that this Mayan city was occupied by different ethnic groups in the time, moving from an "Older Chichén Itza" to a "New Chichen Itza". Different constructive styles are found in the region, the Puuc would be developed in Chichen Itza towards the Late Classic and Terminal Classic periods (600-900 AD) and can be seen towards the southern part of the site. On the other hand, the architectural style called Maya-Toltec is related to the influence of groups coming from Central Mexico around 900 AD. Recent studies, based on petrographic analyzes and dating by the Thermoluminescence technique of ceramic samples, predominant in the region (Chung Seu, 2000) and relative dating (Schmidt, 1998; Osorio, 2004; Pérez Heredia, 2004), established the starting cultural sequence as:

• Episode I, 550-800 AD, arrival of the first '*pure*' Mayas, reflecting in their materials a remarkable southern tradition of the Yucatan peninsula. This episode could be correlated with the Yabnal/Motul ceramic complex, related to the beginning of the urban development of the site.

• Episode II, 750-800 AD, the main period of development and expansion of Chichen Itza, maintaining a close relationship with the south and west of the peninsula (Tabasco and Chiapas). This episode could be correlated with the complexes Cehpech (associated with the "Puuc" style buildings) and Sotuta (associated directly with the maximum splendor of Chichen Itza and corresponding to the architecture called "Maya-Toltec").

• Episode III, 1100-1300 AD, decay and arrival of another foreign group with cultural features from Central Mexico. This episode could be correlated with the Hocabá complex, recovered mainly in contexts of reoccupation of the site.

The two last constructive phases of the pyramid, the one we see nowadays and substructure 1, correspond to Episode II.

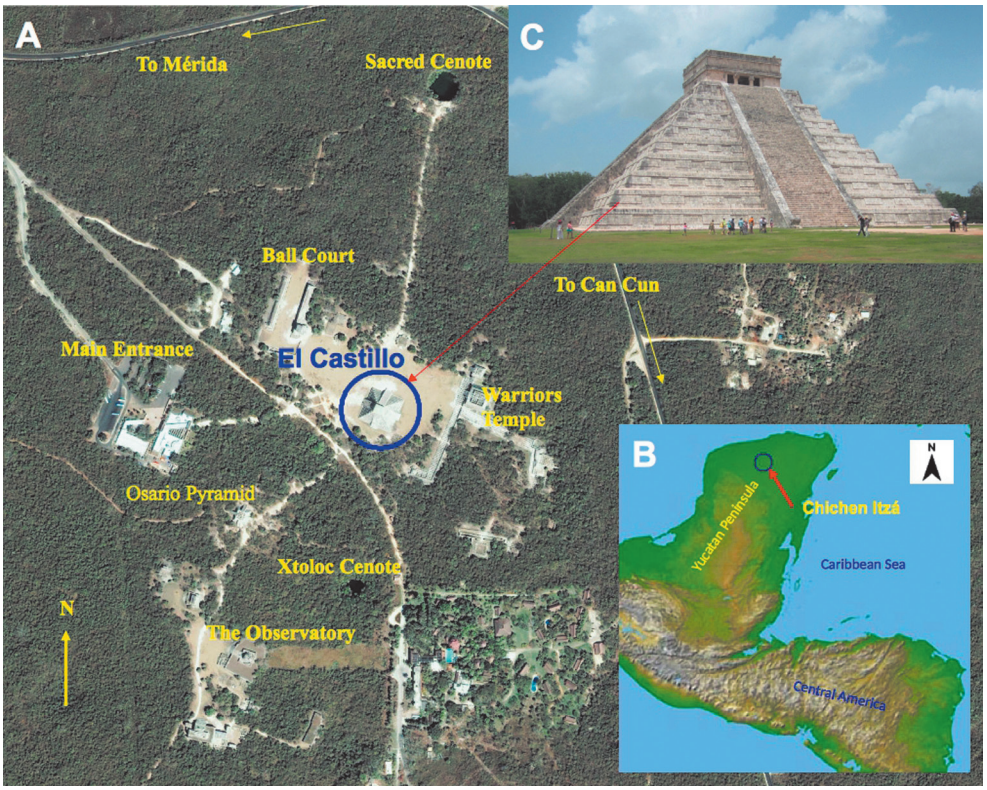

Figure 1. Image from the archaeological site of Chichen Itza taken by the IKONOS satellite in 2001 (A). The archaeological site is found towards the northern portion of the Yucatan Peninsula (B). The location of El Castillo pyramid (blue circle) at the center of this view and the nowadays structure are shown (C).

The edification of the actual pyramid is dated approximately between the years 900 and 1000 AD, while the first substructure, unveiled during the 1930's, is dated around 850 AD. An edifice corresponding to Episode I has been a controversial topic among the Mayan specialists.

Therefore, the present research is devoted to explore the interior of El Castillo pyramid employing a non-conventional and non-invasive technology able to '*illuminate*' the pyramid´s interior in order to define the constructive phases inside this pyramid.

Methodology

Sometimes, spatial conditions of the surveyed area do not allow deployment of conventional three-dimensional electric resistivity tomography (ERT-3D) geometries (Tejero *et al*., 2015). Such constraints are imposed by natural or anthropogenic 'obstacles', which are often the targets of the proposed survey (Trogu *et al*., 2011; Argote *et al*., 2013). Alternative arrays have to be improved to solve this problem. Chávez *et al*. (2015A), and Tejero *et al*. (2015) suggested novel geometries to characterize the subsoil beneath archaeological and urban zones. In this work, the '*L*', '*Corner*', and '*Minimum Coupling*' arrays were employed, adding the so called 'Gradient' array. These non-conventional geometries attempted to 'see' the pyramid's interior (Figure 2), where two electric arrays in 'L' and four 'Corner' arrays define a squared geometry that encloses the structure of interest. Such arrays are described in detail by Argote *et al*. (2013) and Tejero *et al*. (2015). They have also demonstrated that different settings developed for ERT-2D can be employed to identify different bodies present in the subsurface. Based in these 2D electric arrays, Dahlin and Zhou (2004) analyzed the possibilities of 10 different arrays as well as their resolution for different targets. Szalai *et al*. (2015) investigated different distances between electrodes for the Wenner-Gamma array and showed that small resistive bodies can be detected. Finally, Barker (1989) focused his investigation on the penetration depth for different Wenner arrays (alfa, beta, gamma) in comparison with quadrupole sets.

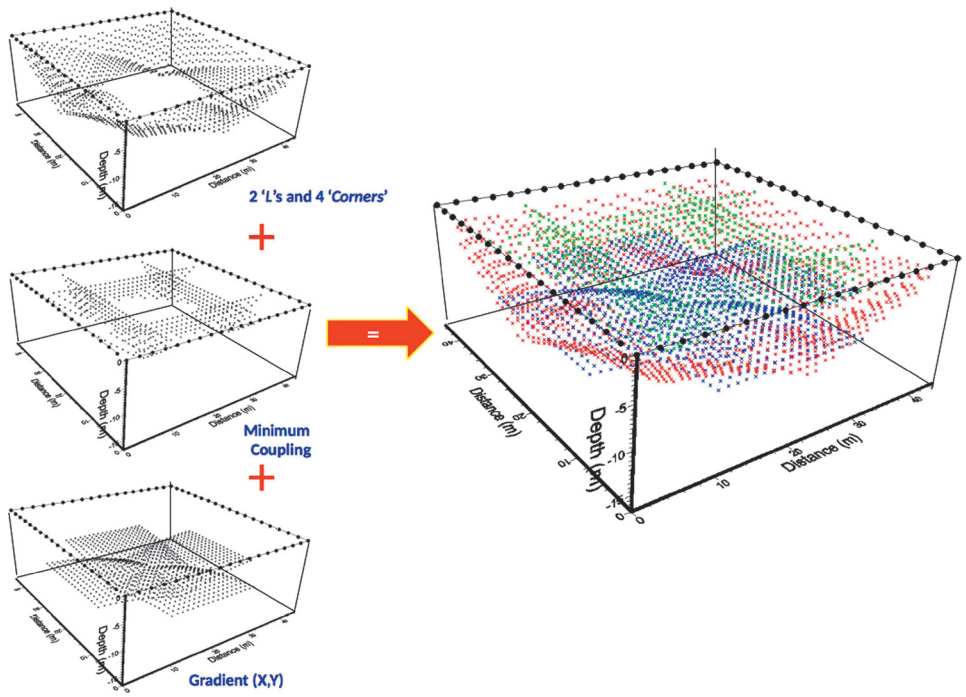

Figure 2. TRE-3D arrays employed to survey either El Castillo subsoil and its interior. Two '*L*'s, four 'Corners', Minimum Coupling (MC) and the Gradient arrays (left) were employed to cover the subsurface of each pyramid's body (right). Observed resistivities for each array are shown as small black dots (left). The total number of observations are depicted in colored dots (right). Electrodes position are shown as black circles forming the squared geometry.

In the present investigation, the Wenner-Schlumberger array was selected to construct the '*L*' array, since measured readings are less noisy, mainly towards the center of the square than those performed with dipolar settings. '*Gradient*' and '*Minimum Coupling*' arrays were employed to better resolve the inner and perimeter portions of the squared geometry.

The ERT-3D data were acquired employing a Syscal-Pro Resistivimeter (IRIS Instruments, France) with 48 channels with a switch box that allowed the addition of 48 additional electrodes. Distribution of the apparent resistivity observations at depth were computed with the software Electre-Pro (Iris Instruments, 2010). The attribution points of each observed data were calculated employing an in-house software. (Tejero *et al*., 2015) describe in detail the procedure to compute the coordinates of the attribution points. (X, Y) coordinates are calculated employing the same process followed for two dimensional arrays. For the Z coordinate or depth of investigation, the depth of the median was considered where 50% of the current flows both above and below that point. Such calculation is based on the concept of the sensitivity function for specific arrays provided by Edwards (1977) and Barker (1989).

The inversion and modelling processes were carried out with the commercial software ERTLab-64 (Geoastier-Geophysics, 2012). Data inversion is mostly based on the method described by Constable *et al*. (1987), where an objective weighted function is minimized in the sense of a root mean square method (Tejero *et al*., 2002).

El Castillo pyramid consists of 9 levels (pyramidal bodies), plus a tenth level that corresponds to the ground level (Figure 3A). Flat electrodes were placed on each body of the pyramid, starting at the top and finishing at the bottom, as shown in Figure 3B. Special gel was applied on the contact area of each electrode to assure good electrical coupling between the plate and the surface (made of stucco) of each level. It has to be mentioned that a careful control on the position (x, y, z) of each electrode was done by employing a double-frequency GPS, consisting of a base and a portable unit. This last one is located on each electrode position and referenced with the base station.

Data were acquired for each body employing the electrical arrays already mentioned. Each data obtained was corrected for positioning and topographic effects. Finally, 37,520

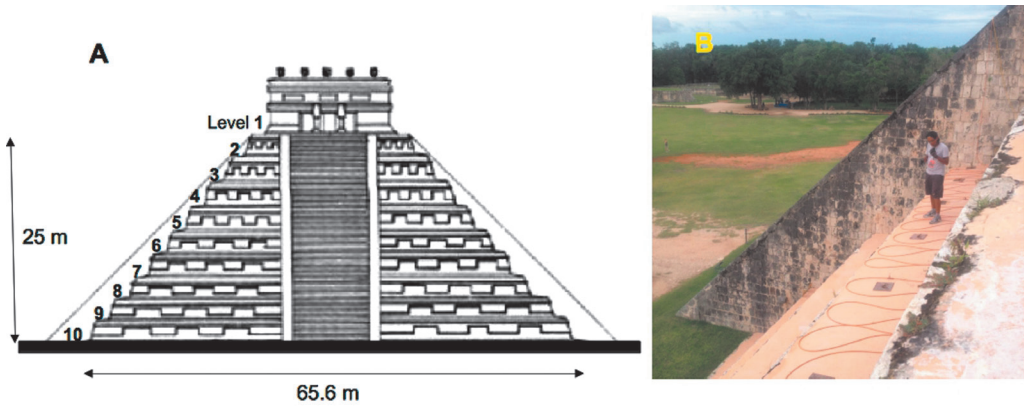

Figure 3. Schematic depiction of the dimensions of El Castillo pyramid and the 10 bodies that make up this pre-Hispanic building (A). The position of the electrodes deployed on each body is shown (B). Each electrode was deployed in the middle of each body.

observations were measured (Figure 4, colored dots). However, 19,400 apparent resistivity observations could be processed and inverted by selecting the levels 10, 9, 5, 4, and 3, since the computation capabilities available were not sufficient to compute the whole set of data. On the other hand, these bodies were inverted in order to obtain a more detailed view of the cavity beneath the pyramid, and to better resolve possible structures within El Castillo on those levels. Obviously, we will lose resolution at the top of the edifice.

Interpretation

The inverted model depicts most of the infill material employed by settlers to build the pyramid, with resistivity values around 700 Ohm-m (in green). Such materials are mostly limestone. Saturated areas (<60 Ohm-m) are depicted in blue (Figure 5A). It is important to mention that, although the apparent resistivity values measured in blocks 8, 7, 6, 2 and 1 were not inverted, their calculated topographic values in all observation levels were introduced during the inversion process for each electrode.

The inverted resistivity model viewed from its lower portion (Figure 5B) depicts the geometry of the cavity beneath El Castillo pyramid discovered in 2015 (Chavez *et al*., 2015 B). Such feature is clearly revealed, with resistivity values ranging between 20 and 80 Ohm-m. As Chavez *et al*. (2015 B) pointed out, it is very likely that this feature is partially filled with water.

In the cross-section model (Figure 6), the X and Y directions at the central portion of the pyramid (crossing planes at X=36 m) are combined, from south to north (A) and east to west (B). The location of two resistive boundaries can be inferred. The yellow line outlines the substructure 1 discovered in 1934 (Erosa-Peniche, 1939). The white discontinuous line sketches the substructure 2 inferred by the geophysical data.

It is interesting to point out, that an important resistive gradient is observed that limits the structure of El Castillo pyramid and substructure (1), delimited by the dashed yellow line. The resistivity values in this portion are about 750 Ohm-m (green), probably related to fill material (limestone made as a

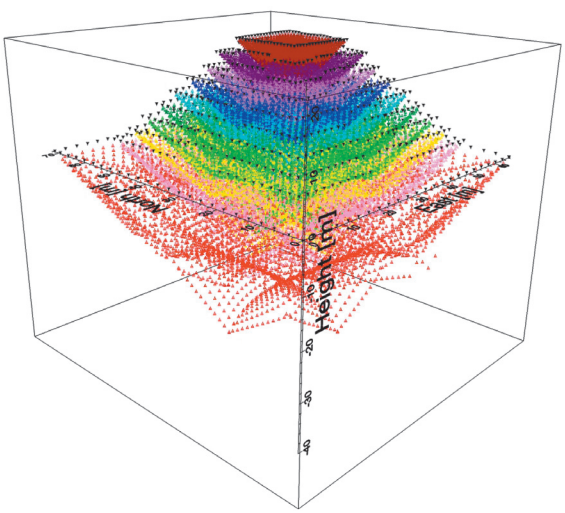

Figure 4. Observation points (cross symbol) measured inside El Castillo pyramid are depicted in different colors. A total of 37,520 data points were computed inside the pyramid. Electrode positions deployed on each pyramid body (black dots) are also shown.

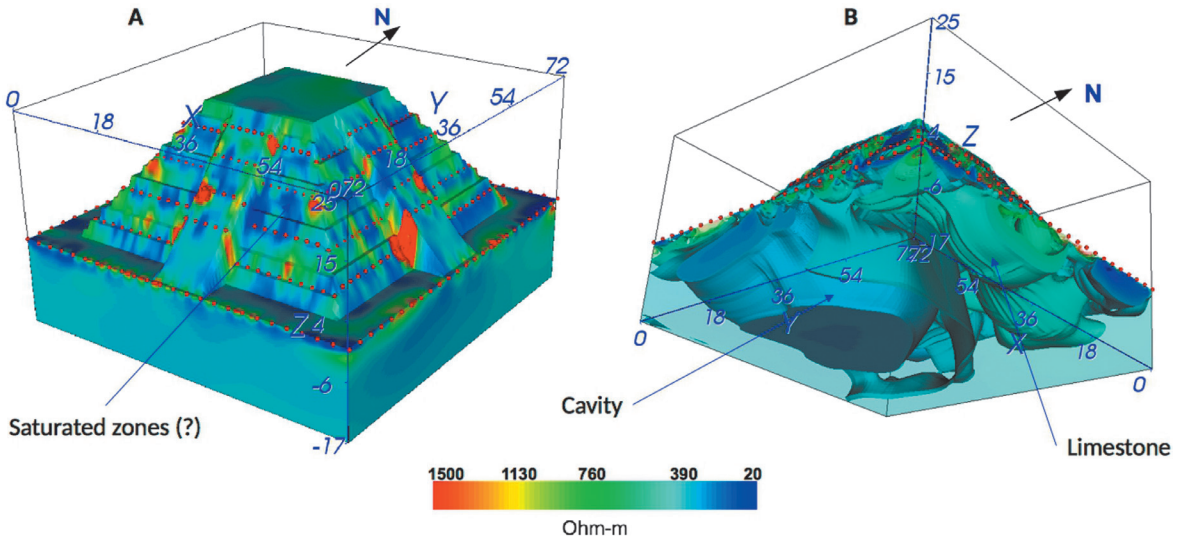

Figure 5. Side view of the southern and western faces (A) of El Castillo pyramid are depicted. In red the effects of the stairs are shown and in blue possible saturated zones. The spectacular geometry of the cavity partially filled with water is clearly seen (B), observing the model from its bottom part. Electrodes position are shown as red dots.

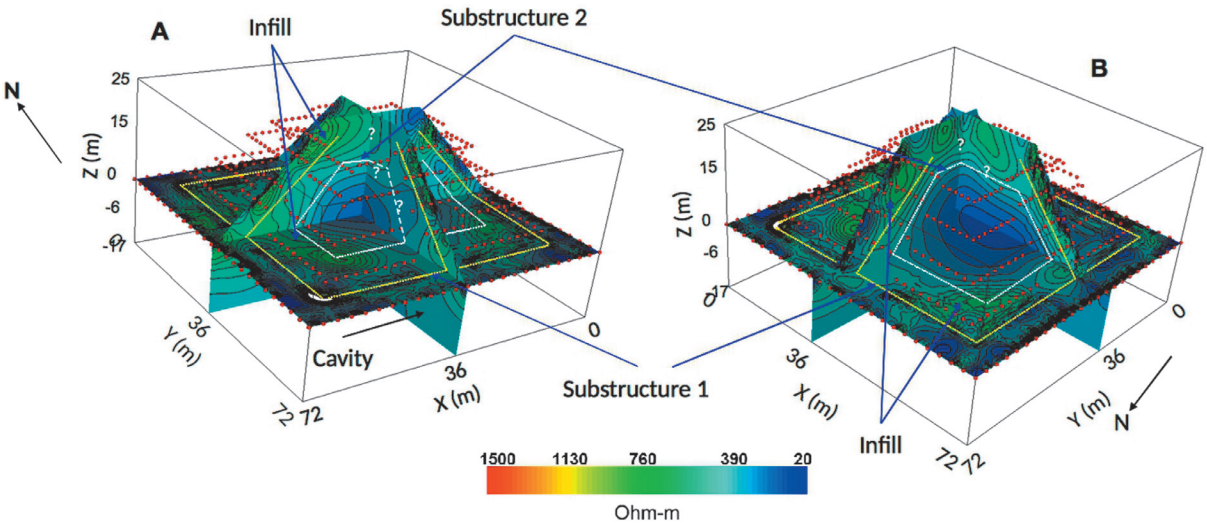

Figure 6. Detailed view of cross sections for X = 36 m and Y = 36 m and the plane Z=0 m at the base of the pyramid. Examining the resistivity gradients (values of 700 Ohm-m, approximately) for different directions in (south to north, A) and (east to west, B), it is possible to infer the location of substructure (1) (broken yellow line). Following the same process, substructure (2) can be sketched (broken white line). Notice that resistivity values for both substructures range between 80 Ohm-m (for substructure 1) and 40 to 20 Ohm-m (for substructure 2), indicating a high degree of saturation.

mortar) employed to cover this older pyramid. Such an effect can be clearly observed on the horizontal slice, where an interesting resistivity gradient is found. A similar effect might be followed that makes possible to sketch the limits (dashed white line) of substructure (2). This is more evident in the horizontal slice, where again a slight resistive gradient (~750 Ohm-m, in green) can be observed.

The upper portions of both inner structures cannot be clearly defined (question marks), even if it is well known that at the top of substructure (1), a temple is found (a jaguar-shaped throne and a Chac-Mol sculpture were found in it). Unfortunately, at this moment the

upper levels have not been yet interpreted, then the resistivity model is unable to detect that structure.

It is important to mention that both inferred bodies have low resistivities, ranging between ~ 80 Ohm-m for substructure (1), and 40 to 20 Ohm-m for substructure (2), which could indicate a high degree of saturation (humidity) of the materials that constitute the interior of El Castillo pyramid. It is worth mentioning that the region where the site is settled has an annual rainfall ranging from 1000 to 1600 mm, therefore water might infiltrate the limestone rocks and soils saturating them.

Finally, a N-S ERT-2D profile was performed inside El Castillo pyramid and over its first substructure to confirm the results obtained with the ERT-3D study concerning the presence of a second substructure (Figure 7). A total of 67 electrodes were installed along the tunnel, staircase and temple. The separation between each flat electrode was about 1 m. The data were corrected by topographic effects, electrode positioning, and noisy data.

The infill material, over which substructure (1) is supported, is shown in green tones (values between 100 and 200 Ohm-m). Subsequently, a series of higher resistivity anomalies can be observed (between 350 and almost 1000 Ohm-m), which present a very particular behavior pattern. These anomalies seemed to delimit a resistivity contrast between two different materials (broken line). These could correspond to a coating of limestone blocks of a second substructure (substructure 2).

Towards the upper portion of the profile, at the top, two very interesting resistive anomalies can be observed. The first one corresponds to a tilted highly resistive body (> 2000 Ohm-m). This structure could be associated either to a poorly consolidated material, perhaps limestone material used to cover substructure (2) during the construction of substructure (1), or to a portion of a partially destroyed tall roof of the oldest temple that probably possessed some special decoration (all made with limestone rocks).

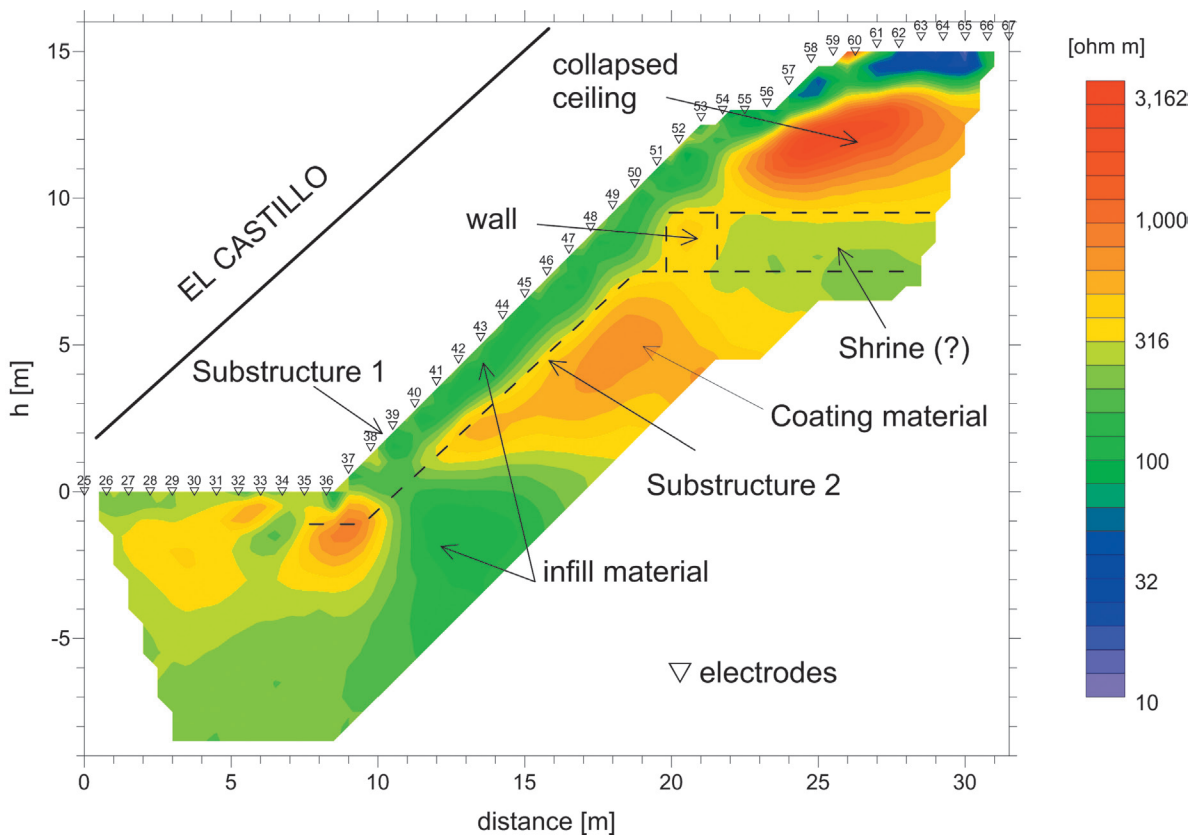

Figure 7. Geo-electric (ERT-2D) profile taken in a tunnel inside El Castillo pyramid, and over the stairway and temple of substructure (1) (Erosa-Peniche, 1939). The dotted lines show the boundary of substructure (2) covered by the infill material, on which the first one (dashed line) was built.

Commonly, Mayan temples of the Late Classic period had tall and wide rooftops, highly ornamented with large masks and sculptures representing deities and other decorations as can be seen in Ek Balam, an archaeological site located 50 km northeast of Chichén Itzá. This fact could explain the wide extension of the anomaly. This body possesses an average height of 12 m at X = 26 m, approximately.

Furthermore, below this high-resistivity anomaly, a medium-resistivity features (values ranging from 100 to 300 Ohm-m)can be seen forming a rectangular space. The geometry and the differences in the resistivity values could be reflecting the presence of a preserved temple´s chamber cover with infill material. When archaeologists in 1935 excavated and opened the main chambers of the temple corresponding to substructure (1), they were intact, only covered with infill material (Erosa-Peniche, 1939). The same case could occur for the temple located on top of substructure (2).

The low-resistivity (<25 Ohm-m) anomalies located just below the temple of substructure (1) indicate areas of high humidity. It is important to mention that inside the temple of substructure (1) a high degree of moisture occurs, which infiltrates from the outside and is deposited in the floor, filling the pores of the stucco that covers it. This could be the cause of the water saturation at this point.

Conclusions

The capability of the three-dimensional Electrical Resistivity Tomography (ERT-3D) method applied to '*illuminate*' El Castillo pyramid was demonstrated in this investigation. Mainly, because the geophysical method used is not invasive and does not disturb the historical context of the archaeological site. This type of experiment has been the first of its kind to be carried out in pre-Hispanic buildings, employing novel electrical arrays, then:

1. It was possible to design appropriate novel geo-electric arrays to 'illuminate' the pyramid's interior. The presence of substructure (1) is very well defined and the ERT- 3D results suggest the presence of a second one (substructure 2), supported by the interpretation done in the ERT-2D profile.

2. The evidence provided about the existence of substructure (2) within El Castillo, suggests that at least three different constructive phases took place in the archaeological site of Chichen Itza.

3. As soon as the inversion process for the 10 levels will be completed, a better resolution will be reached for the upper portions of the resistivity model. More detailed characteristics of substructure (2) are then expected.

Acknowledgments

The authors thank the enthusiastic collaboration of the students from the Faculty of Engineering, UNAM, in the field work. We also acknowledge authorities from INAH and the Archaeological site (M.A. Santos, O. Juarez, R. Gutierrez and E. Lopez) for the facilities granted to work in the Chichen Itza area. Our gratitude to the Hotel Mayaland managers for their support during the field work. This research was carried out through the project PAPIIT IN103614 DGAPA-UNAM and an exceptional award from the Coordinación de la Investigación Científica, UNAM.

References

Argote D., Tejero A., Cifuentes G., Iriarte L., Farías S., Chávez R.E., López F., 2013, 3D electrical prospection in the archaeological site El Pahñu, Hidalgo State, Central Mexico: *Journal of Archaeological Science*, 40, 1213-1223.

Barker R.D., 1989, Depth of investigation of collinear symmetrical four-electrode array. *Geophysics*, 54-8, 1031-1037

Chávez R.E., Tejero A., Cifuentes G., Hernández J.E., Aguilar D., 2015A, Imaging fractures beneath a residential complex using novel 3D electrical resistivity arrays: *Journal of Environmental and Engineering Geophysics*, 20-3, 219-233.

Chávez R.E., Tejero A., Cifuentes G., Argote D.L., Hernández J.E., 2015B, A special ERT-3D array carried out to investigate the subsoil of the Pyramid El Castillo, Chichen Itza, Mexico: 21th Near Surface Geophysics Abstract Book, 21, 1-4. Turin, Italy.

Chung Seu H., 2000, Chichén Itzá de 800 a 1200 d.C. Doctoral Thesis, Facultad de Filosofía y Letras, UNAM, México.

Constable S.C., Parker R.L., Constable C.G., 1987, Occam´s inversion: A practical algorithm for generating smooth models from electromagnetic sounding data. *Geophysics*, 52, 289-300.

Dahlin T., Zhou B., 2004, A numerical Comparison of 2D resistivity imaging with 10 electrod

arrays: *Geophysical Prospecting*, 52, 379-398.

Edwards L.S., 1977, A modified pseudosection for resistivity and induced polarization: *Geophysics*, 42, 1020-1036.

Erosa-Peniche J.A., 1939, "Descubrimiento y Exploración Arqueológica de la Subestructura del Castillo en Chichén Itzá". En: *Actas del XXVII Congreso Internacional de Americanistas, Primera Sesió*n, Vol. II. México, pp. 229-248.

Geoastier-Geophysics, 2012, Curso Introductorio del Software ERTLab@, *www.geoastier.com*.

IRIS Instruments, 2010, ElectrePro@ software: User manual. *www.iris-instruments.com*.

Osorio León J.F.J., 2004, La estructura 5C4 (Templo de la serie inicial) un edificio clave para la cronología en Chichén Itzá. Tesis de Licenciatura en Ciencias Antropológicas en la especialidad de Arqueología, Facultad de Ciencias Antropológicas, UADY, Yucatán, México.

Pérez Heredia E., 2004, Informe de Excavaciones en la Estructura 7B3, Edificio de Los Tres Dinteles. Archivo Técnico, INAH, México.

Schmidt P., 1998, Informe del Proyecto Chichén Itzá, Ampliación 1998. Archivo Técnico, INAH, México.

Schmidt P., 2011, Los oficiantes de la pirámide del Osario en Chichen Itzá. In B. Arroyo, L. Paiz, A. Linares and A. Arroyave (eds.), XXIV Simposio de Investigaciones Arqueológicas en Guatemala 2010. Museo Nacional de Arqueología y Etnología, Guatemala, pp. 1163-1179.

Szalai S., Lemperger I., Metwaly M., Kis A., Wesztergom V., Szokoli K., Novak A., 2015, Increasing the effectiveness of electrical resistivity tomography using γ 11n configurations: *Geophysical Prospecting*, 63, 508-524.

Tejero A., Chávez R.E., Urbieta J., Flores-Márquez E.L., 2002, Cavity Detection in the southwestern hilly portion of Mexico City by Resistivity imaging. *Journal of Environmental and Engineering Geophysics*, 7, 130-139.

Tejero A., Cifuentes G., Chávez R.E., López-González A., Delgado- Solórzano C., 2015, "L" and "Corner" arrays for 3D electrical resistivity tomography: An alternative for urban zones: *Near Surface Geophysics*, 13, 355- 367.

Trogu A., Ranieri G., Fischanger F., 2011, 3D electrical resistivity tomography to improve the knowledge of the subsoil below existing buildings: *Environmental Semeiotics*, 4, 63-70.